Lejla Buzaljko

Direct Lithium Extraction from Lithium-Ion Batteries of Electrical Vehicles

NTNU
Norwegian University of
Science and Technology

Lejla Buzaljko

Direct Lithium Extraction from Lithium-Ion Batteries of Electrical Vehicles

Master's thesis in Chemical Engineering
Supervisor: Sulalit Bandyopadhyay
Co-supervisor: Hammad Farooq
June 2023

Norwegian University of Science and Technology
Faculty of Natural Sciences
Department of Chemical Engineering

NTNU
Norwegian University of
Science and Technology

Abstract

Lithium-ion batteries have dominated the electric vehicle market as a result of their high energy density and good electrochemical performance. The growing demand for lithium-ion batteries is largely driven by the electrification in the transportation sector, allowing for a faster transition from fossil fuels. However, this growing global demand for electrical vehicles and lithium-ion batteries pose questions regarding their circularity, potentially resulting in a serious waste problem and loss of valuable critical raw materials if not properly treated and recycled. In this work, an attempt has been made to develop a process for the early-stage direct lithium extraction from a water leached solution of black mass, obtained from hydrometallurgical leaching. Water was employed as leaching agent in alkaline pH conditions to diminish the usage of harsh acids and to selectively dissolve lithium as the majority compound in solution. Adsorption through ion exchange was further studied as a potential direct lithium extraction technique from leachate.

The results demonstrate that the effect of temperature was negligible on the recovery of lithium during leaching, yielding the highest recovery of 17% for 25°C and low initial solid-liquid ratios of 20 g/L. Moreover, the most selective pH condition for the dissolution of lithium was found to be 10. The highest dissolution of lithium was achieved for the highest solid-liquid ratio of 150 g/L, yielding a recovery of 7.27-9.32%, confirming a reduced leaching efficiency, in contrast to the lowest solid-liquid ratio of 20 g/L, where higher leaching efficiencies were achieved (14.69-17%).

From the direct lithium extraction study it was found that Amberlite Na-form and Molecular Sieve 13X had limited performance in terms of lithium extraction, yielding 26.70% and 21.83% respectively, as a result of competing sodium ions in the leachate. The highest lithium extraction for lower initial lithium concentration was achieved for a solid-liquid ratio of 60 g/L with Amberlite H-form, yielding 93.83% extraction. Desorption with HCl demonstrated high desorption yields of 96.61%, recovering in total 88.78% lithium from the water leachate. In contrast, for higher initial concentrations of lithium, lower extraction rates were observed as a result of higher amounts of competing sodium ions in the water leachate, yielding the highest extraction of 57.92% for a solid-liquid ratio of 60 g/L. Reutilized Amberlite H-form resins showed promising results yielding >90% extraction capacity, compared to fresh Amberlite H-form resins for one additional extraction experiment for lower initial concentration of lithium. Moreover, the highest dissolution of fluoride was achieved for high solid-liquid ratios of 150 g/L and promoted in the presence of sodium ions and alkaline pH conditions.

Preface

This master thesis work was conducted at the Norwegian University of Science and Technology, Department of Chemical Engineering, Norway, on behalf of the research group in Environmental Engineering and Reactor Technology (EERT). The research work was conducted from January 2023 – June 2023.

I hereby declare that this is an independent work performed in accordance with the exam regulations of the Norwegian University of Science and Technology.

Lejla Buzaljko

Trondheim, 23.06.2023

Table of Contents

List of Figures

List of Tables

Abbreviations

CAM	Cathode active material
CRM	Critical raw material
DLE	Direct lithium extraction
EOL	End of life
EV	Electrical vehicle
GHG	Greenhouse gas
HCl	Hydrochloric acid
Li	Lithium
LIB	Lithium-ion battery
LiCl	Lithium chloride
MP-AES	Microwave Plasma Atomic Emission Spectrometer
NaOH	Sodium hydroxide
SEM	Scanning Electron Microscopy
XRD	X-ray Diffractometer

Chapter 1

Introduction

The growing demand for lithium-ion batteries (LIBs) has risen with the popularity of electrical vehicles (EVs), as a result of their high energy density, good electrochemical performance, and broad range of applications [1]. This growing demand for LIBs is a direct result of the electrification in the transportation sector, resulting in a faster and more productive transition from fossil fuels with the increased interest in energy storage systems, like wind and solar power systems [2].

LIBs are also more environmentally friendly compared to traditional batteries containing lead (Pb) and cadmium (Cd), however, with the strong increase in electrification, a stronger dependency on mining and ore processing will become a problem, both environmentally and socially. Currently, more than half of the worlds lithium (Li) production, is produced by extraction from Li-rich brines and the rest from mining hard rock ores like spodumene, petalite and lepidolite. Under current Li extraction practices, lithium chloride (LiCl) and lithium carbonate (Li_2CO_3) are produced from brines by concentration through solar evaporation until most of the liquid water is removed, followed by further refining, typically producing lithium hydroxide monohydrate ($LiOH \cdot H_2O$). This way of producing Li, evaporates on average 500.000 liters of brine per ton of Li_2CO_3. Furthermore, the hard rock extraction process is very chemical intensive, producing large volumes of waste, and is extremely slow, consequently making this technology less productive with the current surge in demand for Li and LIBs [3].

For conventional and unconventional Li resources, it is of immense interest to develop technologies and processes for the direct extraction of Li, that are more sustainable and preventative for water loss, but also more efficient compared to the current extraction methods. The optimal direct Li extraction technology is one that can specifically collect Li-ions out of complexes, while the other salts or metals remain in the solution. The current techniques and technologies applied for the direct Li extraction from brines include precipitation, sorption technologies such as ion-exchange and adsorption, as well as separation techniques using solvent extraction, specific for Li extraction and recovery [4]. Some of these techniques will be discussed in further detail in chapter 2 and 4, and play an impact on the overall scope and objective for this work.

1.1   Lithium-ion Battery Components and Cell Types

The general design of an LIB is described in Figure 1.1, illustrating that the major components of an LIB consist of the anode active material and cathode active material (CAM), where the two are often referred to as the negative and positive electrode, respectively. As can be seen from the general LIB design, the porous CAM comes in a large variety of compositions and materials, with the most common ones being NMC (Lithium Nickel Manganese Cobalt Oxide), NCA (Lithium Nickel-Cobalt-Aluminum Oxide), LCO (Lithium Cobalt Oxide), LMO (Lithium Manganese Oxide) and LFP (Lithium Iron Phosphate) [2, 5].
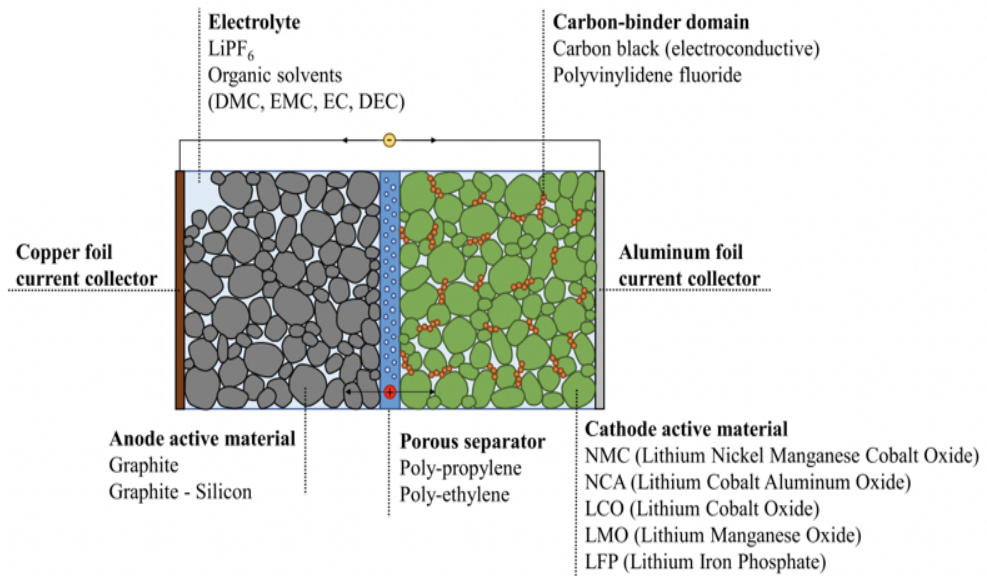
Figure 1.1: The principle of the lithium-ion battery (LIB) [5].

With the CAM, conductive carbon and a polymeric binder (e.g., polyvinylidene fluoride, PVDF), and a cathode current collector consisting of an aluminum (Al) foil are included. The porous anode is made of graphite (and optionally silicon), conductive carbon, and CMC (carboxymethyl cellulose) or SBR (styrene butadiene rubber) binder, and the anode current collector is a copper (Cu) foil [2, 5].

The porous separator is an electrically insulating membrane (eg, polypropylene or polyethylene) that prevents electrical short-circuit due to contact between the electrodes, but allows for ion-diffusion. The porous electrodes and separator are soaked in an electrolyte, typically consisting of a lithium salt (eg, $LiPF_6$ and $LiClO_4$) dissolved in an organic solvent with electrochemical stability, allowing the battery to operate at high voltage ranges [2, 5].

The cathode serves as a "source" of Li-ions (Li^+), where a power source is applied to the battery to oxidize the transition metal oxide, which causes the release of Li^+ into the electrolyte (deintercalation) and simultaneously releases electrons into the external circuit. The electrons combine with intercalated Li^+ at the graphite-based negative electrode. During discharge, the reverse reaction occurs spontaneously [2, 5].

The variation in CAM, from different battery cell manufacturers, determine the performance, stability, range and lifetime of the battery. Furthermore, LIB chemistries are evolving at a rapid pace, and new battery chemistries are being developed to produce batteries with enhanced qualities for future battery requirements [2, 6]

1.2   Todays and Future EV market

Global LIB sales has increased rapidly over the past decade, as a result of the accelerated interest in EVs and stationary storage systems. The globally increasing demand for LIBs is expected to escalate over the next decade, with the required number of GWh increasing from estimated 700 GWh in 2022 to around 4.7 TWh by 2030 [7]. LIBs for mobility applications, such as EVs, will account for the vast demand in 2030 with about 4.300 GWh, as illustrated in Figure 1.2 (Mobility). This rapid demand is largely driven by the regulatory shift towards sustainability, including net-zero targets and guidelines, greater consumer adoption rates and increased awareness for greener technologies. Furthermore, national incentives, aiming at reducing the sales of internal combustion engine vehicles in effort to reduce greenhouse gas (GHGs) emissions has also been a crucial driving force for the accelerated demand in LIBs [7, 8].
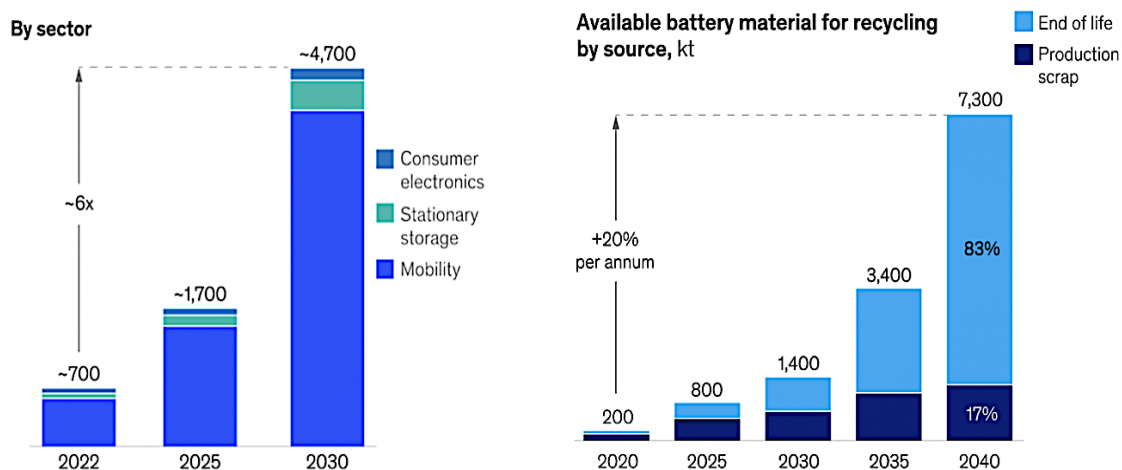
Figure 1.2: Future global LIB demand (GWh) (left) and available battery materials for recycling (Kt) (right) [7].

However, the continuous increase in LIBs placed in the global market gives rise to concerns related to their end of life (EOL) and circularity. Knowing that LIB packs are expected to serve in EVs for about 8-10 years (after 20% loss in capacity), gives rise to a discussion about how to handle EOL waste streams in the future [9]. Batteries reaching their EOL have to be removed from their original application permanently, before potentially being applied in new applications, giving them a second life, or reused in other ways before eventually being recycled.

Reuse and recycling of LIBs has been limited due to the first generation EVs still being on the road. As seen from Figure 1.2, the predicted rate of batteries reaching EOL by 2030 is expected to be low, however, the growth is projected to be more then three-fold in the following decade, with more batteries reaching EOL. Nonetheless, with the continuous technological improvements in LIBs, enhancing their cyclic stability, safety and lifetime, it can be difficult to predict the annual volume of LIBs reaching EOL for reuse and recycling, making it challenging for recyclers to obtain economies of scale [10].

1.3 Motive for Battery Recycling

As discussed in section 1.2, the growth in the EV market and LIB production imposes a demand for infrastructure and strategies to handle LIB waste and for recovering precious metals [2]. It has been estimated that 95% of the LIBs produced globally remain untreated in households or disposed in municipal landfills [2, 11]. The low recycling rates for LIBs can be attributed to several factors, including deficient legislations, absence of infrastructure for LIB collection, economic feasibility and the lack of efficient recycling technologies for the growing stream of LIB waste [11].

LIB recycling is critical for preserving valuable resources and for reducing the need for primary resources. Cobalt (Co) is considered a valuable resource, with approximately 60% of the worldwide mine production originating from the Dominican Republic of Congo, where political and social constraints contribute to raw material scarcity. Furthermore, uneven geographic distribution of Li reserves causes price spikes for Li raw materials [2]. Over the next two decades, the demands for Li will increase with 90%, following with 60-70% for nickel (Ni) and Co, stressing the demand for critical raw materials (CRMs) [12].

In addition to valuable material savings, LIB recycling has beneficial impact concerning energy consumption and environmental conservation. The production of Li, Ni, Co and Al requires excessive amounts of high energy to be extracted from virgin sources and releases significant amounts of GHGs [2]. A recycling process offers a viable solution for reintroducing LIB materials into the economic cycle, reducing

the need for primary raw materials while protecting the environment of hazardous and toxic materials from landfill disposal [2, 11].

1.4 Lithium-ion Battery Recycling and Challenges

Today, only 1% of Li is recycled, as the focus has been directed towards the more economically valuable Co and Ni metals [13]. However, with the increasing demand for Li and other CRMs, recycling of spent LIBs can provide a crucial solution to raw material scarcity and price fluctuations, as well as efficient waste management for the prevention of landfilling. By 2030, the estimated number of electric passenger vehicles on the roads will reach 215 million, and nearly 4 million electric vehicles will be phased out each year [14, 15]. The corresponding amount of batteries will be retired, even though the retired LIBs still maintain 70% to 80% of their initial capacity [9]. Consequently, 100-120 GWh EV batteries are expected to be phased out by 2030, containing significant amounts of valuable metals and toxic chemicals [14].

Collecting and recycling LIBs can be technically and economically challenging due to the complexity of the battery systems and the absence of standardized battery cell geometries and chemistries [5]. A LIB recycling process should aim at recovering critical raw battery materials with battery-grade quality to achieve a closed-loop cycle and avoid downcycling. A LIB recycling process should also aim at reducing the negative environmental impacts of landfilling and mining for virgin raw materials [5]. In the following section a general description of the current and most developed recycling routes will be discussed, after which a detail inventory of the relevant unit operations will be discussed in chapter 2.

1.4.1 Current Technologies for LIB Recycling

There are currently three main LIB recycling routes for transforming spent LIBs into recycled products, classified based on how the entrained battery elements are liberated from the electrode active materials, that being, via smelting in pyrometallurgy, through leaching in hydrometallurgy, or without any destruction of the crystalline structure of the electrode active material in direct recycling [5]. Co-precipitation can be classified as an additional recycling route being a combination of hydrometallurgy as it implements leaching while targeting to re-synthesise CAM [5]. These recycling routes consist of multiple unit operations, where each unit operation can be categorized based on its function in the process, as presented in the simplified block flow diagram in Figure 1.3.
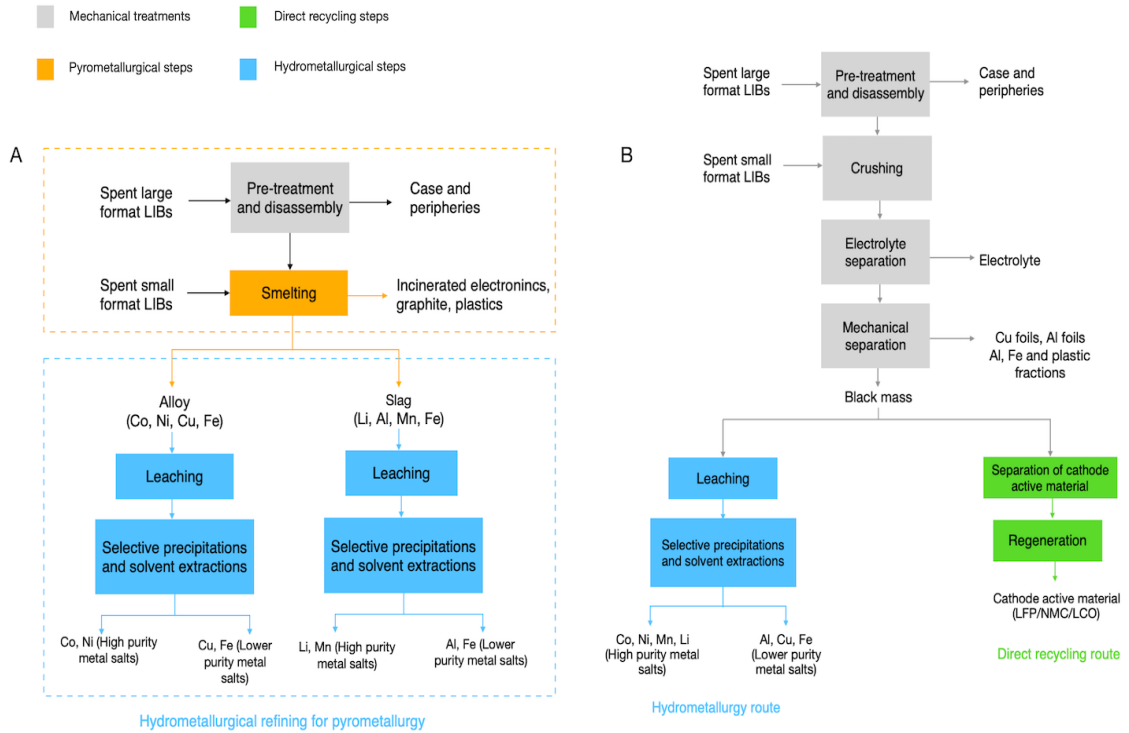
Figure 1.3: Block flow diagrams of general LIB recycling routes: (A) pyrometallurgical route, with hydrometallurgical refining of the alloy and the slag, (B) hydrometallurgical and direct recycling routes, post pre-treatment and mechanical separation [5].

A pre-treatment in the form of deactivation and mechanical separation is generally applied before smelting in the pyrometallurgical process and leaching in the hydrometalurgical process. The mechanical pre-treatment consists of the disassembly of casings, electronics and cables from the large battery systems. The disassembly is often followed by a deactivation step to prevent electrical and flammable risks [5]. The pre-treatment processes is illustrated in light grey colour in A and B in Figure 1.3, where additional steps are represented in B, illustrating the additional separation of electrolyte and removal of current collector foil scrap and plastic fragments prior to obtaining the crushed and shredded battery cells, also know as black mass.

After pre-treatment has been employed, the central parts of the recycling is initiated. As presented in Figure 1.3A, pyrometallurgy is initiated by smelting the whole battery in a high temperature (ca. 1000°C) furnace to reduce the component metal oxides to an alloy of Co, Cu, and Ni, which can be further refined via hydrometallurgy to obtain high-purity metal salts [5, 16]. The electrolyte is evaporated in a lower temperature zone of the furnace and directed to energy recovery while plastics and graphite are burnt in the higher temperature zone of the furnace. Li, Al, Mn and some Fe is retained as part of the slag fraction which can be further refined via hydrometallurgical operations [5].

Leaching is the most significant unit operation in hydrometallurgy, where various types of acids (inorganic and organic) are employed to dissolve CAM from black mass into solution. The CAM can further be recovered as single-phase metal salts through crystallization, selective precipitation, solvent extraction and electrochemical methods [5]. The hydrometallurgical route is presented in light blue colour in Figure 1.3A and 1.3B, aiming at recovering battery grade salts that can be reused in battery production, closing the loop for critical battery materials.

Differently from the pyrometallurgical route, hydrometallurgy requires pre-treatments in the form of dismantling, crushing, electrolyte separation followed by a mechanical separation (in light grey in 1.3B), allowing for the recovery of Al, Fe and Cu scrap, prior to black mass being subjected to hydrometallurgy [5].

Similarly to hydrometallurgy, black mass is also the starting point of the direct recycling route, described in bright green colour in Figure 1.3B. Direct recycling involves separation and regeneration of CAM (and anode material) without destructing the crystalline cathode morphology through leaching and high temperature treatments. The recycled products from direct recycling are intended for the direct reuse for manufacturing new LIBs [5, 17]. However, this recycling process will incur large scale difficulties with the varying battery chemistires and designs, making the necessary disassembly and separation of components much more challenging [18].

1.4.2   Comparison for Pyrometallurgy and Hydrometallurgy

As a general comparison between the discussed recycling routes, pyrometallurgy has the opportunity to recycle a variety of LIBs with different geometries and chemistries. In addition, pyrometallurgy is the most technologically developed technology for recycling LIB at an industrial scale, making it capable of processing large amounts of volume. The crucial drawback with the pyrometallurgical route is the high energy consumption in the smelters, resulting in a net increase in GHGs, as well as low purity in the recycled products leading to downcycling of CRMs [5].

In contrast, hydrometallurgy allows for high purity and selectivity of the recovered metals, with lower energy consumption and toxic gas emissions, compared to pyrometallurgy [5]. However, the aim to specifically recover metals from black mass can reduce the application of hydrometallurgy on an industrial scale, potentially resulting in lower productivity for smaller volumes [5]. Hydrometallurgy will nonetheless still be one of the main drivers for future LIB recycling technologies, as it today is the only process that has potential to recover all CRMs from spent LIBs. With this, hydrometallurgy will be the main recycling technology studied throughout this work.

Thesis Outline

Chapter 1 provides an insight into the state-of-the-art lithium-ion batteries, the future market predictions of lithium-ion batteries, the motivation for recycling, as well as the current recycling technologies with their associated advantages and challenges.

Chapter 2 explains the fundamental theory behind relevant unit operations in the hydrometallurgical process. The chapter is divided into two parts, metal dissolution and metal extraction, where leaching, adsorption and ion exchange will be discussed in detail.

Chapter 3 gives a brief overview of the relevant characterization techniques used in this work, mainly being x-ray diffraction, scanning electron microscopy, microwave plasma atomic emission spectrometer and fourier-transform infrared spectroscopy.

Chapter 4 includes a literature review with a greater focus on leaching, both acidic and water leaching, as well as adsorption through ion exchange. A discussion regarding the approaches employed in literature will also be included.

Chapter 5 lays the groundwork for the experimental pathway for the direct lithium extraction from a water leached solution of black mass. Chemical reagents, experimental procedures and analytical instrumentation utilized for qualitative and quantitative analysis will be listed.

Chapter 6 presents the analysis of the earlier chapter including an associated discussion related to literature findings and new propositions.

Chapter 7 provides a conclusion for the main discoveries of the study and suggestions for future work.

Chapter 2

Theoretical Background

This chapter serves as a background for selected unit operations in the hydrometallurgical recycling process. First, the leaching unit operation for metal dissolution from solids will be described, next an overview of relevant mechanisms for adsorption and ion exchange, for metal extraction from liquids, will be defined.

2.1   Metal Extraction from Solids

2.1.1   Leaching

As previously introduced, leaching is the most significant unit operation in the hydrometallurgical process. Leaching, often referred to as solid-liquid extraction, is a mass-transfer driven operation involving the liberation of metals into solution by chemical dissolution, forming the basis of the hydrometallurgical extraction process [19]. The main objective of leaching, is to convert valuable insoluble metals into soluble salts, that can be further recovered through operations like solvent extraction, adsorption and precipitation, to name a few examples.

Leaching is widely used in the metallurgical industry for extracting metals like gold (Au) and Al from ores. However, leaching can also be applied for extracting valuable metals from sources like spent LIBs, as previously discussed (section 1.4.1). The main motive for leaching spent LIBs, is to convert the metals present in the black mass, procured in the pre-treatment step, into ionic solutions [20].

The leaching media most widely employed for dissolving valuable metals from black mass into solution are organic and inorganic acids, with the most common inorganic acids being sulfuric acid (H_2SO_4), nitric acid (HNO_3) and hydrochloric acid (HCl). Acidic leaching is often performed in combination with hydrogen peroxide (H_2O_2), which acts as an external reducing agent to increase the leaching efficiency by converting insoluble metals like Co^{3+}, into the soluble divalent Co^{2+} metals. However, these inorganic acids adverse environmental impact due to emissions of pollutants like SO_X, Cl_2 and NO_X [21, 22].

For these reason, substitution of inorganic acids with more environmentally friendly organic acids, like oxalic acid ($H_2C_2O_4$) or even water as a leaching agent, can reduce the environmental impact of the recycling process and make it more sustainable [21, 23]. Furthermore, there are several factors that can impact the efficiency of a leaching process, such as concentration, pH, time, temperature, solid-liquid ratio and particle size [20]. These factors will be discussed in further detail in chapter 4, where previous work and research from literature will be reviewed.

2.2 Metal Extraction from Solution

After metal extraction has been performed, yielding a leached solution (leachate) containing metals and impurities, follows a separation and purification step for the recovery of the desired metals. Solvent extraction, adsorption through ion exchange, crystallization and precipitation are established techniques often employed for this purpose. As this specific work will cover the applicability of adsorption through ion exchange, a greater focus will be directed towards the discussion of this underlined technique.

2.2.1 Adsorption and Ion Exchange

The adsorption separation/extraction technique involves the partitioning of a gaseous or liquid component, by the contact of an external and/or internal solid surface. The solid material is characterized by it surface area and the forces of attraction, namely physical mass transfer (physisorption), mass transfer with chemical reactions (chemisorption) and by the exchange of ions from a mixture to a solid surface (ion exchange) [24]. Figure 2.1 illustrates the general adsorption process, showing the adhesion of molecules (blue) onto the solid surface of the adsorbent (grey).
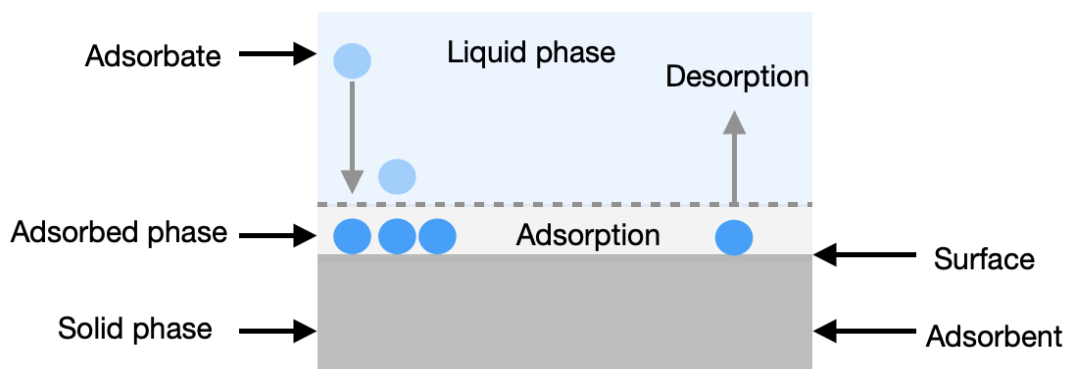
Figure 2.1: Schematic illustration over the general adsorption process.

From the figure above one can see that the adsorbing phase is often referred to as the adsorbent, and the material concentrated/adsorbed at the surface of that phase is the adsorbate. The amount of adsorption will be affected by the available surface and pore volume of the adsorbent, and depends also on the chemical properties of the fluid and the solid. Furthermore, the rate of adsorption also depends on the rate of diffusion to the adsorbent, which also depends on temperature, concentration and pressure [25].

Ion exchange is often discussed interchangeably with adsorption, as the two processes share many of the common features. Ion exchange is also a mass transfer driven process, where ions are the sorbed species in contrast to adsorption, where electrically neutral species are sorbed [24]. Ion exchange is employed to remove soluble ions or charged molecules (cations and anions) from a solution, either through cation exhcange or anion exchange. The ions in solution are transferred to a solid matrix due to different charges and involve the exchange of ions with the same polarity. Typical ion exchangers are ion-exchange resins (porous resin beads), zeolites (porous silicate minerals) and specific clays (layered silicate minerals) to name a few examples [19].

For an ion exchange resin, in the ionic form A, that is in contact with a solution containing ions B, an equilibrium reaction will be formed, described from equation 1 [26]. In the process described from equation 1, ions A will migrate into the solution and be replaced by ions B from the solution until equilibrium is reached [26]. From the equilibrium state, selectivity coefficients can be defined based on the ratios of ions in solution against the ions on the resin, described from equation 2, if the activity coefficients (γ) are defined to be constant [26]. From equation 2, K is the selectivity coefficient of B^+ over A^+, and the bar (-) indicates the resin phase. Effectively, the selectivity coefficient for an ion is a measurement of a resins preference for that specific ion, meaning, that for higher selectivity coefficients, a greater preference for the underlined ion [26, 27].

$$R - A^+ + B^+ \longleftrightarrow R - B^+ + A^+ \tag{1}$$
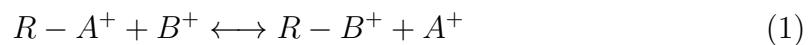
$$K_A^B = \frac{[A]}{[B]} \cdot \frac{[\bar{B}]}{[\bar{A}]} \tag{2}$$

In Figure 2.2, a schematic illustration over the ion exchange process, utilizing a immobile cation surface to selectively separate positive molecules from the negative ones, is presented. The figure also shows the process of elution, where the positively charged molecules are being separated, prior to the negatively charged molecules are being eluated and stripped from the cation surface [19, 28]. Figure 2.2 is presented to give a better understanding over the principle differences between ion exchange and adsorption, which was presented in figure 2.1.
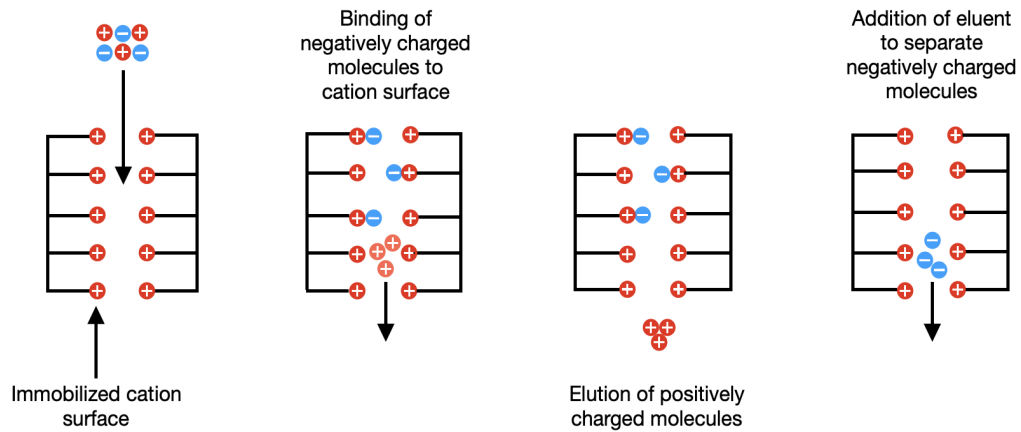
Figure 2.2: Ion exchange process utilizing a immobile cation surface to eluate positively charged molecules prior to the negatively charged molecules [28].

In chapter 4, studies from literature regarding adsorption and ion exchange as a separation and extraction technology will be discussed in greater detail. A greater focus will be directed towards the applicability of ion exchange as a potential method for the direct extraction of Li from hydrometallurgical leaching, will be discussed, as this will be one of the main fields studied throughout this work.

Chapter 3

Characterization Techniques

In this chapter, a brief overview of the relevant characterization techniques used throughout this work, will be presented. Quantitative and qualitative analysis are important for the investigation of dissolved metals in solution and solid composition analysis. The following chapter will present the theory behind x-ray diffraction, scanning electron microscopy, microwave plasma atomic emission spectroscopy and Fourier-transform infrared spectroscopy.

3.1   Powder X-ray diffraction (XRD)

Powder X-ray diffraction (XRD) is a non-destructive characterization method frequently used for the identification of different crystallographic structures in powder material and atomic spacing. XRD is based on constructive interference of monochromatic X-rays, being generated by a cathode ray tube directed towards the powder sample [29]. The exchange of produced incident rays with the powder material produces constructive interference and a diffraction ray when conditions are satisfied by Bragg's law, described in Figure 3.1.
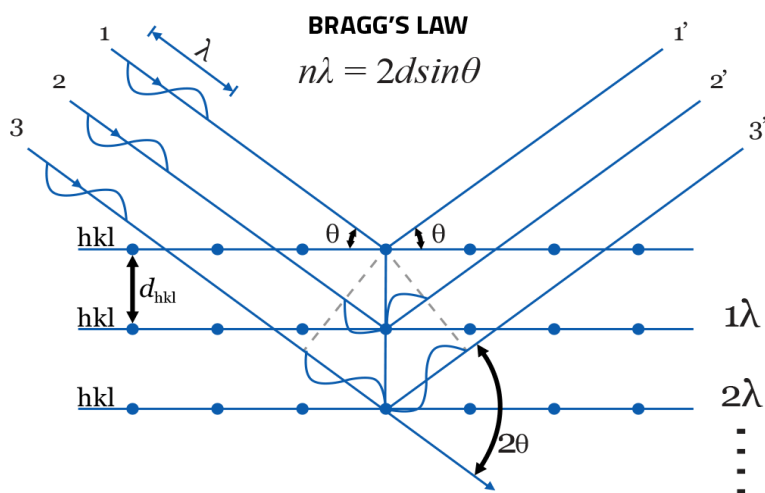
Figure 3.1: Diffraction of X-rays governed by Bragg's law [30].

From Bragg's law, n is an integer, λ is the wavelength of the X-rays, d is the interplanar spacing generating the diffraction, and θ is the diffraction angle. Braggs's law associates wavelengths from electromagnetic radiation to a diffraction angle and the lattice spacing in the crystalline sample. As previously stated, X-rays are produced in a cathode ray tube, where electrons are accelerated towards the target material. Copper is most frequently used target material, with CuK_α radiation = 1.54 Å. The produced X-rays are collimated and directed towards the powder sample material. When the geometry of the X-rays, that are influencing the powder sample, satisfy Bragg's law, constructive interference happen and peak intensity appears [29].

3.2 Scanning Electron Microscopy (SEM)

Scanning electron microscopy (SEM) is an important microscopy technique, capable of achieving detailed visual imaging of particles at high resolutions. SEM is a state-of-the-art instrument commonly employed for studying surface phenomena of materials, giving information about topography and morphology. The fundamental principle governing the microscopy technique, is the release of primary electrons from the electron gun, providing energy to the atomic electrons of the measured sample. The secondary atomic electrons form an image, gathered by electron collectors (detectors) from each point of the measured sample [31].
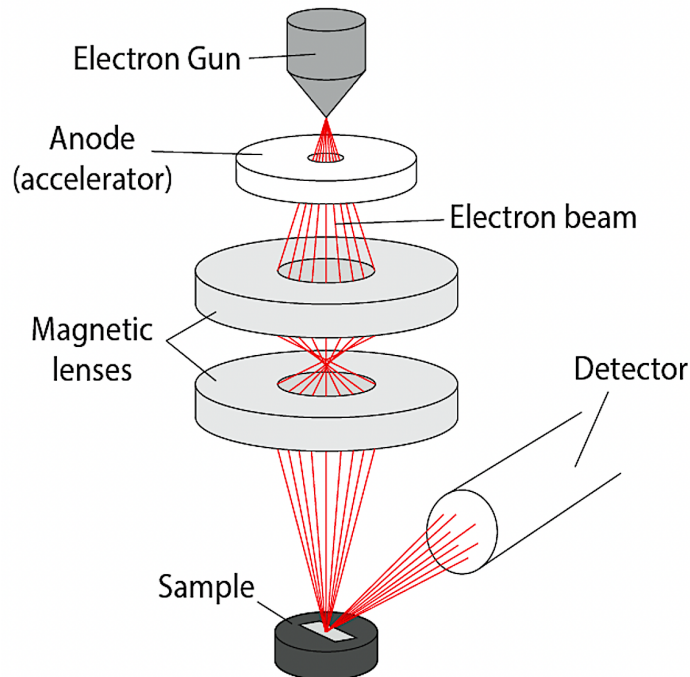
Figure 3.2: Schematic diagram of the core components of SEM [32].

The schematic diagram governing the principles of SEM is presented in Figure 3.2, where the incidence of electrons are being accelerated down the column of the microscope by the negatively charged anode, repelling the electrons. The electrons are further focused onto the sample by magnetic lenses, to ensure a narrow beam of electrons onto the sample, followed by scanning of the sample surface and signals detection from the secondary electrons to generate the final image [31, 32].

3.3   Microwave Plasma Atomic Emission Spectroscopy (MP-AES)

Microwave plasma atomic emission spectroscopy (MP-AES) is an analytical technique employed for determining the elemental composition of a sample by examining its electromagnetic spectrum. MP-AES is based on specific element excitation, where an atom emits light in a characteristic pattern of wavelengths, an emission spectrum, as it returns to its ground state. Sources for atomic emission include microwave plasma (MP) and the inductively coupled argon plasma (ICP) with both being high temperature sources for excellent excitation for atomic emission spectroscopy [33].

The microwave plasma is formed from nitrogen and can reach temperatures near 5000 K. At these temperatures the atomic emission is strong, producing wide detection limits and linear dynamic range for most elements. Effectively, the MP-AES runs on air, and the nitrogen is extracted from compressed air from a generator to fuel the plasma [33].
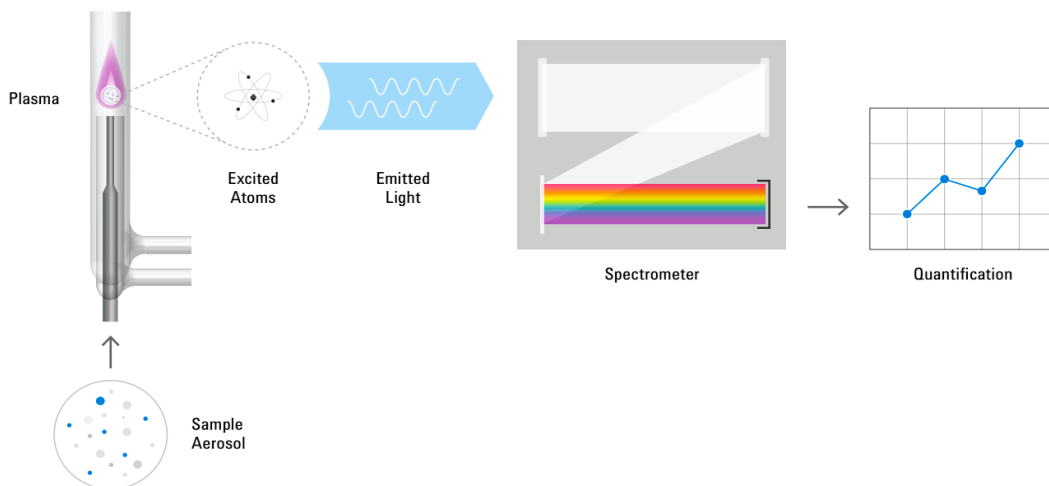
Figure 3.3: Working principle of MP-AES [33].

As illustrated in Figure 3.3, an aerosol is formed from a nebulized liquid sample in a spray chamber. The aerosol is further introduced into the centre of the hot plasma. The aerosol dries, decomposes and is atomized. The atoms continue to be excited

and emit light at their characteristic wavelengths before returning to their lower energy states. MP-AES quantifies the concentration of an element in a sample by comparing its emission to a known concentrations of the element, using a calibration curve [33].

3.4 Fourier Transform Infrared Spectroscopy (FTIR)

Fourier transform infrared spectroscopy (FTIR) is another non-destructive analytical technique used to identify organic materials, and in some cases inorganic materials. The FTIR technique measures the absorption of infrared radiation by the sample material against the wavelength, where the infrared absorption bands identifies molecular components and structures. When a material, solid or liquid, is irradiated with infrared radiation, the absorbed infrared radiation excites molecules into a higher vibrational state. The wavelengths that are absorbed by the analyzed sample are of its characteristic molecular structure [34].

Figure 3.4 presents the schematic working principle of FTIR, where a beam of light, containing various frequencies, reflects on a sample and measures the amount of beam absorbed by the material, producing data points. These data points are then analyzed from a computer in a backward direction, to measure the absorption at each wavelength [34, 35].
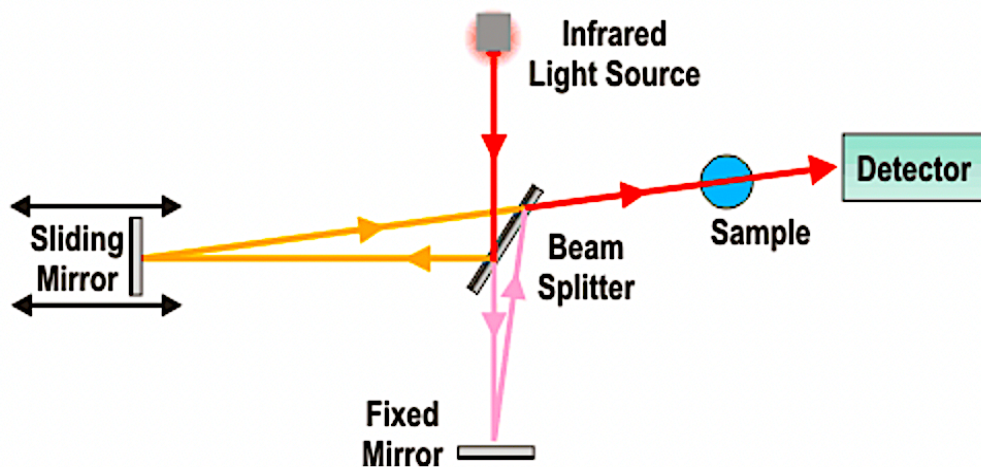
Figure 3.4: Schematic representation of FTIR [34].

The FTIR uses an interferometer to regulate the wavelength through a broadband infrared source. A detector, illustrated in Figure 3.4, measures the intensity of transmitting light as a function of its wavelength. The signal from the detector is an interferogram which is then further measured from a computer, using Fourier transformation to obtain a single-beam infrared spectrum, hence the name [34, 35].

Chapter 4

Literature Review

In chapter 2, the theory behind relevant unit operations employed in hydrometallurgical recycling were described, with a grater focus on leaching for metal dissolution, and adsorption though ion exchange for metal extraction from liquids. In this chapter, the foremost applications, as described in literature, will be presented with more detailed descriptions of the previously discussed unit operations in hydrometallurgy, as well as techniques for the direct lithium extraction from solutions, as this will be further studied throughout this work. The general hydrometallurgical route for recovering metals from spent LIBs was described in chapter 1, in section 1.4.1.

4.1 Leaching

The majority of studies, presented in literature, have investigated leaching of mixed cathode material with acidic leaching agents. Inorganic acids, like sulfuric acid (H_2SO_4), hydrochloric acid (HCl) and nitric acid (HNO_3) are commonly used as leaching agents due to their effectiveness and low reagent cost. Compared to H_2SO_4 and HNO_3, HCl requires a lower concentration threshold to achieve high leaching rates and efficiency, eliminating the need for a reducing agent [2]. A crucial disadvantage by utilizing HCl as a leaching agent is the evolution of toxic Cl_2 vapour from the oxidation of Cl^-, as shown from reaction equation 3 [2].

$$6LiNi_{1/3}Mn_{1/3}Co_{1/3}O_2\ (s) + 24HCl\ (aq) \longrightarrow 2NiCl_2\ (aq)$$
$$+MnCl_2\ (aq) + 2CoCl_2\ (aq) + 6LiCl\ (aq) + 3Cl_2\ (g) + 12H_2O\ (l) \tag{3}$$
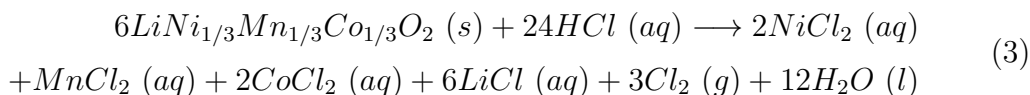
On the other hand, the leached products of H_2SO_4 are more kind as shown from reaction equation 4. Previous research, has demonstrated that when using H_2SO_4 without a reducing agent, the maximum leaching efficiency of 50.2% and 66.2% were obtained for Mn and Co respectively, due to the presence of lowly soluble Co^{3+} and Mn^{4+} in the spent batteries. However, when coupled with a reducing agent, e.g. H_2O_2, the leaching efficiency increases significantly achieving more than 95% in leaching efficiency for all metals entrained in the cathode material [2].

$$6LiNi_{1/3}Mn_{1/3}Co_{1/3}O_2\ (s) + 9H_2SO_4\ (aq) + H_2O_2\ (l) \longrightarrow 2NiSO_4\ (aq)$$
$$+2MnSO_4\ (aq) + 2CoSO_4\ (aq) + 6Li_2SO_4\ (aq) + 2O_2\ (g) + 10H_2O\ (l) \tag{4}$$
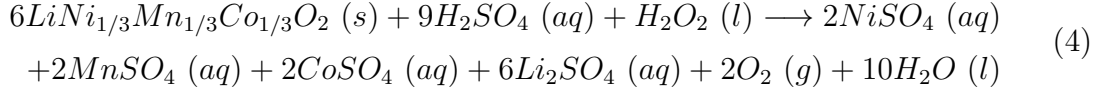
From literature, an increasing interest in organic acids as leaching agents have been reported, as a result of their biodegradability, lower acidity and release of toxic/harmful gases (eg, Cl_2, NOx, SO_x). Although the acidity of organic acids is considerably lower than for inorganic acids, organic acids have great leaching abilities, as they form chelation complexes and stabilize the dissolution of metals [2]. Among the organic acids, citric acid, acetic acid and oxalic acids are widely used. In equation 5, the leaching of NMC111 black mass using a generic monoprotic organic aced (HOA) is depicted [2].

$$6LiNi_{1/3}Mn_{1/3}Co_{1/3}O_2\ (s) + 18HOA\ (aq) + 3H_2O_2\ (l) \longrightarrow 2Ni(OA)_2\ (aq)$$
$$+2Mn(OA)_2\ (aq) + 2Co(OA)_2\ (aq) + 6LiOA\ (aq) + 3O_2\ (g) + 10H_2O\ (l) \tag{5}$$
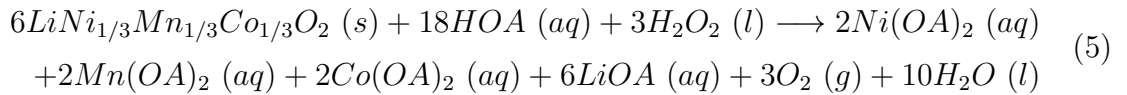
Nonetheless, with the growing demands for Li, research has been driven towards making processes that can more selectively recover Li as a main priority. In the current hydrometallurgical processing route, Li is recovered as one of the final products (Figure 1.3), often being contaminated with impurities as other metals are recovered in advance, often through chemical precipitation or solvent extraction. Water leaching, post pre-treatment of spent LIBs, has emerged as a potential solution for the early-stage Li recovery from black mass in the hydrometallurgical process. Utilizing water as a leaching agent has demonstrated selective dissolution of Li in solution as a majority compound, leaving the other metals entrained in the black mass in the raffinate. Léa et.al investigated the early-stage Li recovery from spent LIBs using a thermal pre-treatment followed by water leaching [23]. From the study a maximum Li recovery of 62% was obtained after pyrolysis at 700 °C, for a solid-liquid ratio of 20 (g/L). In the study it was argued that the thermal pre-treatment had a positive effect on the recovery of Li, since the CAM decomposes and the contact surface between the CAM and leaching agent increases [23].

Furthermore, from previous studies, investigating the selective recovery of Li, by the employment of water as a leaching agent, it was found that alkaline pH conditions of 10 were favourable for the selective dissolution of Li in solution [36]. Moreover, it was also recognised that for a lower solid-liquid ratio, the leaching efficiency was high, but the concentration of Li in solution was low. However, when the solid-liquid ratio was increased, the leaching efficiency decreased and the concentration of Li in solution increased [36]. In chapters 5 and 6, water leaching will be investigated further with the aim to selectively dissolve Li as a majority metal in solution.

4.2   Direct Lithium Extraction from Solution

The fundamental principles governing ionic separation and extraction from solution was depict in chapter 2, where adsorption through ion exchange was introduced. The predominant factors that influence selecting a method for the recovery of Li are the practical applicability of the method, the co-existing contaminant ions, and the effect of other competing ions.

For the selective extraction of Li, adsorption technologies through ion exchange, have shown superior selectivity towards Li, as well as simple and efficient applicability and less environmental impact compared to solvent extraction, which suffers from pollution and excess use of harsh chemicals [37, 38]. The main studied processes for the selective extraction of Li have been designed for the application on natural Li bearing brines, often referred to as direct lithium extraction (DLE) from brines, and not on industrial effluents, like for example on black mass from spent LIBs. DLE technologies aim to tackle both the environmental and techno-economic shortcomings of the solar evaporation technology, previously discussed in the introduction of this work (section 1), aiming for the avoidance of open air evaporation ponds as well as be more responsive to the future Li demands [39].

The adsorbents designed for DLE require manufacturing of a solid material morphologically modified with active sites for optimal Li selectivity. The most common adsorbents for the recovery of Li through ion exchange, as presented in the literature, are listed in Table 1. From the table, the adsorbents comprise of inorganic metal-based aluminum (Al), manganese (Mn), and titanium (Ti) adsorbents. The principle governing Li sorption by metal adsorbents is based on the structural memory effect as a result of Li^+ tendency to occupy the vacancies by removing the original Li^+ from the pristine structure [38]. The mechanism of the structural memory effect for Li adsorption-desorption can be described from equation 6, utilizing a Li-Al layered double hydroxide (Li/Al-LDHs) adsorbent [38, 40].

$$xLiCl + [Li_{(m-x)}Al_2(OH)_6]Cl_{(m-x)} + (n+1)H_2O \leftrightarrows \\ [Li_mAl_2(OH)_6]Cl_m \cdot nH_2O + H_2O \tag{6}$$
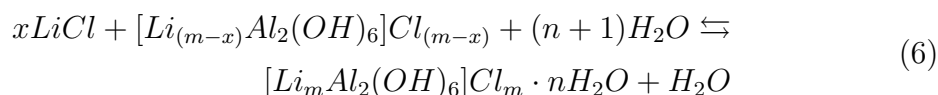
Jing et.al investigated the Li adsorption capacities of Li/Al-LDHs on low grade brines, where Li/Al-LDHs was synthesized using a coprecipitation method utilizing $AlCl_3$, LiCl and NaOH. The study of Jing et.al demonstrated that Li/Al-LDHs had superior adsorption selectivity towards Li with ion selectivity sequence of $Li^+>$ $Na^+>$ $K^+>$ $Ca^{2+} \gg Mg^{2+}$ with a reported uptake capacity of 7.27 mg/g [40].

Table 1: Technologies for DLE through morphologically altered materials.

Adsorbent	Prepration	Li$^+$ adsorption performance	Reference
Li/Al-LDHs	Coprecipitation	Li capacity of 7.27 mg/g in Qarhan old brine	[40]
Li$_4$Mn$_5$O$_{12}$	EDTA-citrate complexing	43.1 mg/g in 0.5 g/L LiCl solution	[41]
Li$_2$TiO$_3$	Hydrothermal method	76.7 mg/g in LiOH solution (2 g/L of Li) at 30 °C for 24 h	[42]
Li$_4$Ti$_5$O$_{12}$	Hydrothermal method	160.6 mg/g in LiCl solution with 2000 mg/L of Li	[43]
Li$_{1.6}$Mn$_{1.6}$O$_4$	Hydrothermal method	40 mg/g in seawater	[44]

However, as previously stated, adsorbents require manufacturing of a solid material that can create active sites with strong selectivity towards Li$^+$. As a result of this, great interest in commercially available ion exchange resins, with high affinity for Li$^+$ has emerges as a potential technology for DLE [39]. Julien et.al studied the adsorption/desorption process for the selective recovery of Li$^+$ from a LiCl solution, utilizing commercially available Amberlite IR 120 exchange resin (H-form and Na-form) and molecular sieve 13X [45]. The study was performed with the motive to device a process for the selective recovery of Li$^+$ from streams such as leachate of spent LIBs, obtained from hydrometallurgical leaching. Both Amberlite IR 120 and the molecular sieve 13X showed good Li$^+$ uptake through ion exchange ranging between 12.9 and 14.2 mg/g with fast reaction kinetics at ambient temperature [45].

Amberlite IR 120 (H-form and Na-form) are Gaussian gel type strongly acidic cation exchange resins of the sulfonated polystyrene type (R-SO$_3$H and R-SO$_3$Na) with 8% crosslinks, whereas molecular sieve 13X are synthetically produced zeolites with three-dimensional structures based on silicon oxide (SiO$_4$) and aluminum oxide (AlO$_4$) polyhedra [45–47]. The polyhedra are linked by their corners to produce an open structure with internal cavities in which ions can be retained. By the substitution of Si^{4+} by Al^{3+}, a negatively charged surface develops, which enables cation exchange [47]. Both Amberlite IR 120 (H-form and Na-form) and molecular sieve 13X are nontoxic, cheap and available in different grain size. Furthermore, the adsorbents have showed promising reuse over several adsorption–desorption cycles that renders them environmentally friendly [47]. The employment of DLE, through ion exchange, can contribute to improved and simpler operations, compared to the current Li extraction methods, as well as contribute to great Li raw material demand and circularity. In the upcoming page, the thesis aim and scope will be presented.

Aim and Scope of work

Li is a fundamental raw material for the renewable energy transition owing to its widespread use in EVs. With the increasing demand for LIBs, as a result of the electrification in the transportation sector, a focus has to be directed towards the optimization of Li recovery from secondary sources, like spent LIBs from EVs, to prevent emissions of harmful materials and to provide a solution to Li raw material scarcity in the future. At present, only 1% of Li is recycled, despite the critical raw material scarcity. This underlines the crucial necessity for a recycling process that is specifically designed to recover Li in a sustainable and efficient operation.

Today, the conventional methods for the direct extraction of Li, have been studied for the employment on primary Li sources, like Li-bearing brines. For these reasons, this work will investigate the DLE from mixed-metal (NMC) LIB electrodes, with the overall goal of resource savings and meeting the future resource demands for the increasing EV market.

The work will cover the DLE from a water leached solution of black mass, through ion exchange. The ion exchange technique will be investigated as a potential extraction method from a conventional hydrometallurgical process utilizing water as a leaching agent. Incentives for utilizing water as the leaching agent is the ascribed lower environmental footprint and a more favorable recovery directed towards Li. Quantification of fluoride in the electrode material will also be investigated throughout this work, to establish the amount of fluoride dissolved in solution during the leaching operation and to study the effect of parameters on the dissolution. A simplified flow chart representing the experimental path for the DLE from a water leached solution of black mass through ion exchange is represented in Figure 4.1, where the experimental path will follow the flow chart chronologically.
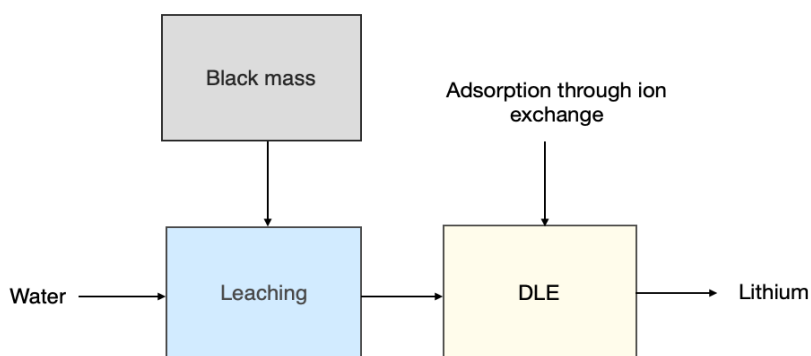
Figure 4.1: Experimental path for DLE from black mass.

Chapter 5

Materials and Experimental Setup

In this chapter, the chemical reagents used in the experimental procedure will be described, as well as the experimental setup. The experimental procedure can be represented by the block flow diagram in Figure 4.1, which shows the route for the dissolution of Li through water leaching. The path is followed by adsorption through ion exchange for the direct extraction of Li from the leachate.

5.1   Materials used in experimental work

LIBs of the prismatic cell type were supplied by Norsk Hydro ASA (Hydrovolt). Pre-treatments performed by Hydrovolt include drying at $\sim$ 200°C to remove the electrolyte, and magnetic separation to remove iron. This black mass was further treated at NTNU, where milling and sieving was performed as to obtain a black mass size < 53 µm. For black mass metal digestion, a mixture (3:1) of hydrochloric acid (HCl, 37.0%) and nitric acid (HNO_3, 65.0%) was used to make aqua regia solution. For fluoride digestion from black mass, nitric acid (HNO_3, 2.0%) and sodium sulfite (Na_2SO_3, $\geq$98.0%) was used. Sodium chloride (NaCl, $\geq$99.0%), acetic acid (CH_3CO_2H, $\geq$99.0%) and CDTA (trans-1,2-Diaminocyclohexane-N,N,N',N'-tetracetic acid monohydrate, $\geq$99.0%) was used to make total ionic strength adjustment buffer (TISAB II). Distilled water (DI) was utilized as leaching agent for the water leaching experiments of black mass. Sodium Hydroxide (NaOH, >99%) was utilized to make a 5M solution for pH adjustments for the water leaching experiments.

For the adsorption experiments, three selected ion exchange resins where used, namely Amberlite® IRC120 H, hydrogen form, Amberlite® IR120 Na, sodium from and Molecular Sieve 13X. ICP Multi-element standard solution IV (1000 mg/L Ag, Al, B, Ba, Bi, Ca, Cd, Co, Cr, Cu, Fe, Ga, In, K, Li, Mg, Mn, Na, Pb, Sr, TI, Zn) from Certipur® was used for calibration standards preparation prior to MP-AES analysis. Fluoride standard solution (1000 mg/L F) from Certipur® was used for constructing calibration curves for the Fluoride Selective Electrode. All chemicals were obtained from Sigma Aldrich and used without further purification. Solutions were prepared using MQ water.

5.2 Metal quantification and Characterization

The metal composition, as well as the phases of the utilized solid black mass and obtained filter residues, where characterized using X-ray Diffractometer (XRD, Bruker D8 A25 DaVinci). The characterization for crystalline samples was performed in the range of 20-80° with a step size of 0.013° for a total step time of 126.72 seconds, resulting in 1 hour total for all crystalline samples. Additionally, the particle morphology of the utilized black mass and filter residues were examined using Scanning Electron Microscopy (SEM, FEI Apreo) at an accelerating voltage of 30 kV and a beam current of 0.10 nA, without tiltage.

The metal ions in solution were quantified using Microwave Plasma Atomic Emission Spectrometer (MP-AES). Calibration curves were fabricated by the MP-AES associated software from calibration standards in the rage of 1-25 mg/L, prepared from a multi-metal 1000 mg/L stock solution. Prior to the MP-AES analysis, the solid samples were digested with the Speedwave® Microwave Digestion System (Berghof SpeedWave XPERT). Furthermore, Fourier-Transform Infrared Spectroscopy (FTIR, Bruker Vertex 80v) was used to investigate the infrared spectrum of black mass for fluoride detection and a Fluoride Selective Electrode (FSE, Metrohm) was used to quantify the fluoride in the solid black mass and obtained liquid samples.

5.3 Metal Digestion

To quantify the metals in the solid black mass, solvent digestion was performed followed by analysis with MP-AES. Black mass consists of an inhomogeneous mixture of different solid components, making it challenging to quantify due to variations in each solid sample. Knowing this, it was decided to perform two independent digestion methods, namely microwave assisted digestion and manual digestion, to compare the results obtained from both methods.

5.3.1 Microwave Assisted Digestion

Digestion of solid samples was performed to quantify the mass of metals in the solid black mass, prior to analysis with MP-AES. Approximately 0.5 g of the black mass was weighed and placed in a PTFE vessel. Aqua regia solution, consisting of a 10 mL solution HCl and HNO_3 (volumetric ratio of 3:1, respectively) was further added into the vessel. The mixture was allowed to de fume for 10 minutes before sealed and placed in the Berghof Speedwave Xpert for microwave digestion. A manual program from Agilent was used to digest the solid samples, described in Table 2. Following the digestion, the samples were filtered using a syringe to remove graphite.

Table 2: Microwave assisted digestion program utilized for black mass digestion.

Step	T (°C)	p (bar)	Ramp	Hold	Power (%)
1	150	40	10	15	50
2	180	40	10	25	40
3	50	0	0	0	0

5.3.2 Manual Digestion

Manual digestion was performed similarly to microwave assisted digestion, starting with weighing approximately 0.5 g of the solid black mass sample in a beaker. 8 mL of aqua regia solution, consisting of HCl and HNO_3 (volumetric ratio of 3:1) was added and left to react for 24 hours in room temperature. The suspension was filtered using a syringe and collected for further MP-AES analysis. The manual digestion, with the main process steps is illustrated in Figure 5.1.
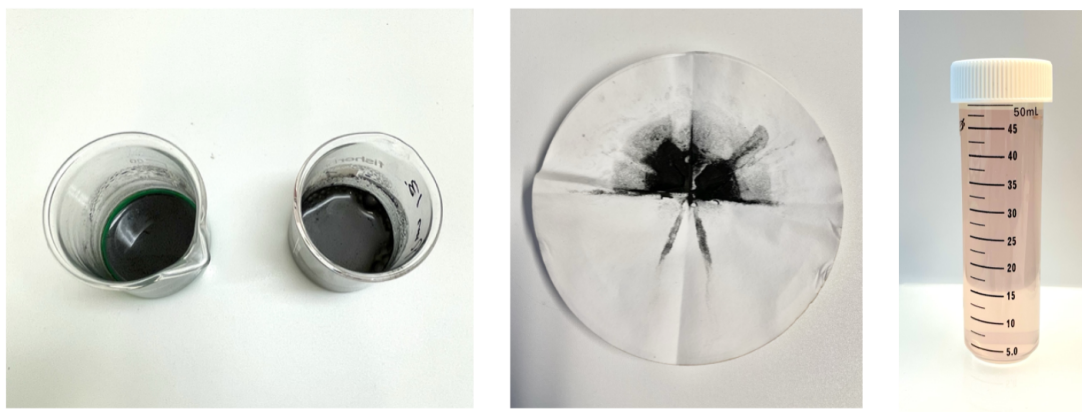
Figure 5.1: 1) Manual digestion of black mass with aqua regia. 2) Graphite filtrate post reaction. 3) Filtered solution post graphite removal.

5.3.3 Fluoride Digestion

Fluoride digestion from the black mass powder was initiated by weighing approximately 1 g of the solid powder prior to leaching with 2% HNO_3. The leaching time was set to 30 minutes at 70°C over a water bath. After the given reaction time, the suspension was set for cooling to room temperature before further addition of Na_2SO_3 (approximately 1/64 tbs). A second leaching was done following the addition of Na_2SO_3 for 15 minutes at 70°C over the same water bath. Following, the solution was filtered and diluted to 250 mL prior to measurements with FSE.

5.4   Water Leaching Experimental Procedure

Water leaching experiments were performed with the motive to selectively dissolve Li in solution, to later be used in the DLE experiments and for analysing with FSE. Furthermore, the study was performed with the motive to verify previous studies [36]. The software JMP was used to create a design of experiment (DOE) for the leaching experiments, applying the "Custom Design" feature. The continuous factors comprising of temperature, pH and solid-liquid ratio as a design option, created a randomized list of 20 experiments, described in Table 3, predicting the desired response of Li concentration in solution. The main factors to be studied from the water leaching experiments comprise of pH, solid-liquid ratio (g/L) and temperature (°C).

DI water was utilized as the leaching agent for the Li dissolution from spent LIB material (black mass). The experimental temperature was controlled using an external heating circulator (Julabo SE-12) connected to a three-necked jacketed reactor. A condenser was attached to the reactor to prevent evaporation of the reaction solution. A magnet was places inside the reactor for continuous agitation at 400 rmp, for all experiments. A pH meter from VMR was placed inside the reactor to control the reaction pH. The water leaching experiments were initiated by heating the solution to the desired temperature. Following, the black mass was weighed according to the desired solid-liquid ratio and placed in the reactor, as illustrated in Figure 5.2. Addition of base (NaOH) was performed as to obtain a pH of the desired one, and the reaction was kept at the decided time frame of 1 hour for all independent experiments.

Figure 5.2: 1) Water leaching setup 2) Leaching setup with black mass.

After the specified leaching time, the residue was filtered with a vacuum filtration setup and the final solution volume was measured with a measuring cylinder before being collected in bottles (Figure 5.3) for subsequent DLE experiments. 1 mL of the leached solution was further analyzed with MP-AES to determine the concentration of the dissolved metals. The filtered residue was also analysed for metal concentration with MP-AES, subsequent to SpeedWave digestion and XRD.
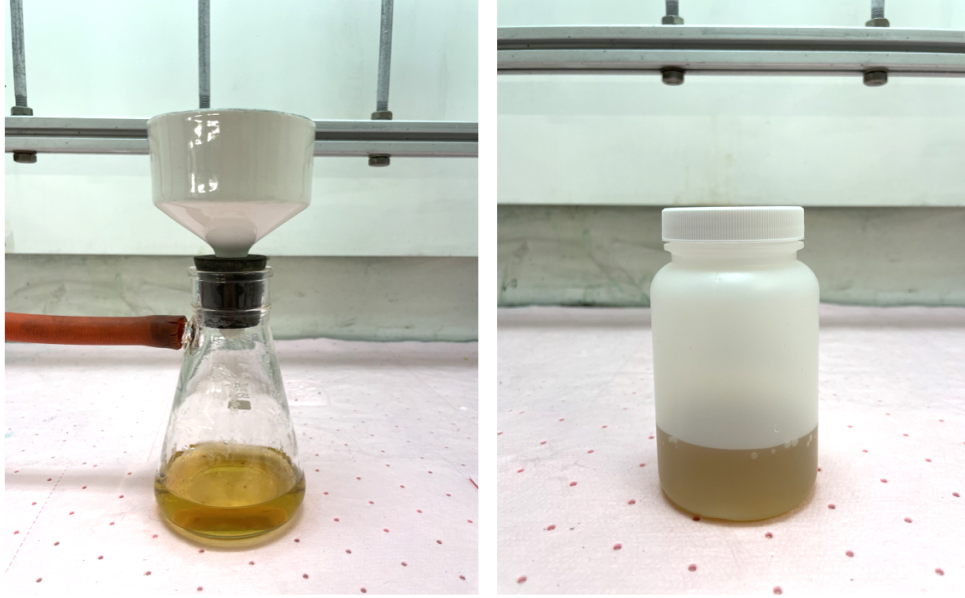
Figure 5.3: 1) Vacuum filtration setup 2) Leached solution post vacuum filtration.

A summary for the set of leaching experiments is described in Table 3, presented on the next page, specifying the varied conditions for temperature, pH and solid-liquid ratio obtained from JMP. As previously mentioned, these sets of experiments were performed with the intention to selectively dissolve Li in solution to be later used for the DLE experiments and fluoride analysis with FSE, as well as to compare the obtained results in this work, with previous work. The leaching efficiency for all performed experiments was calculated according to equation 7.

$$Leaching\ efficiency\ (\%) = \frac{C_i \cdot V}{m_0 \cdot w_i} \cdot 100 \tag{7}$$

From equation 7, C_i is the concentration of metal i in the leachate (mg/L), V is the volume of solution (L), m_0 is the weight of the black mass sample (mg) and w_i is the weight percentage of the metal i in the sample (%).

Table 3: Summary over conditions employed for water leaching experiments.

Summary of Leaching Experiments			
Exp.	Temperature (°C)	pH	s/l ratio (g/L)
1	80	6.5	20
2	80	6.5	40
3	80	6.5	150
4	80	8	20
5	80	8	40
6	80	8	150
7	80	10	20
8	80	10	40
9	80	10	150
10	60	6.5	20
11	60	6.5	40
12	60	6.5	150
13	60	8	20
14	60	8	40
15	60	8	150
16	60	10	20
17	60	10	40
18	60	10	150
19	25	10	20
20	25	10	150

5.5 Direct Lithium Extraction Studies

For the DLE, from the obtained water leached solutions described in section 5.4, adsorption through ion-exchange was investigated. The flow diagram presented in Figure 5.4 gives a description over the experimental extraction path of Li through ion exchange from the Li containing leachate. In summery, the Li containing leachate was contacted with selected ion exchange resins, Amberlite H-form and Na-form, as well as the Molecular sieve 13X zeolite. Following, the Li-depleted solution was filtered from the adsorbents and analysed with MP-AES to determine the amount of Li adsorbed from the solution. Finally, Li desorption from the ion exchange resins was performed utilizing HCl, as to obtain a solution rich in Li.
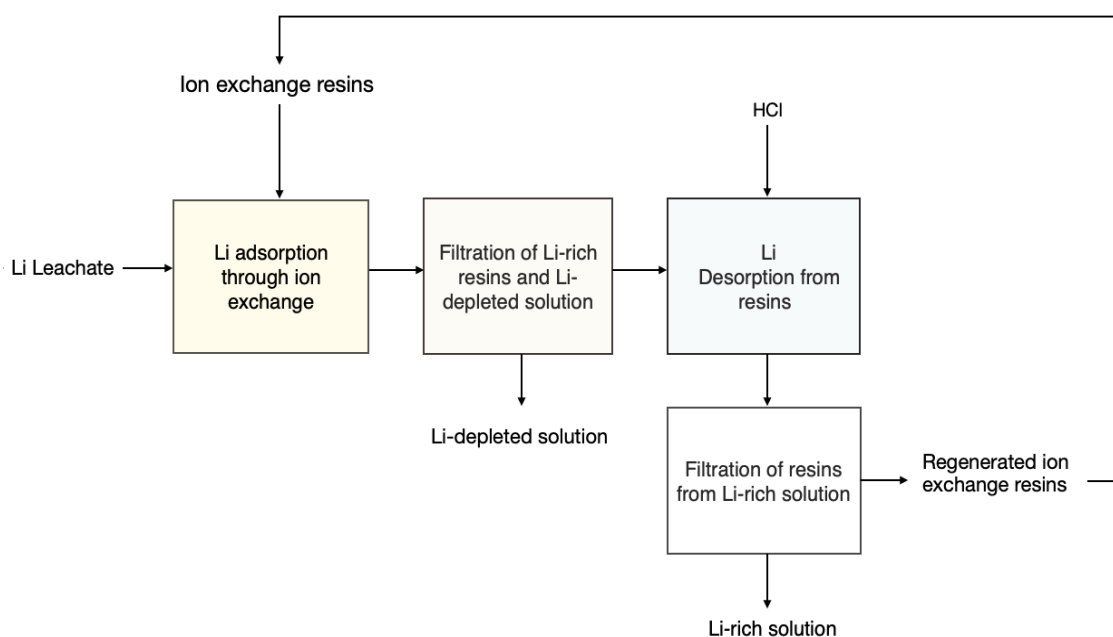
Figure 5.4: Flow chart representation over experimental path for DLE from water leachate.

In this work, three different types of experiments were performed for the DLE study; kinetic studies, to investigate the equilibrium uptake capacity and equilibrium retention yield (removal efficiency), as a function of contact time. Experiments studying the effect of increasing solid-liquid ratio. Desorption/elution studies, to determine the desorption yield and overall Li recovery from both adsorption and desorption steps. Finally, reutilization studies of the used resins to investigate the difference in performance, namely uptake capacity and retention yield.

5.5.1   Experimental Kinetic Study

Kinetic studies were performed to investigate the reaction rate of the adsorption experiments for the Amberlite H-form and Amberlite Na-form ion exchange resins and the Molecular sieve 13X zeolite. The aim of the study was to identify the reaction equilibrium, to potentially reduce the contact time for the adsorption experiments, as well as study the uptake capacity of Li and retention yield of Li from the solution onto the resins. For the investigation, the same batch setup as previously used for the water leaching experiments (section 5.4) was used, illustrated to the left in Figure 5.5.

Figure 5.5: 1) Batch reactor setup for adsorption experiments. 2) Li-depleted solution after filtration.

The kinetic study was conducted on two selected Li containing leachates, performed for solid-liquid ratios of 20 g/L and 150 g/L, both for 25°C and pH of 10, previously described from Table 3 (Exp. 19 and 20). Furthermore, the kinetic experiments were performed for a fixed temperature of 25°C and controlled using the same external heating circulator (Julabo SE-12) as for the water leaching experiments. For each experiment, 100 mL of leachate was placed into a three-necked jacketed reactor. Following, the ion exchange resins and zeolite was weighed as to obtain a solid-liquid ratio of 20 g/L and placed inside the reactor. A magnet was placed in the reactor for continuous agitation at 400 rpm and maintained in contact for 4 hours to ensure equilibrium. Small volumes of the liquid phase were regularly withdrawn with a syringe and collected for further analysis with MP-AES to monitor the decrease in Li concentration, uptake capacity and retention yield, as a function of contact time. After the specified reaction time, the Li-enriched resins and zeolite were filtered and collected for further desorption studies. The final Li-depleted solution after filtration is illustrated to the right in Figure 5.5.

The Li uptake capacity (Q) was determined from mass balance as the amount of Li retained per gram of resin, described in equation 8. C_i is the initial Li concentration (mg/L), C_f is the final (equilibrium) Li concentration (mg/L), m is the mass of resin (g) and V is the volume of solution (L). The Li retention yield was calculated from equation 9.

$$Q \ (mg/g) = (C_i - C_f)\frac{V}{m} \tag{8}$$

$$R \ (\%) = \frac{(C_i - C_f)}{C_i} \cdot 100 \tag{9}$$

5.5.2 Experimental Solid-liquid Study

To understand the effect of increasing solid-liquid ratio, on the uptake capacity (Q) and retention yield (R), studies were conducted for increasing amount of adsorbent. The solid-liquid ratio was increased from 20, 40 and 60 g/L and studied on the previously used leachates, discussed in the previous section. The same reactor setup, as for the kinetic study (Figure 5.5) was used for the solid-liquid ratio studies. The same conditions in terms of temperature (25°C) and suspension agitation (400 rpm) were used, however, the contact time was reduced to 30 minutes. After the specified contact time, the Amberlite H-form and Amberlite Na-form resins were filtered from the Li-depleted solution and stored for further desorption studies. The Li-depleted solution was analysed with MP-AES to determine the decrease in Li concentration.

5.5.3 Desorption Experiments

Following the adsorption experiments, desorption was performed on the Li-rich resins obtained from section 5.5.2. HCl was utilized for the desorption/elution of Li from the resins, to liberate the Li-ions in solution. From literature it has been recognized that the desorption yield increases for higher elution concentration, being in the range of 3-5M for HCl [45, 48]. However, with the desire to reduce the cost of operation, a more diluted concentration of acid will be preferable for larger scale operations, being more preventative for the equipment and environment. It was therefore decided to utilize a 1M HCl solution for the desorption experiments in this work.

The same reactor setup as described in section 5.5.1 and 5.5.2, was used for the desorption experiments, for the same reaction conditions in terms of temperature (25°C) and agitation (400 rpm). 100 mL of 1M HCl was contacted with the Li-rich resins in the same three-necked jacketed reactor used in previous experiments, for a contact time of 30 minuets. Following, subsequent filtration of the desorbed resins from the Li-enriched solution was performed. The desorbed resins were further washed with MQ water, dried and stored for further reutilization studies.

The Li-enriched solution, after desorption with HCl was further analysed with MP-AES to determine the Li desorption yield (equation 10) and the overall Li recovery yield (equation 11).

$$Li_{desorption} \ (\%) = \frac{C \cdot V_{acid}}{Q \cdot m} \cdot 100 \tag{10}$$

$$Li_{Recoverd} \ (\%) = \frac{C \cdot V_{acid}}{C_i \cdot V} \cdot 100 \tag{11}$$

From both equation 10 and 11, C is the final (equilibrium) Li concentration in the HCl solution (mg/L), Q is the Li uptake capacity for each sorbent sample (mg/g), m is the mass of sorbent (g) and V_{acid} is the volume of HCl solution (L).

5.6 Fluoride Ion Quantification with Fluoride Selective Electrode

To quantify the amount of fluoride in the utilized black mass and the leached solutions obtained from section 5.4, a fluoride selective electrode from Metrohm was used. Fluoride selective electrodes are efficient for measuring the fluoride concentration in solution and have a wide concentration measurement range [49]. The electrode is operated by converting activity of fluoride ions dissolved in solution into an electrical potential. The electrical potential is then compared to a calibration curve made with known fluoride concentration. The measured solution activity from the electrode is related to Nernst equation, described in equation 12. From the equation, E is the potential, E^0 is the characteristic constant of the fluoride selective electrode, R is the gas constant, n is the ionic charge, F is the Faraday constant and a is the activity. The ionic charge of fluoride is -1, meaning that the theoretical slope of the calibration curve is -59.16, at ambient temperature [49].

$$E = E^0 + 2.3 \frac{RT}{nF} log(a) \tag{12}$$

For the calibration curve, a standard solution of fluoride with a concentration of 1000 mg/L was series diluted as to obtain solutions of 500 mg/L, 250 mg/L, 100 mg/L, 50 mg/L, 25 mg/L, 10 mg/L, 1 mg/L and 0.1 mg/L. 15 mL of each diluted solution was mixed with 15 mL total ionic strength adjustment buffer (TISAB II), yielding samples of known concentration for the calibration curve. For the fluoride determination of the obtained samples from section 5.4, 15 mL of solution was mixed with equal amounts of TISAB II and subjected to electrode potential measurements. The fluoride concentration was calculated using the obtained equation from the calibration curve.

TISAB II was prepared by weighing out 8 g of CDTA, 116 g NaCl and measuring out 114 mL of acetic acid. This was further mixed and diluted to 1 L solution with MQ water. The mixture pH was adjusted to 5.4 using 5M NaOH and then diluted with MQ water as to obtain a total volume of 2 L.

Chapter 6

Results and discussion

In this chapter, results obtained from chapter 5 will be presented, following the same chronology as the associated flow chart presented in Figure 4.1.

6.1 Black mass Quantification

6.1.1 Composition of Black mass

Black mass from the spent electrode material (pre-treated EOL LIBs) were used in the water leaching experiments, described in section 5.4. To calculate the leaching efficiencies of the experiments, a determination of the metal composition had to be performed. For this, both microwave assisted digestion and manual digestion was performed prior to analysis with MP-AES. The procedure for the two digestion experiments were described in section 5.3. The bar charts in Figure 6.1, as well as the values in Table 4, represent the metal composition in weight percent, of the initial black mass from the spent pre-treated LIBs.
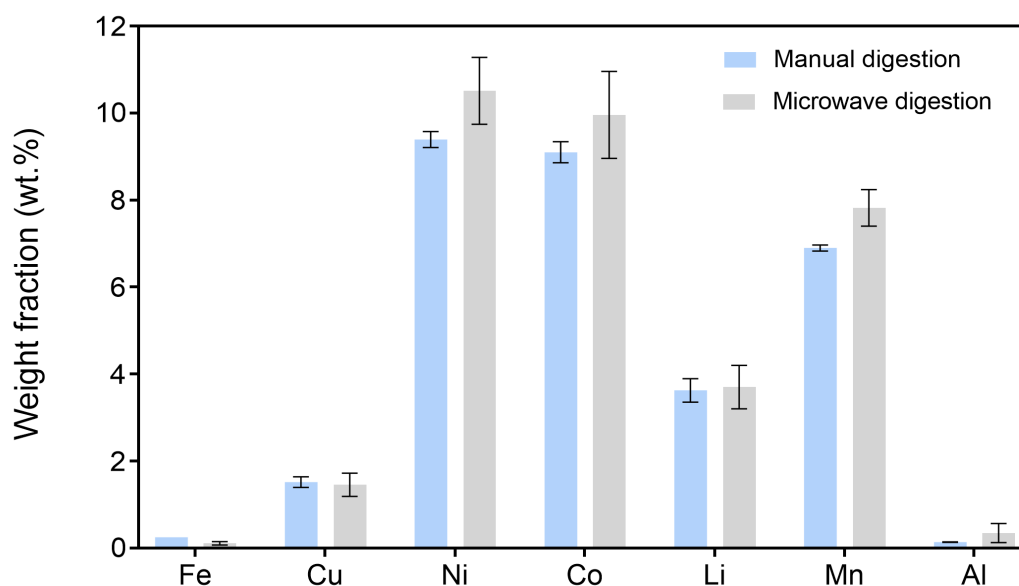
Figure 6.1: Black mass metal weight percentage from manual digestion and microwave assisted digestion.

Table 4: Black mass metal composition from microwave assisted digestion and manual digestion.

Black mass metal composition (wt.%) from MP-AES						
Method	Fe	Cu	Ni	Co	Li	Mn	Al
Manual	0.25 ± 0.0	1.52 ± 0.12	9.39 ± 0.18	9.1 ± 0.24	3.63 ± 0.27	6.9 ± 0.07	0.14 ± 0.0
Microwave	0.11 ± 0.04	1.46 ± 0.27	10.51 ± 0.77	9.96 ± 1.00	3.70 ± 0.50	7.82 ± 0.42	0.35 ± 0.22

The metal weight percentages (wt.%), for both the microwave assisted and manual digestions are averages from three samples obtained by using the same amount of solids ($\sim$ 0.5 g) in each digestion. As can be seen from the charts in Figure 6.1, both digestion methods are in good agreement with each other, however, the standard deviation for the microwave assisted digestion is significantly larger compared to the set of manual digestions. This may be a result of sample loss during filtration, leading to more inconsistent values.

From Figure 6.1 and Table 4, it is evident to see that Ni, Co and Mn are the dominating metals present in the black mass, with similar wt.%. This similarity indicates that the cathode material is of the NMC class, previosluy discussed in section 1.1 [5]. The lower wt.% of Co and Mn, compared to Ni, may be attributed to the digestion not being performed in the presence of a reducing agent (H_2O_2), yielding a lower dissolution of Co and Mn due to the lowly soluble Co^{3+} and Mn^{4+} [2]. A part from the dominating metals, Li is in abundance, originating from the CAM and conductive salt of the electrolyte. The minor metals, Cu and Al are traces of the Al cathode current collector and Cu anode current collector, whereas Fe is an impurity originating from the battery steel casings. The remaining wt.% are predominately carbon, in the form of graphite, along with fluoride, sulphur and phosphor from cell casings, binders and electrolytes [5].
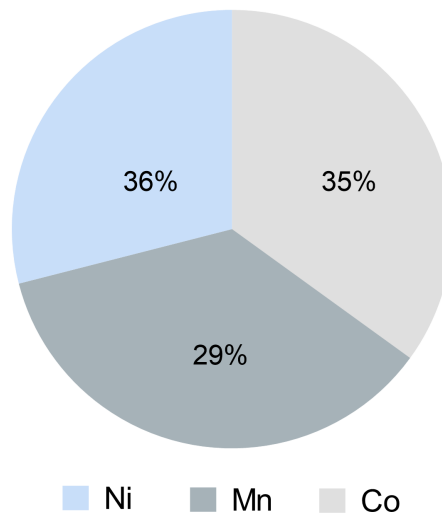
Figure 6.2: Molar ratio of Ni, Mn and Co in utilized black mass from MP-AES.

The quantity of metals in black mass determine the type of cathode. The cathode mixed metal oxide is used to name the batteries based on the metal molar ratios. As a further investigation of the cathode material, the metal composition was used to establish the molar ratio between Ni, Mn and Co for the NMC cathode type prediction. The pie chart illustration in Figure 6.2 represent the molar ratio of Ni, Mn and Co in the black mass obtained from the MP-AES analysis, yielding the molar ratio of $Ni_{0.36}Mn_{0.29}Co_{0.35}$. All data presented in this section, including the obtained results for the manual and microwave assisted digestion, are listed in Appendix A.

6.1.2 Phase identification

XRD analysis of the initial solid black mass utilized in the experimental procedures was conducted, where the measurement conditions for crystalline samples was described in section 5.2. The resulting XRD pattern from the ICDD database is presented in Figure 6.3. The XRD phase identification confirms that the initial black mass comprise of the mixed metal oxide $LiNi_{0.33}Mn_{0.33}Co_{0.33}O_2$ (PDF 00-062-0431) cathode material and of carbon (PDF 00-056-0159) from the graphite anode. It is also clear to see that the predominant phase of $LiNi_{0.33}Mn_{0.33}Co_{0.33}O_2$ (sharp peak at $2\theta = 18.751$) confirm that the crystal structure of the CAM is retained post mechanical treatment.
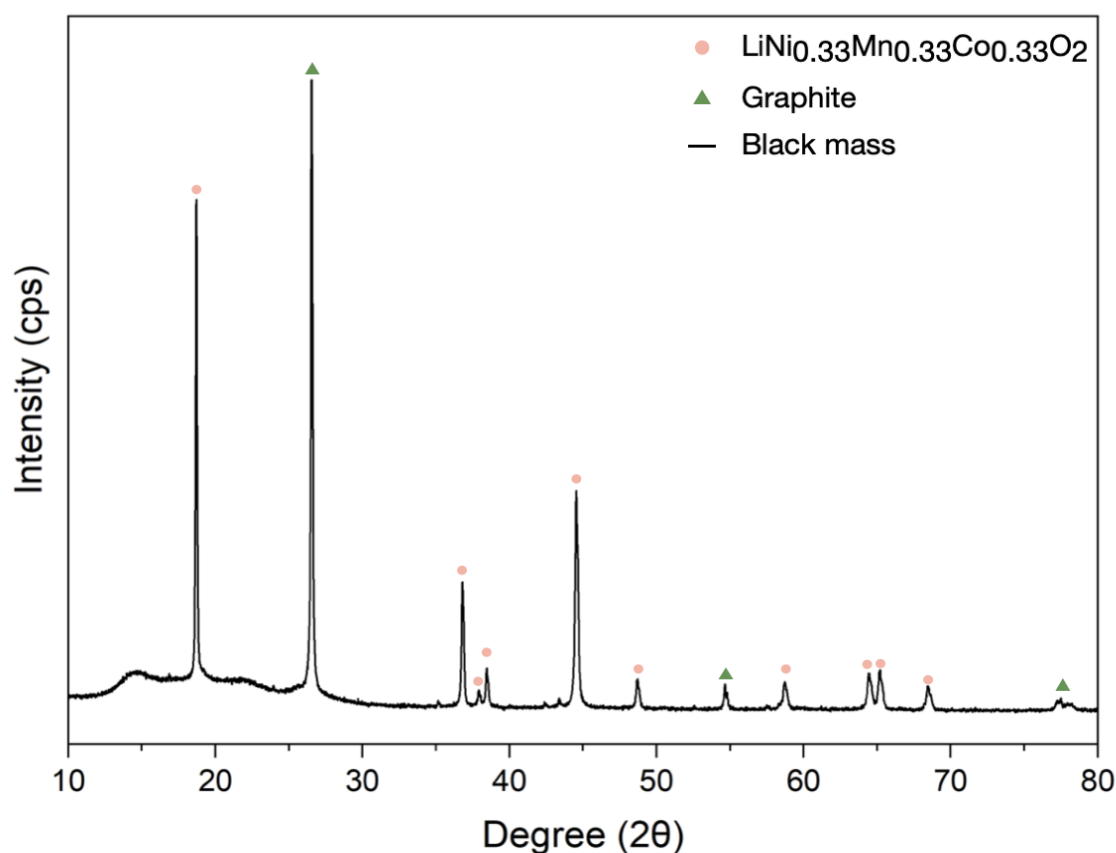
Figure 6.3: XRD pattern of initial solid black mass.

The phase identification from the XRD pattern are agreeing with the calculated molar ratios obtained form the MP-AES analysis, confirming the elemental ratio of Ni, Mn and Co to the $N_1M_1C_1$ cathode material. From the previously discussed metal ratios in section 6.1.1, it is also evident that the XRD pattern correlate with the previously discussed MP-AES results, with minor differences in wt.%, most likely due to the inhomogeneity of each sample and also as a result of dissimilar sample preparations. Furthermore, the lack of use of a reducing agent also affect the dissolution of Mn and Co, as explained in previous sections. For the digested samples, metal loss during preparation and filtration is likely, resulting further in minor differences for the two analytical methods.

The filtered residue, post digestion with aqua regia, was also examined to investigate if all the metals had digested properly. Figure 6.4 illustrates the comparison between the resulting digested XRD pattern (red) as well as the initial black mass powder from the ICDD database, discussed previously above. As seen from the pattern for the digested black mass, the predominant peaks presented are the ones for graphite (PFD 00-056-0159). The XRD phase identification for the digested black mass confirm that most the metals from the initial black had been properly digested, leaving mainly graphite in the filter.
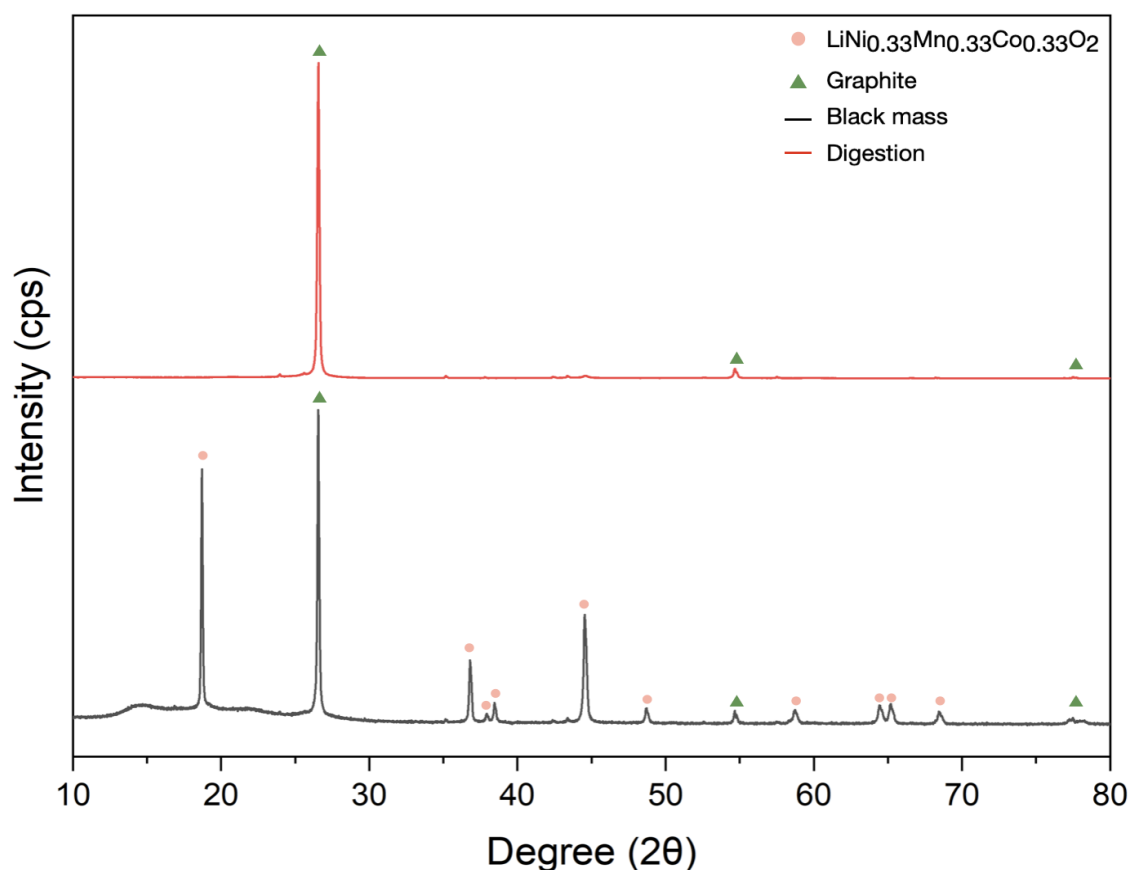
Figure 6.4: XRD pattern of digested black mass (red) and initial black mass (black).

6.1.3   Particle Morphology of Spent Electrode Material

SEM images were taken to further investigate the particle morphology of the utilized black mass. The measurement conditions for the SEM images were detailed in section 5.2. The samples were prepared by applying a small amount of the black mass power on a conductive tape, before analysis with SEM. Figure 6.5 shows the top-view SEM images of the utilized black mass, originating from spent NMC batteries for 50, 20, 10 and 5 µm.
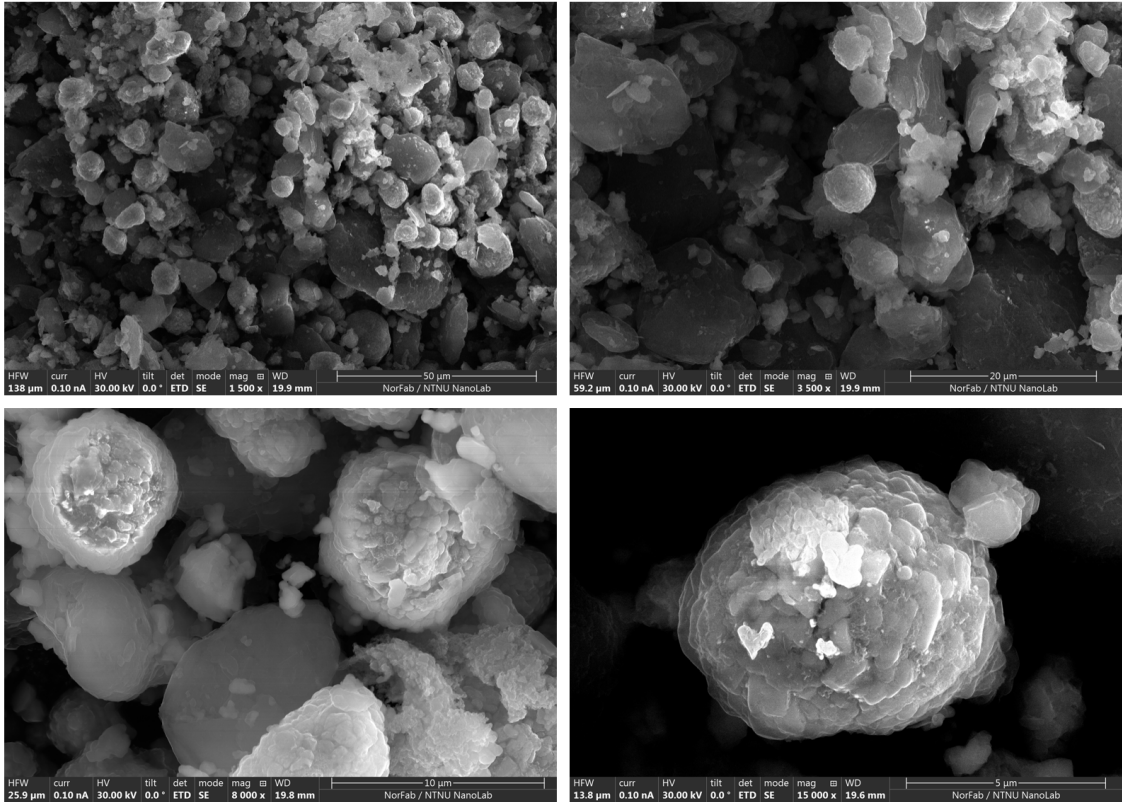
Figure 6.5: SEM images of utilized black mass for varied magnification.

From the first two SEM images on top, it is evident to see that the larger particles have formed aggregates with the smaller particles. From literature it has been taught that the aggregation is caused by the residual binder, leading to the formation of larger particles when the batteries are being crushed [50]. The high magnification SEM images on the bottom reveal small spheres in the range of $\sim$ 5–10 µm, comprising of much smaller particles. This assembly of spheres can be attributed to the spent cathode material, i.e., Ni, Mn and Co. Additional EDS mapping was performed on the spherical particles, confirming the presence of NMC metals, namely Ni, Mn and Co, which can be found in Appendix E. Furthermore, spherical grain orientation may arise from the hexagonal structure of NMC particles. The hexagonal unit cell allows for 12 possible symmetrical orientations, potentially explaining the variation in particle morphology, seen from the low magnitude images on the top [51]. The layered and more darker shaded particles correspond to the amorphous graphite [50].

6.2   Water Leaching

The fundamental theory behind the leaching unit operation was described in chapter 2. As previously declared, water leaching was employed with the aim to selectively dissolve Li in solution. The experimental water leaching procedure was described in section 5.4 and the main findings will be presented and discussed in the following section.

6.2.1   Effect of solid-liquid ratio and Temperature on Lithium Dissolution

The DOE for the selective leaching of Li was described previously in Table 3, defining the varying parameters, namely solid-liquid ratio, pH and temperature. From previous studies, it was recognized that the Hydro black mass gave acidic pH in water [36]. The acidic nature of the Hydro black mass may be a direct result of the black mass not being pyrolysed, only dried at $\sim 200°C$, which has proven to enhance the recovery of CAMs due to decomposition, leaving the leftover soluble organic electrolyte to remain in the black mass [22, 23]. Therefore, it was decided to alter the pH with the addition of NaOH, to obtain a more selective dissolution towards Li. Figure 6.6 presents the Li concentration (mg/L) against solid-liquid ratio, to the left, and Li leaching efficiency (%) against solid-liquid ratio to the right, for 25°C, 60°C and 80°C, respectively, for a pH 10, described from Table 3 in section 5.4.
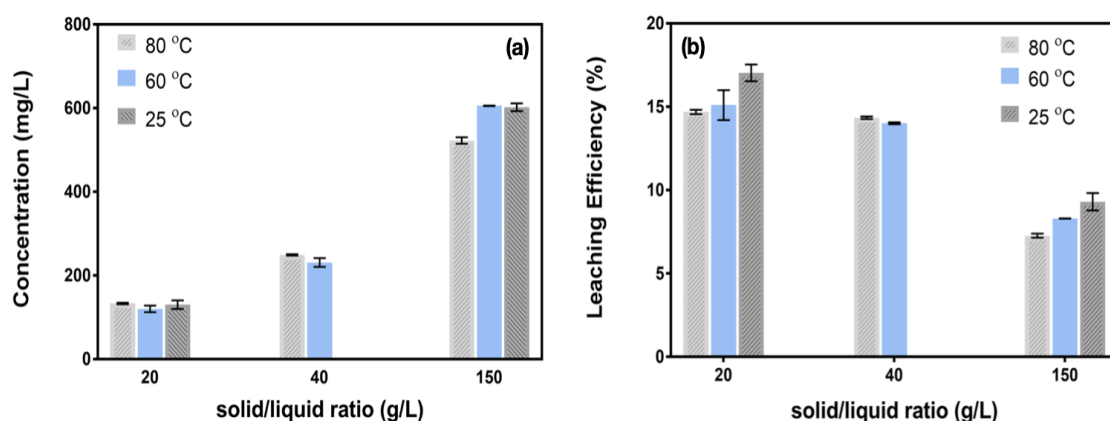
Figure 6.6: (a) Li concentration (mg/L) against solid-liquid ratio (g/L) and (b) Li leaching efficiency (%) against solid-liquid ratio, both for pH 10, at 25°C (grey), 60°C (blue) and 80°C (light grey).

As can be seen from the left charts in Figure 6.6 (a), the concentration of Li in the leachate increases with increasing solid-liquid ratio. The Li concentration starts from 134.4 mg/L for a solid-liquid ratio of 20 g/L, and increases to 528 mg/L for a solid-liquid ratio of 150 g/L, for a temperature of 80°C. The same increasing trend, for a increased solid-liquid ratio is also observed for 60°C, initially starting at 126 mg/L and reaching 606 mg/L, for solid-liquid ratios of 20 g/L and 150 g/L, respectively.

Furthermore, for 25°C, no significant difference in terms of Li dissolution was observed, yielding a final Li concentration of 131.4 mg/L for a solid-liquid ratio of 20 g/L, and 602 mg/L for a solid-liquid ratio of 150 g/L. This finding was also observed by Léa et.al, where it was recognized that there was no significant increase or change in the dissolution of Li for higher temperatures [23]. From this observation it can be acknowledged that the effect of temperature had negligible effect on the dissolution of Li during water leaching, having the potential to significantly reduce the overall energy demand for the leaching process.

However, as the solid-liquid ratio increases, from 20 g/L to 40 g/L and 150 g/L, the leaching efficiency decreases. From the right charts, in Figure 6.6 (b), it is evident to see that the leaching efficiency declines slightly from 14.69% for a solid-liquid ratio of 20 g/L, to 7.27% for a solid-liquid ratio of 150 g/L, at 80°C. The same observation was confirmed for a temperature of 60°C, where the initial leaching efficiency for a solid-liquid ratio of 20 g/L yielded 15.10%, and declined to 8.30% when the ratio was increased to 150 g/L. This reduction in leaching efficiency can be attributed to the reduced contact area between the solid black mass and water, for higher solid-liquid ratios, yielding a reduced leaching efficiency [23]. Furthermore, from literature it has been found that the leaching efficiency of a thermally treated black mass, either thorough pyrolysis or incineration, has a positive effect on the leaching efficiency [23, 52, 53]. From the study of Léa et.al it was confirmed that the efficiency of Li increased to 62% for a solid-liquid ratio of 20 g/L, after pyrolysis at 700°C, as a result of CAM decomposition, explaining the lower efficiencies obtained in this work [23].

Moreover, for 25°C, the leaching efficiency was slightly higher compared to 60°C and 80°C, yielding 17.04% for a solid-liquid ratio of 20 g/L, as a result of minimal evaporation of water during the leaching experiment. The same observation in terms of reduced leaching efficiency when the solid-liquid ratio is increased to 150 g/L, for 25°C, can be observed from Figure 6.6 (b), yielding 9.32%, as a result of reduced contact area between the black mass powder and the water. This observation, for the same temperature conditions of 25°C and pH of 10 were also achieved from previous studies, yielding 15.20% for a solid-liquid ratio of 20 g/L and further reducing to 11.90% when the solid-liquid ratio was increased to 150 g/L. From the previous studies it was further concluded that the Li leaching efficiencies at 25°C and 80°C were similar, agreeing with the results obtained in this work [36].

In spite of the fact that a low solid-liquid ratio of 20 g/L yielded the highest leaching efficiency, a higher solid-liquid ratio is more favourable in terms of higher Li concentration in the leachate. From an industrial point of view, utilizing a moderate solid-liquid ratio, will yield sufficient production capacities and acceptable recoveries of Li in solution. The MP-AES data for the obtained metal concentrations (mg/L) in the leachates, for all experiments described from Table 3, can be found in Appendix B.2. The data for the calculated leaching efficiencies, from equation 7, can be found in Appendix B.4, including a calculation example.

6.2.2 Investigating Replicability and pH effect on Lithium Dissolution

From the previous section, it was acknowledged that the concentration (mg/L) of Li in solution increased for increasing amounts of black mass (solid-liquid ratio) utilized. However with increasing solid-liquid ratios, a decrease in leaching efficiency was confirmed. In Figure 6.7, the concentration as a function of solid-liquid ratio, (a), and leaching efficiency as a function of solid-liquid ratio (b), is presented for temperatures 60°C and 80°C, for pH values of 6.5 and 8.
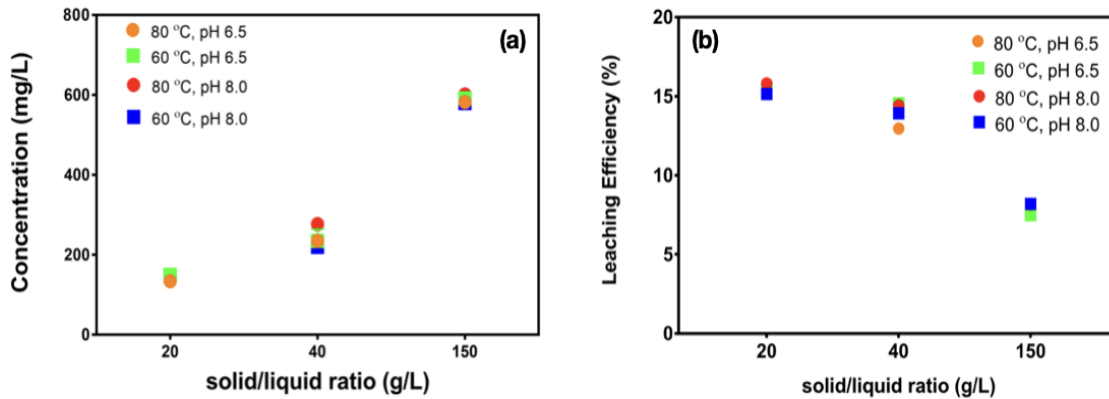
Figure 6.7: (a) Li Concentration (mg/L) against solid-liquid ratio and (b) Li leaching efficiency (%) against solid-liquid ratio, for pH 6.5 and 8 for 60°C and 80°C.

From Figure (a) and (b) it is evident to see that the result are in accordance with the ones obtained for a pH of 10, previously discussed from Figure 6.6. The same trends in terms of increasing Li dissolution can be observed for increasing solid-liquid ratio, for the lower pH values of 6.5 and 8. Furthermore, the same reduction in leaching efficiency can be acknowledged for increasing amounts of black mass utilized. This indicates that the effect of pH had negligible effect on the dissolution of Li.

For a pH of 6.5 at 80°C (orange) the dissolution of Li increases from 134.1 mg/L to 235.2 mg/L and 582 mg/L, when the solid-liquid ratio is increased from 20 g/L to 40 g/L and 150 g/L, accordingly. For a pH of 6.5 at 60°C (green) similar observations occur where the dissolution increases from 150 mg/L to 234.7 mg/L and 592 mg/L, for increased amount of black mass, confirming the negligible temperature effect on the Li dissolution. Furthermore, for a pH of 8 at 80°C (red) the dissolution sequence for increasing solid-liquid ratio was 144.1 mg/L and 279.7 mg/L and 601 mg/L. Finally, for a pH of 8 at 60°C (blue), the increasing effect on the dissolution of Li was 148 mg/L, 219.8 mg/L and 579.5 mg/L. In contrast, for an increment in solid-liquid ratio the leaching efficiency reduces from 15.49% to 12.96% and 8.12%, when the solid-liquid ratio is increased from 20 g/L to 40 g/L and 150 g/L, for pH 6.5 at 80°C (orange). Similar trends for 60°C (green) were obtained, yielding efficiencies of 15.49%, 14.54% and 7.48%, for the underlined solid-liquid ratios. Finally, for a pH of 8 at 80°C (red) the leaching efficiency reduced in the order of 15.81%, 14.42% and 8.17% and for 60°C (blue) the order was 15.14%, 13.91% and 8.19%, for 20 g/L, 40 g/L and 150 g/L, respectively.

These results confirm that the effect of pH had little effect on the dissolution of Li, yielding similar concentrations of Li for all the studied pH values. Furthermore, the pH effect had limited influence on the Li leaching efficiency. The effect of pH, can also be confirmed from Figure 6.8, where the concentration (mg/L) against pH has been plotted to the left (a and c), and leaching efficiency (%) against pH to the right (b and d), for the studied solid-liquid ratios. From the plots in Figure 6.8, it can be seen that the Li concentration stays relatively constant for all solid-liquid rations, irrespective of pH. This observation gives rise to the taught that the dissolved Li from the utilized black mass originates from the electrolyte (LiPF$_6$) [54]. Furthermore, the leaching efficiency for the studied pH values, stays relatively constant from pH 6.5 to 8 and 10. This confirms that the initial solid-liquid ratio (g/L), of black mass to water, is the dominating factor influencing the dissolution of Li in solution. All discussed results presented in this section are listed in Appendix B.2 and B.4.
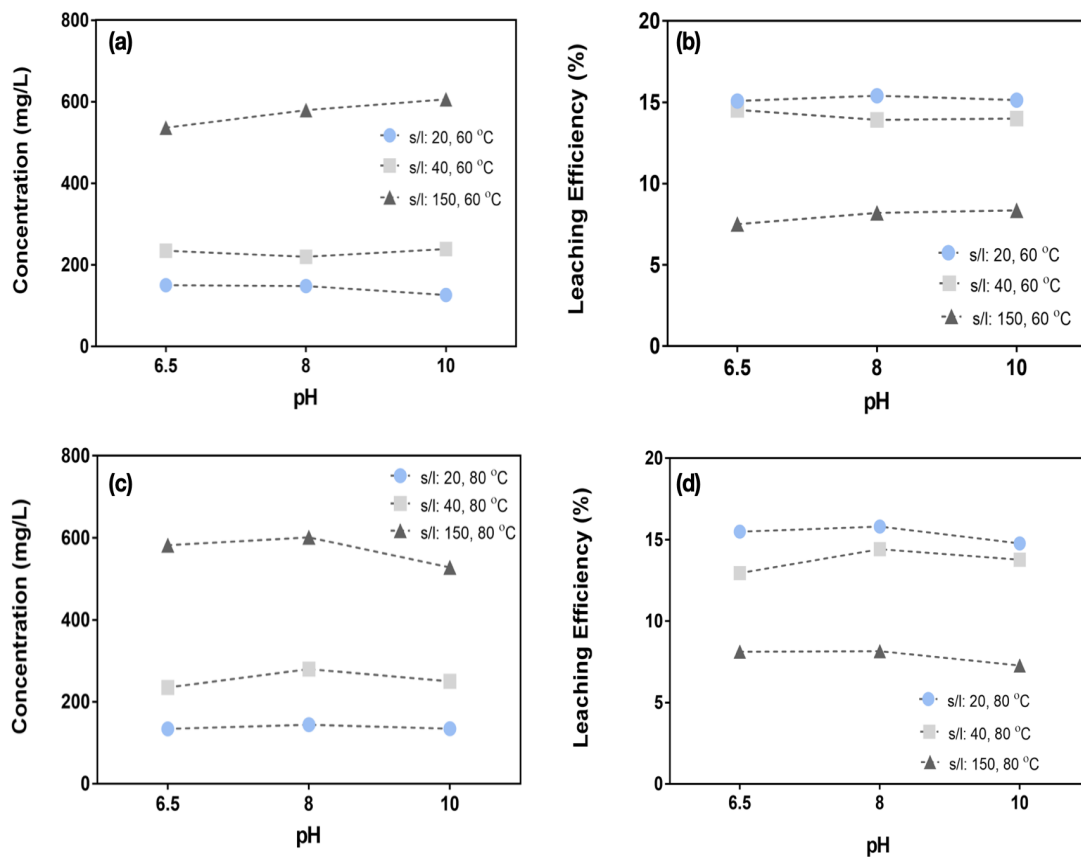
Figure 6.8: Effect of varied pH conditions (6.5, 8 and 10) on Li dissolution (a) and (c) and leaching efficiency (b) and (d) at 60°C and 80°C.

6.2.3   Effect of Metal Dissolution from Water Leaching

Commonly for most LIBs, the graphite layer is coated onto the Cu current collector, and the CAM is coated onto an Al current collector [5]. After crushing, sieving, and separation, most of the Al and Cu can be removed effectively, but there may still be small traces of Al and Co impurities in the black mass. It is therefore vital to investigate the effects of Al and Co, as well as the impurities from the other metals entrained in the black mass, for the selective recovery of Li. From the previous section, it was established that the pH had little influence on the dissolution of Li, however this does not establish that the dissolution was selective towards Li for the studied pH values. Therefore, in this section the dissolution of the other metals entrained in the black mass will be discussed in greater detail.
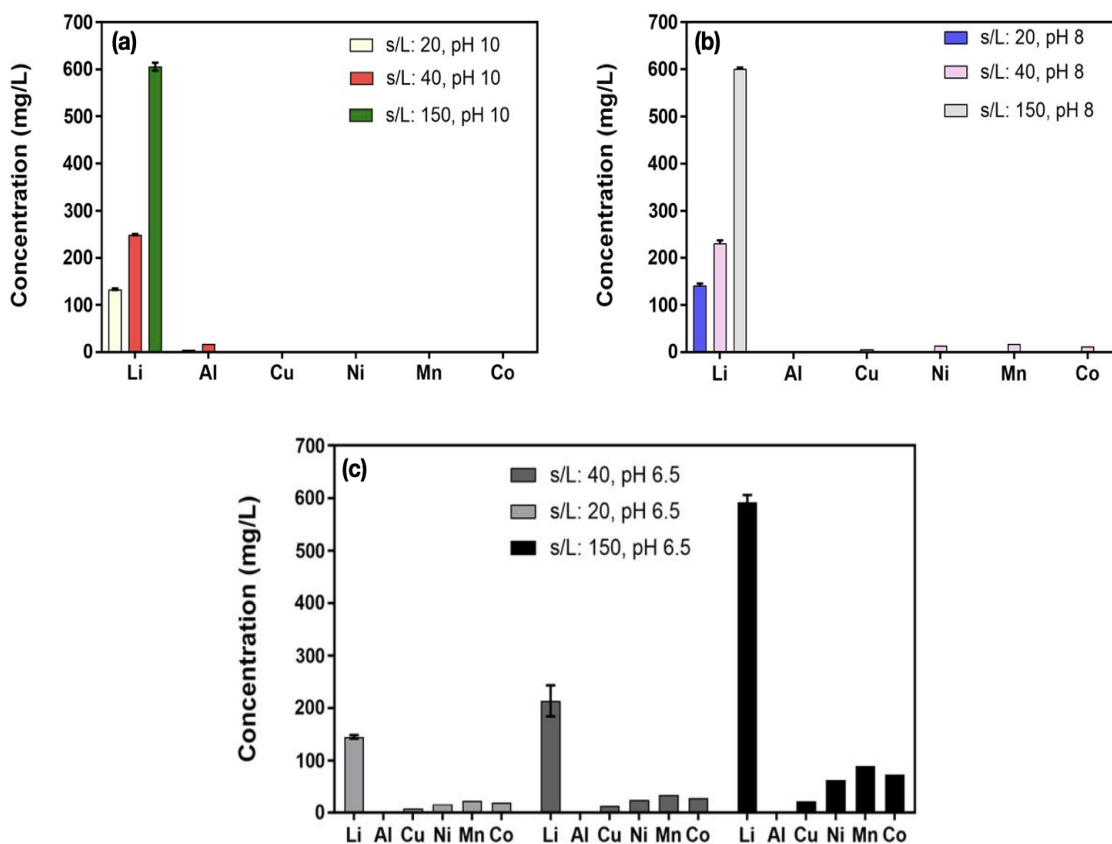
Figure 6.9: Metal dissolution from water leaching experiment. (a): pH 10 for studied s/l ratios. (b): pH 8 for studied s/l ratios. (c): pH 6.5 for studied s/l ratios.

Figure 6.9 presents the metals dissolved in solution from the preformed experiments, for different pH values and solid-liquid ratios. As can be seen from the bar charts, it is evident that Li was dissolved in majority, confirming that the leaching conditions were selective with respect to Li. From the first graph (a), the bar charts display the obtained metals in solution for the experiments conducted at pH 10 for varied solid-liquid ratios. From the charts it is evident to see that mainly Li was dissolved with minor traces of Al, leaving all the other metals (Cu, Ni, Mn and Co) in the filter residue.

41

From the studies of Léa et.al, traces of Al were also detected from their water leaching studies, observing that the dissolution of Al was lower compared to Li. However, with increasing contact time, it was established that the dissolution of Al increased due to slower Al kinetics, compared to Li [23]. This observation is important as it could lead to a more selective leaching towards Li by shortening the contact time and thus avoiding the extraction of Al. Furthermore, as explained in section 5, NaOH was utilized to adjust the pH for a more selective recovery of Li in solution. From literature it has been recognized that alkaline leaching with NaOH targets the dissolution of Al metal from the cathode current collector. The dissolution mechanism of the Al current collector can be described from equation 13 and 14 [54].

$$2Al + 2NaOH + 2H_2O \rightarrow 2NaAlO_2 + 3H_2 \tag{13}$$

$$Al_2O_3 + 2NaOH + 2H_2O \rightarrow 2NaAlO_2(OH)_4 \tag{14}$$
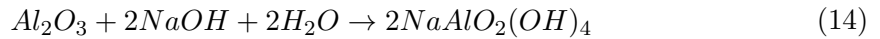
Moreover, Ferreira et.al, studied the effect of NaOH concentration on Al dissolution and observed that for an increasing alkali concentration, a significant amount Al was dissolved [54, 55]. This statement is in accordance with the results presented in (a), for the water leaching experiments performed at pH 10, and figure (b), for the experiments performed at pH 8. However, for the experiments performed at a pH of 8, small traces of Ni, Mn, Co and Cu dissolved in solution, barley detectable from the bar charts in (b).

From the results presented in the bottom centre (c), for the experiments conducted at pH 6.5, small traces of Cu, Ni, Mn and Co for all solid-liquid ratios was detected, along with Li being the majority metal in all cases. This observation is a result of the enhanced solubility of Cu, Ni, Mn and Co in acidic pH condition, previously discussed in section 2.1. However, as can be seen from all three plots, in Figure 6.9, the dissolution of Li was superior for all pH values, compared to the dissolution of the other metals entrained in the black mass.

For future applications, a pH of 10 would be the most favourable for the selective dissolution of Li in solution, to avoid the dissolution of other metals entrained in the black mass. However, a pH of 10 necessitate a higher usage of NaOH, potentially resulting in excessive solvent usage and a more Na-contaminated solution, compared to the experiments performed for lower pH. Moreover, the previous temperature study (section 6.2.1) exposed that increasing temperatures had negligible effect on the dissolution of Li, signifying that the leaching experiments can be performed at 25°C and also having the potential to significantly reduce the energy demand for the leaching process. Furthermore, for higher utilized solid-liquid ratios, higher concentration of Li was dissolved in the leachate, but the Li recovery reduced as a result of the reduced contact area between the solid black mass and the water.

6.2.4   Water Leaching Filter Residue Phase Identification

Phase identifications with XRD was performed on the dried filter residue following the water leaching experiments to investigate the effect on the crystalline structure. The same measurement conditions as for the crystalline samples discussed previously in section 5.2 were used for the filter residue characterization. The resulting XRD pattern for the water leached filter residue is presented in red in Figure 6.10, from the ICDD database. The same pattern was obtained for all independent filter residues acquired from all the water leaching experiments.
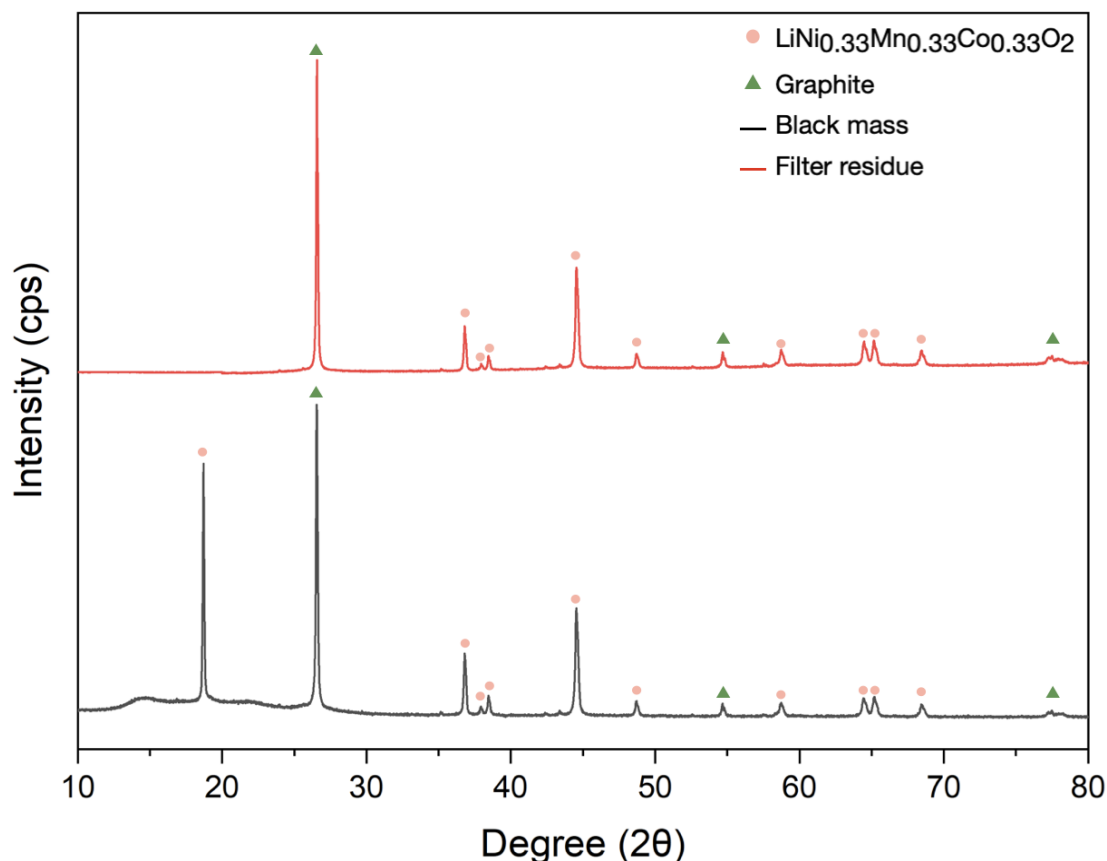
Figure 6.10: XRD pattern of filtered residue post water leaching experiments.

From the XRD pattern above, it is evident to see that most of the mixed metal oxide cathode material, $LiNi_{0.33}Mn_{0.33}Co_{0.33}O_2$ (PDF 00-062-0431), remained unchanged post water leaching, compared to the initial XRD pattern of black mass illustrated in black and previously discussed in section 6.1.2. However, the previously observed peak at $2\theta = 18.751$, seen from the XRD pattern of black mass, was no longer present in the water leached filter residue. This identification is a result of the selective leaching targeting the dissolution of Li during water leaching, confirming that Li was dissolved in solution. Furthermore, it is evident to see that the carbon (PDF 00-056-0159) from the graphite anode remained unreacted, confirmed by the peaks at $2\theta = 27$, $2\theta = 55$ and $2\theta = 78$ (green).

43

6.3 Fluoride Quantification

As was established in the introduction of this work, the fluoride compounds primarily originate from the LIB electrolyte ($LiPF_6$), along with the PVDF binder in the active electrode material. At elevated temperatures, the fluoride amount in the electrolyte, and to some degree, the PVDF binder, may form hazardous gases such as hydrogen fluoride (HF), phosphorus pentafluoride (PF_5) and phosphoryl fluoride (POF_3) [56, 57]. The decomposition of ($LiPF_6$) is promoted by the presence of water according to the following reactions;

$$LiPF_6 \longrightarrow LiF + PF_5 \tag{15}$$

$$PF_5 + H_2O \longrightarrow POF_3 + 2HF \tag{16}$$

$$LiPF_6 + H_2O \longrightarrow LiF + POF_3 + 2HF \tag{17}$$
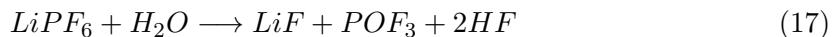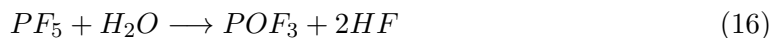
In addition to these concerns, the presence of water soluble fluoride can impose problems further down the process line, during metal recovery from solution. It is therefore imperative to investigate the amount of fluoride dissolved in the water leached solutions, as well as to identify the crucial parameters promoting the dissolution.

6.3.1 Fluoride Detection with FTIR

FTIR was used to investigate the potential fluoride peaks in the black mass, utilized in the experimental work. For the potential fluoride detection, PVDF was also analysed to determine the fluoride-containing peaks from the binder. Additionally, FTIR analysis on a pyrolyzed black mass was conducted, as it has been recognised from literature that the fluoride decomposes at temperatures above 400°C, resulting in no fluoride peaks in the FTIR spectra [58–60]. Furthermore, the filter residue following the water leaching experiments was investigated with FTIR to study the potential fluoride peaks.

As can be seen from the obtained FTIR spectra, in Figure 6.11, the characteristic peaks for PVDF (light blue) are in the wavenumber region of 763 to 1200 cm^{-1}. From literature the absorption band at 763 cm^{-1} is related to the in-plane bending or rocking vibration in the α phase. The band at 840 cm^{-1} is the stretching in β or γ phase, for the mixed mode of -CH$_2$ rocking and -CF$_2$ asymmetric stretching. The long band at 1173 cm^{-1} is associated to the symmetrical stretching of -CF$_2$ [61, 62]. From the dark blue spectra, associated with the utilized black mass in this work, small traces of -CF$_2$ can be detected for the band at 1070 cm^{-1} (marked in green box), being the α phase for the band at 1173 cm^{-1}. Furthermore, a small peak at 835 cm^{-1} was identified, potentially relating to the β or γ phase, for the mixed mode of -CH$_2$ rocking and -CF$_2$ asymmetric stretching.

From the spectra of the pyrolysed black mass (red), no peaks for the -CF$_2$ band in the marked region are detected, potentially confirming the decomposition of fluoride from the FTIR spectra. The spectra of the dried filter residue (pink) from the water leaching experiments displayed no traces of fluoride in the α phase at 1070 cm^{-1}, for -CF$_2$, but the same peak at 835 cm^{-1} was identified, for a reduced intensity compared to the black mass, potentially revealing that some fluoride from the left over PVDF binder was dissolved in solution post water leaching.
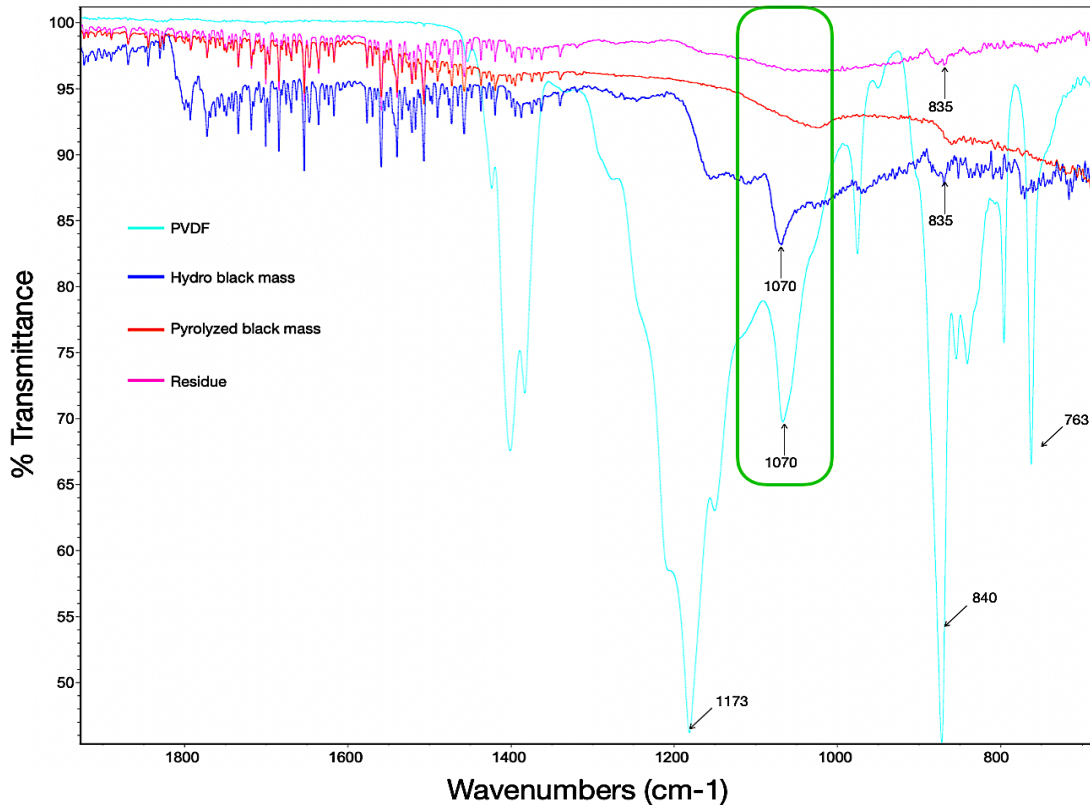
Figure 6.11: FTIR spectra.

As previously discussed, the battery electrolyte (LiPF$_6$) is another source of fluoride entrained in the black mass. From literature, inspections of the P-F modes at 840 cm^{-1} have been associated with the PF$_6^-$ origination from the LiPF$_6$ electrolyte [63]. From the spectra of the utilized black mass, the previously discussed peak at 835 cm^{-1} could also be attributed to the P-F modes originating from the LiPF$_6$ electrolyte [63]. However, the FTIR spectra above, is not sufficient enough to quantify the amount of fluorides in the water leachates and the utilized black mass, having greater potential to serve as a qualitative method for the potential detection of fluoride. For that reason, further investigation with a FSE was performed, to quantify the amount of fluoride in the black mass and obtained water leachates. This will be discussed in greater detail in the upcoming section.

6.3.2 Fluoride Ion Quantification

As described in section 5.2, a FSE from Metrohm was used to determine the concentration of fluorides in the initial black mass powder and water leached solutions. The experimental procedure for the fluoride digestion of black mass was described in section 5.3.3. Furthermore, the procedure for constructing the calibration curve, as well as TISAB II preparation was depicted in section 5.6.

The obtained calibration curve in this work is presented in Figure 6.12, including the equation from the experimental data points. The obtained slope from the equation, -59.13, is agreeing with the theoretical slope of -59.16 for fluoride at ambient temperature [49]. Accordingly, the obtained equation was used to determine the concentration of fluoride in the water leachates and utilized black mass.
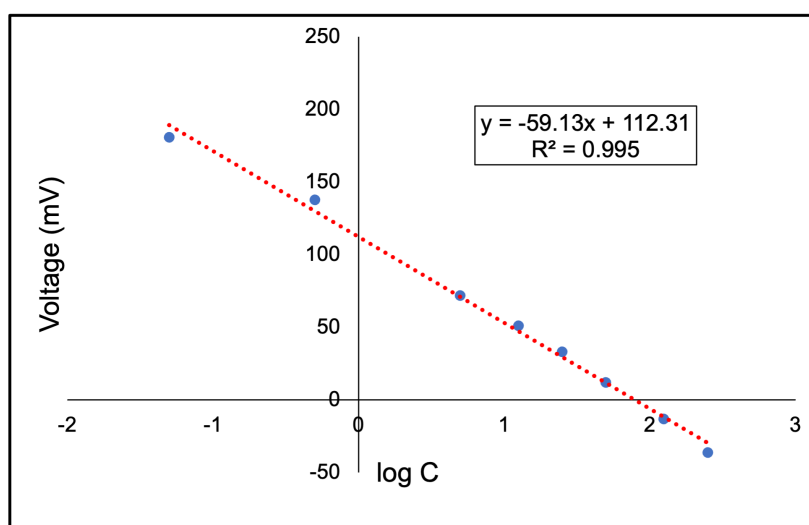
Figure 6.12: Calibration curve for FSE.

The amount of fluoride dissolved in the water leached solutions are presented as bar charts in Figure 6.13, arranged according to solid-liquid ratio (g/L), pH and temperature (°C). From the carts, a visual trend in rising fluoride concentration (mg/L) is identified for increasing solid-liquid ratio. Furthermore, a slight increase in concentration, for higher temperature is observed, from 60°C to 80°C. The effect of increasing temperatures has shown to promote the dissolution of fluorides in the solution, agreeing with the observations seen in this work [64].

Moreover, an increase in fluoride concentration was observed for increased pH, giving a fluoride concentration of 330 mg/L, 367.87 mg/L and 396.2 mg/L for pH 6.5, 8 and 10, respectively, for a solid-liquid ratio of 20 g/L and temperature of 60°C. Additionally, for 80°C, the fluoride concentration was 385.47 mg/L, 423.24 mg/L, and 483.5 mg/L, for pH 6.5, 8.0 and 10, for a solid-liquid ratio of 20 g/L. These observations are in agreement with work presented in literature, where a high correlation between fluoride enrichment and alkaline pH has been established [65, 66].

For a solid-liquid ratio of 40 g/L, 637.03 mg/L, 742.52 mg/L and 810.90 mg/L of fluoride was dissolved for pH 6.5, 8.0 and 10 for 60°C. Moreover, for a solid-liquid ratio of 40 g/L and 80°C, 724.38 mg/L, 849.79 mg/L and 918.0 mg/L was dissolved, for pH 6.5, 8.0 and 10, respectively. This demonstrates that for increasing solid-liquid ratios of black mass, a higher dissolution of fluoride can be observed, being accelerated for higher temperatures and higher alkalinity. The highest dissolution of fluoride was observed for a black mass to water ratio (solid-liquid ratio), of 150 g/L. The fluoride concentration was 1524 mg/L, 1706.20 mg/L and 1844.39 mg/L for a temperature of 60°C and pH of 6.5, 8.0 and 10, respectively. Additionally the concentration of fluoride for 80°C reached 1596.90 mg/L, 1773.95 mg/L and 1932.62 mg/L. This confirms that the highest dissolution of fluoride was achieved for a solid-liquid ratio of 150 g/L for a temperature of 80°C and pH of 10.
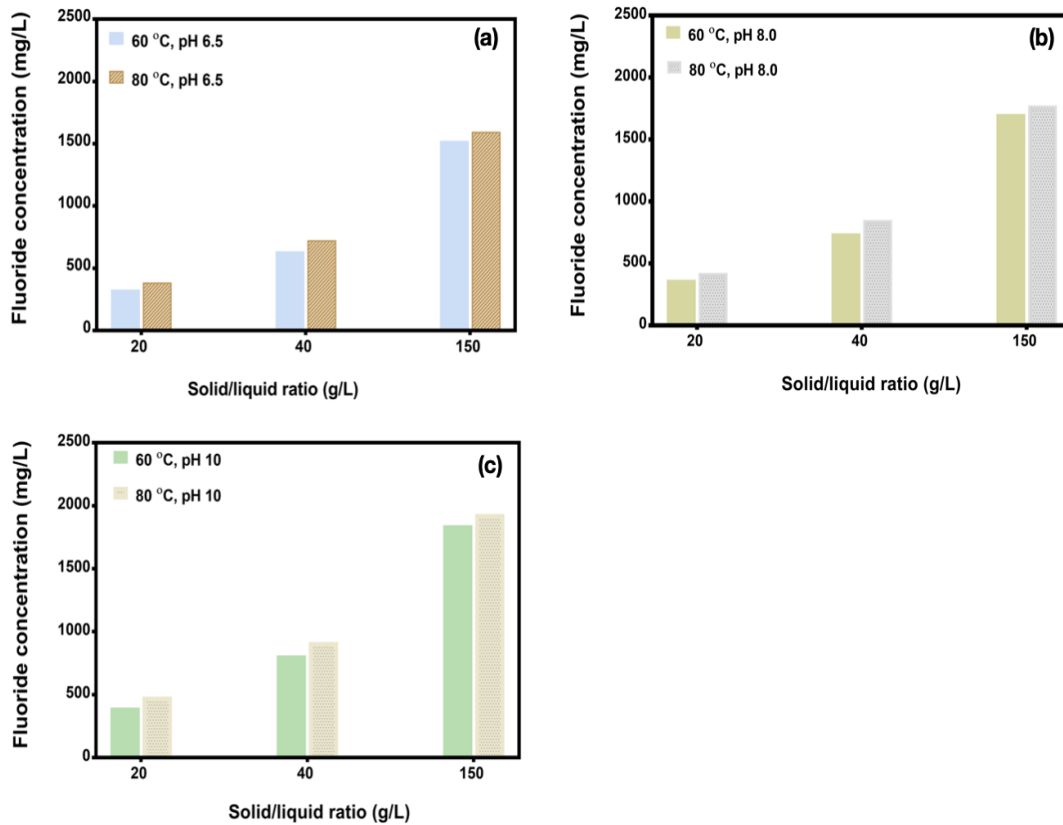
Figure 6.13: Concentration of fluoride (mg/L) in water leachates as a function of solid-liquid ratio (g/L), temperature (°C) and pH.

Furthermore, a high correlation between the dissolution of fluoride and the presence of sodium ions (Na^+), has been reported in literature [65, 66]. As previously explained, NaOH was utilized for pH adjustments during the water leaching experiments, from pH 6.5 to 8.0 and 10, yielding a higher Na^+ concentration in the water leachates performed for a pH of 10, resulting in higher dissolution of fluoride in solution. To minimize the dissolution of fluoride in solution, a lower solid-liquid ratio of black mass would be advised, as well as less alkaline pH conditions for lower temperatures. All relevant data, including the voltage data for constructing the calibration curve, initial amount of fluoride in the black mass and fluoride concentration data are listed in Appendix D.

6.4 Direct Lithium Extraction through Ion Exchange

In section 2.2 the theory regarding adsorption through ion exchange was presented as a potential extraction technique for metal ion recovery. In section 4.2, a review over relevant literature findings regarding DLE was presented. The experimental procedure for the extraction of Li^+ through ion exchange was described in section 5.5, whereas in this section the main findings from the study will be presented.

6.4.1 Effect of Contact Time - Kinetic Studies

As introduced in section 5.5.1, kinetic studies were performed to investigate the reaction rate of the Amberlite H-form and Amberlite Na-form resins, and Molecular sieve 13X zeolite, to identify the reaction equilibrium. Figure 6.14, exhibits the Li^+ concentration depletion profile as a function of contact time, for Amberlite H-form (red), Amberlite Na-form (green) and Molecular sieve 13X (blue), for an initial Li^+ concentration of 131.4 mg/L (Appendix B.2) and fixed solid-liquid ratio of 20 g/L.
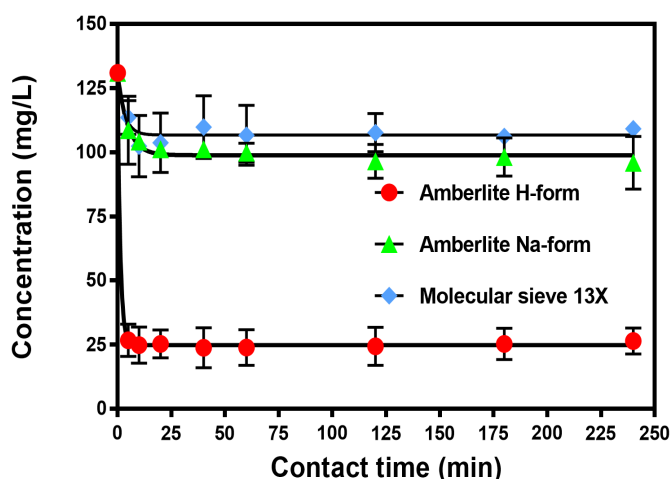
Figure 6.14: Depletion of Li^+ as a function of contact time with Amberlite H-form, Amberlite Na-form and molecular sieve 13X, for an initial Li^+ concentration of 131.4 mg/L.

From the Li^+ concentration depletion graphs, it is evident to see that equilibrium was reached after 30 minutes of contact, in all cases. Furthermore, from the graph it is also visible to see that the initial Li^+ concentration reduced significantly more for Amberlite H-form, yielding a equilibrium concentration of 24.40 ± 5.16 mg/L in the depleted solution, compared to Amberlite Na-form and Molecular sieve 13X, yielding a Li^+ depleted solution of 98.5 ± 10.25 mg/L and 103 ± 0.84 mg/L, respectively. From the study of Julien et.al, there was no significant difference in the performance of Amberlite H-form and Amberlite Na-form, when utilizing LiCl as the Li^+ source [45]. The dissimilarity observed from Figure 6.14 could be a result of the counter-ions in the water leachate, mainly Na^+, competing with Li^+ for the active sites of the resin being more substantial for Amberlite Na-form.

48

A potential reason for this could be attributed to the larger surface density of Amberlite Na-form (1.27 g/mL) in comparison to Amberlite H-form (1.19 g/mL), where a larger resin density corresponds to more available active sites for ion exchange occur, making the Na^+ occupy the active sites of the resin and hindering the uptake of Li^+ [46]. Moreover, the low Li^+ concentration depleation from Molecular sieve 13X can be attributed to the lower selectivity of Li^+ over Na^+. This was recognized from the work of Rebekka Reicha et.al, where it was confirmed that the Molecular sieve 13X sorption sites for Li^+ were occupied by Na^+, as a result of the lower hydrodynamic Na^+ size and faster diffusion towards the zeolite [67, 68].

Moreover, in Figure 6.15, the obtained Li^+ uptake capacity (a) and retention yield (b) as a function of contact time is presented. From the graphs it is evident to see that both the uptake capacity and retention yield increased with contact time, as a result of greater Li^+ depleation from the water leachate with increasing contact time. Two loading zones for Amberlite H-form (red), Amberlite Na-form (green) and Molecular sieve 13X (blue) can be appreciated, a fast one, for the first 5 minuets, and then a slow one up to 240 minutes. The first loading zone can be attributed to the stages of surface retention and diffusion within the pores of the resin, being very fast as a result of larger initial Li^+ concentration during the first minutes of contact [48]. In the second loading, the controlling mechanism could be attributed to the diffusion of Li^+ to the resins, due to the lower concentration of Li^+ in the solution after the first minutes of contact.
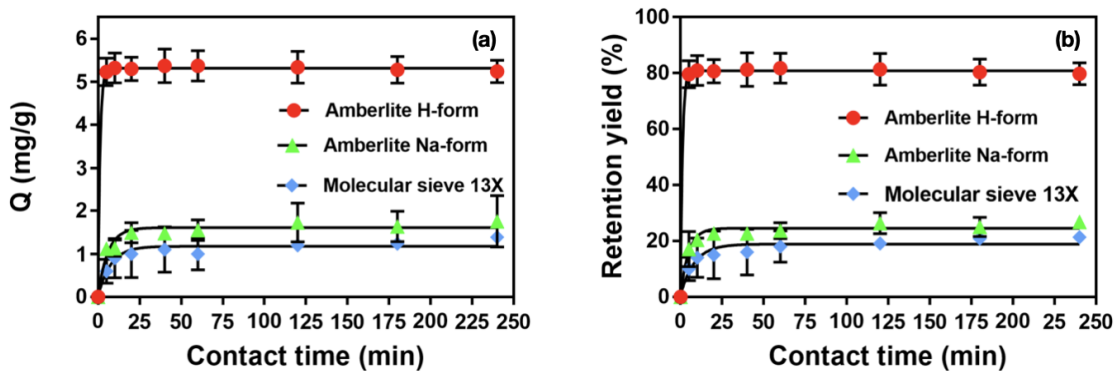
Figure 6.15: (a) Uptake capacities and (b) retention yields of Li^+ as a function of contact time from Amberlite H-form, Amberlite Na-form and Molecular sieve 13X.

After the first 5 minutes of contact, the uptake capacity reached 5.23 ± 0.32 mg/g for Amberlite H-form, 1.12 ± 0.13 mg/g for Amberlite Na-form and 0.6 ± 0.27 mg/g for Molecular sieve 13X. Furthermore, the retention yield during the first 5 minutes of contact reached 79.62 ± 4.85 % for Amberlite H-form, 17.01 ± 2.16 % for Amberlite Na-form and 8.58 ± 7.0 % for Molecular sieve 13X. For Amberlite H-form the equilibrium uptake capacity after 240 minutes reached 5.34 ± 0.26 mg/g, with an equilibrium retention yield of 81.43 ± 3.94 %, indicating that the resins became saturated fast, as there was no significant change from 5 to 240 minutes of contact. For Amberlite Na-form and Molecular sieve 13X, the equilibrium uptake capacity and retention yield after 240 minuets reached 1.76 ± 0.31 mg/g and 1.39 ± 0.02 mg/g, respectively, and 26.70 ± 1.25 % and 21.83 ± 0.32 %.

Following, kinetic studies were performed on the higher initial Li^+ concentration leachate of 602 mg/L (Appendix B.2) with Amberlite H-form. The reason for only performing the study with Amberlite H-form is attributed to the reduced Li^+ extraction performance with Amberlite Na-form and Molecular sieve 13X. The resin amount was fixed as to obtained a solid-liquid ratio of 20 g/L, as for the previous studies. Figure 6.16 exhibits the Li^+ concentration depletion as a function of contact time with Amberlite H-form. From the depletion profile, a similar drop in initial concentration can be observed for higher initial Li^+ concentration with Amberlite H-form.
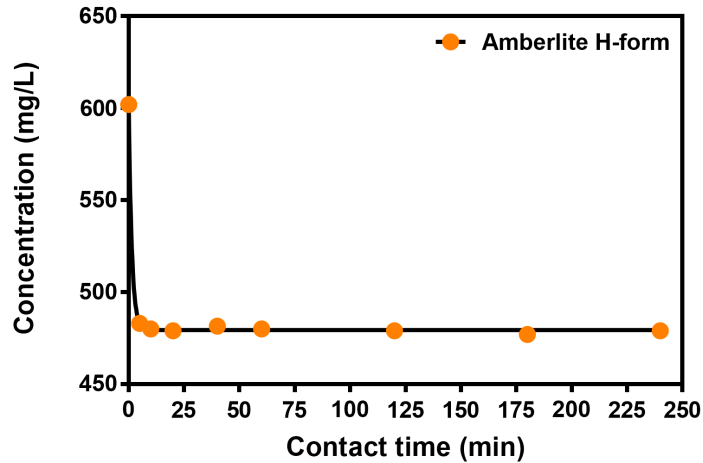
Figure 6.16: Depletion of Li^+ as a function of contact time with Amberlite H-form for an initial Li^+ concentration of 602 mg/L.

From the profile above, it is also evident to see that equilibrium was attained after 30 minutes of contact, obtaining an equilibrium concentration of 477.5 mg/L. Furthermore, the equilibrium uptake capacity and retention yield as a function of contact time was studied, yielding 6.11 mg/g and 20.42%, respectively, presented in Figure 6.17. The lower retention yield, compared to the results presented in Figure 6.15 (b), are attributed to the difference in initial Li^+ concentration, yielding lower extractions capacities for higher initial concentrations of Li^+, when a solid-liquid ratio of 20 g/L is utilized.
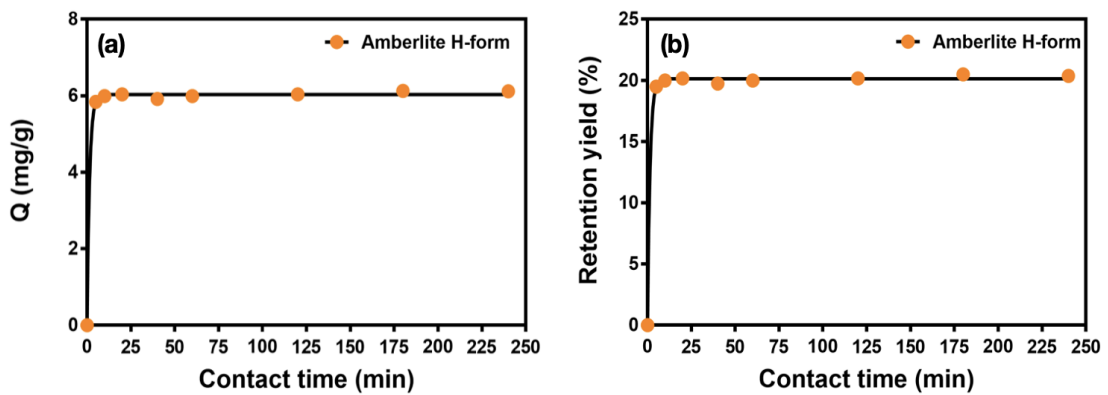
Figure 6.17: (a) Uptake capacities and (b) retention yields of Li^+ as a function of contact time from Amberlite H-form for an initial Li^+ concentration of 602 mg/L.

This study reveals that the ion exchange reaction time was rapid, attaining equilibrium within 30 minutes for all three adsorbents, implying that the reaction time can be reduced to a time frame of 30 minutes. Furthermore, the uptake capacity of Amberlite H-form showed greater selectivity towards the extraction of Li^+, compared to Amberlite Na-form and Molecular sieve 13X, as a potential result of the competing Na^+ ions in the leachate [48]. Furthermore, for higher initial concentrations of Li^+, a lower extraction was obtained for a solid-liquid ratio of 20 g/L, suggesting that a higher resin amount has to be utilized to yield a greater Li^+ extraction. The obtained results from the kinetic study are presented in Appendix C.

6.4.2   Effect of Solid-Liquid Ratio

From the previous kinetic study (section 6.4.1), it was recognized that the Amberlite Na-form resins had lower performance, in terms of uptake capacity and retention yield, compared to Amberlite H-form. It was therefore decided to perform additional experiments with HCl-washed (1M) Amberlite Na-form, to investigate if the performance could replicate the results obtained for Amberlite H-form. Furthermore, the effect of solid-liquid ratio was studied to understand the potential effect on the uptake capacity and retention yield. For these studies the solid-liquid ratio was increased in the order of 20 g/L, 40 g/L and 60 g/L, for Amberlite H-form and the HCl washed Amberlite Na-form. All other parameters including, temperature, agitation and established contact time of 30 minutes were kept constant. Figure 6.18 exhibits the effect of solid-liquid ratio on the uptake capacity and retention yield, from Amberlite H-form (red), HCl washed Amberlite Na-form (light grey) and Amberlite Na-form (green) discussed previously in the kinetic study, all for an initial Li^+ concentration leachate of 131.4 mg/L.
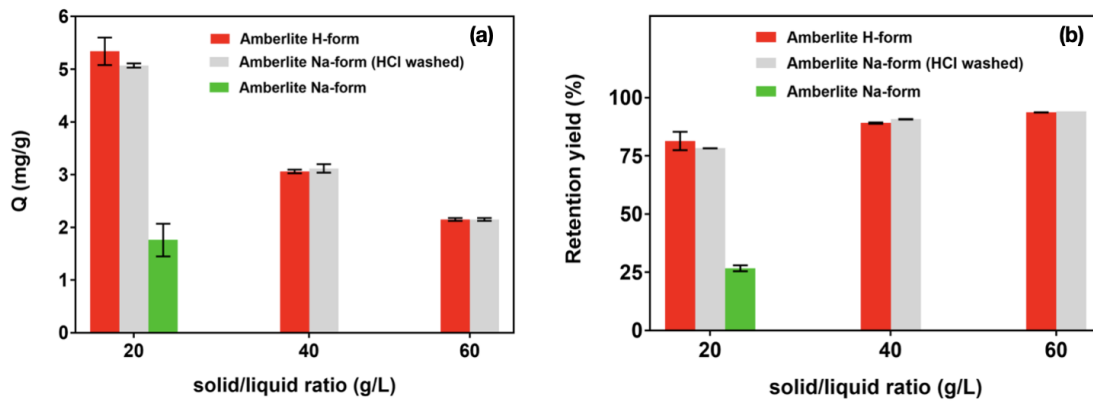
Figure 6.18: Effect of solid-liquid ratio on uptake capacity (Q) (a) and retention yield (%) (b), for an initial Li^+ concentration of 131.4 mg/L.

From the bar charts presented in Figure 6.18 (a), it is evident to see that as the solid-liquid ratio is increased, the uptake capacity of Li^+ decreases. Furthermore, the graphs revealed improvement in Li^+ retention from 81.43% to 89.12% and 93.83% when the solid-liquid ratio was increased from 20 g/L to 40 g/L and 60 g/L, respectively for Amberlite H-form.

Contrarily, the uptake capacity decreased from 5.34 mg/g to 3.06 mg/g and 2.15 mg/g for increasing resin amount from 20 g/L to 40 g/L and 60 g/L. The rapid increase in retention yield can be attributed to the increment in material surface resulting in more available active sites for the extraction of Li^+. The reduction in uptake capacity is attributed to there being more active sites available against less Li^+ to occupy the active sites, leaving more active sites unoccupied [69–71].

As can be visually seen from the bar charts in Figure 6.18 (a and b), the 1M HCl washed Amberlite Na-form yielded better performance in terms of uptake capacity, as well as retention yield, compared to the untreated resin (green). The stripped Amberlite Na-form displayed similar trends in terms of uptake capacity and retention yield as from Amberlite H-form, reaching 5.07 mg/g and 78.32%, in uptake capacity and retention yield, respectively, for a solid-liquid ratio of 20 g/L. Furthermore, the improvement in retention yield for increasing solid-liquid ratio, for the washed Amberlite Na-form, from 20 g/L to 40 g/L and 60 g/L, increased to 90.76% and 94.14%, respectively. This confirms that for higher solid-liquid ratios, higher extraction of Li^+ can be achieved. The reduction in uptake capacity as a result of increased solid-liquid ratio from 20 g/L to 40 g/L and 60 g/L, reduced to 3.12 mg/g and 2.15 mg/g, respectively, as a result of unoccupied active sites [69–71].

Moreover, the effect of solid-liquid ratio was studied for the higher initial Li^+ concentration leachate of 602 mg/L, with Amberlite H-form, where the effect of solid-liquid ratio, on the uptake capacity and retention yield is presented in Figure 6.19. The same trend in terms of reduced uptake capacity for increasing solid-liquid ratio can be acknowledged from Figure 6.19 (a). However, the reduction in uptake capacity for higher initial Li^+ concentration was not equally as rapid, as for lower initial Li^+ concentration (131.4 mg/L), yielding the highest uptake capacity of 6.11 mg/g for a solid-liquid ratio of 20 g/L, reducing accordingly to 5.86 mg/g and 5.78 mg/g, for the solid-liquid ratios of 40 g/L and 60 g/L, respectively. This implies that for higher initial concentrations of Li^+, higher uptake capacities can be achieved as a result of higher driving forces making the Li^+ diffuse into the cross-links of the resin, as a result of the higher concentration gradient [68].
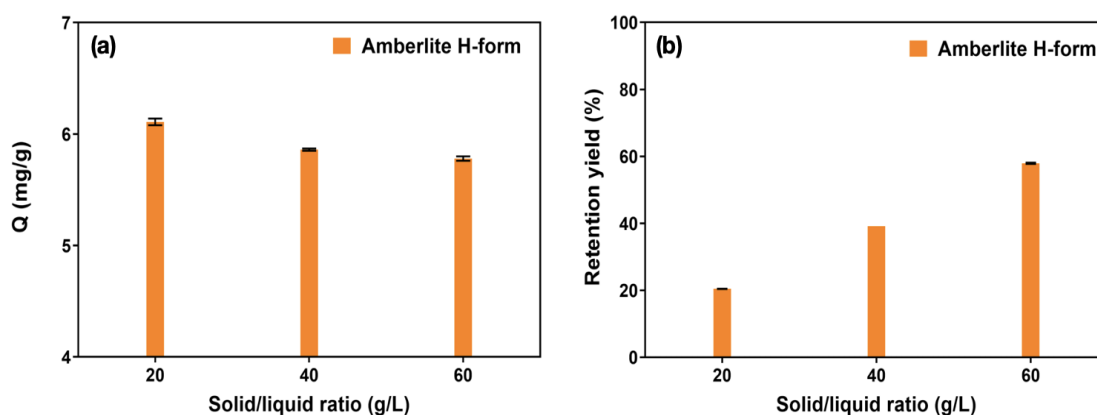
Figure 6.19: Effect of solid-liquid ratio on uptake capacity (Q) (a) and retention yield (%) (b), for an initial Li^+ concentration of 602 mg/L.

Accordingly, the rise in retention yield for increasing solid-liquid ratio, presented in Figure 6.19 (b), is attributed to the additional material surface, ensuring more active sites available for the Li^+ extraction. However, the obtained retention yields are lower, compared to the results presented in Figure 6.18 (b), reaching 20.42%, 39.16% and 57.92%, for solid-liquid ratios of 20 g/L, 40 g/L and 60 g/L, respectively. This suggests that a higher solid-liquid ratio of Amberlite H-form has to be utilized to extract all the Li^+ from the leachate for higher initial concentrations. All results discussed in this section are listed in Table 23 and 24 in Appendix C.

6.4.3   Desorption Studies

The experimental procedure for the desorption study was outlined in section 5.5.3, where 1M HCl was utilized as eluent to recover Li^+ in solution. From the previous kinetic study (section 6.4.1), it was acknowledged that the Li^+ uptake capacity and retention yield from Amberlite Na-form and Molecular sieve 13X were significantly lower than for Amberlite H-form. It was therefore decided to not perform any desorption on Amberlite Na-form and Molecular sieve 13X, and rather direct the study solely towards Amberlite H-form. Another argument is the difference in price for the utilized adsorbents, where Amberlite H-form is significantly cheaper, compared to both Amberlite Na-form and Molecular sieve 13X. Even though it was acknowledged, from section 6.4.2, that Amberlite Na-form could reach similar uptake capacities and retention yields as Amberlite H-form, when washed with HCl, the additional washing step and excess use of HCl makes it less attractive for large scale operations.
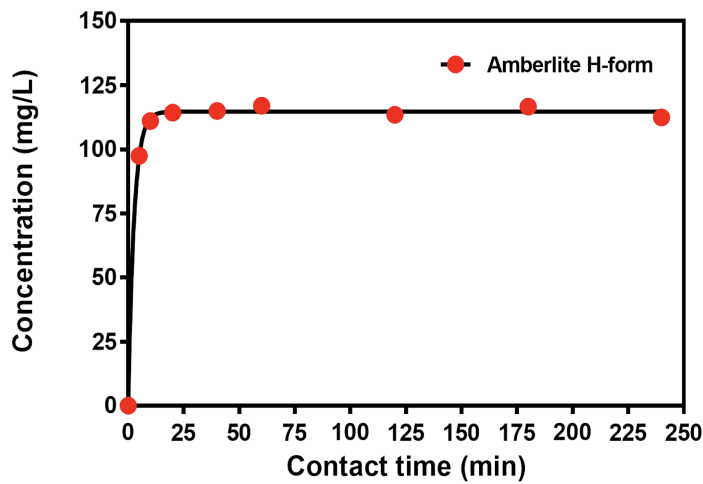
Figure 6.20: Li^+ desorption profile from Amberlite H-form for an initial Li^+ concentration of 131.4 mg/L, for a solid-liquid ratio of 20 g/L.

From the work of Julien et.al it was recognized that the desorption kinetics of Li^+ from Amberlite H-form were rapid, attaining equilibrium within 20 minutes [45]. Fast desorption kinetics of Li^+ were also confirmed in this work, with equilibrium being reached within 30 minutes of contact, seen from Figure 6.20. The Li^+ desorption profile exhibited above is

for the previously studied resins utilized in the adsorption kinetic study, for a solid-liquid ratio of 20 g/L and for an initial Li^+ concentration leachate of 131.4 mg/L.

Following, the desorption yield (%), as well as the global recovery of Li^+, from both adsorption and desorption steps was investigated. Figure 6.21 (a) presents the desorption yield, calculated from equation 10, described in section 5.5.3, as well as the global Li^+ recovery (b), from the adsorption and desorption steps, calculated from equation 11. The figure exhibits the results for Amberlite H-form, for both the lower initial Li^+ concentration leachate (red) and higher concentration leachate (orange), previously discussed in section 6.4.2. From the red bar charts presented in Figure 6.21 (a), the desorption yield was high for all studied solid-liquid ratios, reaching 99.46% for a solid-liquid ratio of 20 g/L. The desorption yield decreased slightly for increasing solid-liquid ratio, yielding 98.45% and 97.11% for solid-liquid ratios of 40 g/L and 60 g/L, respectively. From this, it can be appreciated that 1M HCl was sufficient for the elution of Li^+ from the resins, achieving > 95% desorption yield for the studied solid-liquid ratios for an initial Li^+ concentration of 131.4 mg/L.

Moreover, the desorption yield for the higher initial Li^+ concentration leachate of 602 mg/L was studied, displayed in orange in Figure 6.21 (a). A reduction in desorption yield for the higher initial concentration leachate can be acknowledged, yielding a desorption of 61.22%, 79.59% and 70.50%, for the studied solid-liquid ratios. This reduction in desorption yield can be attributed to the contact time being limited to 30 minutes, as kinetic studies were only performed on the lower initial concentration of Li^+ leachate. Moreover, as previously mentioned, the desorption yield increases for higher eluent concentration [45, 48]. This indicates that for higher initial concentration of Li^+, a higher concentration of HCl would be advised as to achieve higher Li^+ desorotion yields.
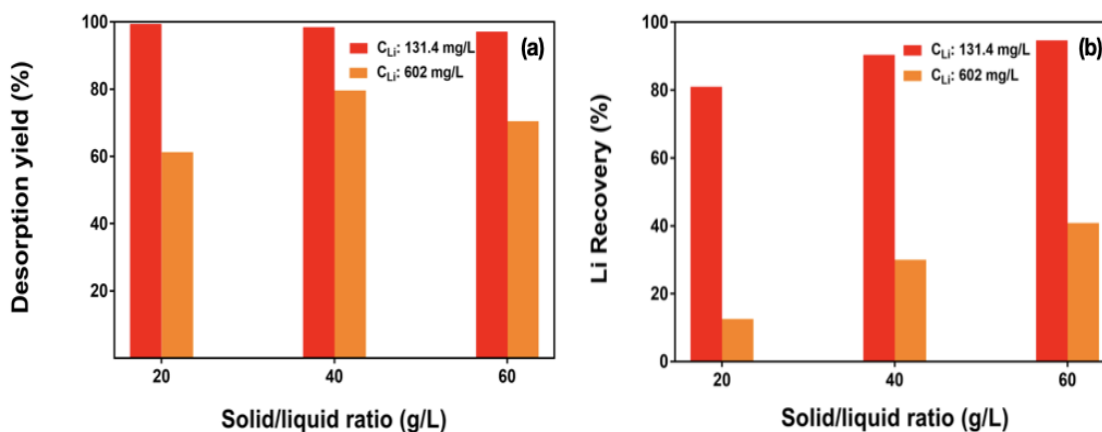
Figure 6.21: (a) Desorption yield (%) and (b) Li^+ recovery (%) for selected solid-liquid ratios for initial Li^+ concentration of 131.4 mg/L (red) and 602 mg/L (orange).

Following, the global recovery of Li^+ was studied from both adsorption and desorption steps. In Figure 6.21 (b), the recovery of Li^+ as a function of solid-liquid ratio is presented. From the recovery profile, it is evident to see that for increasing solid-liquid ratio (increment in resin amount), the recovery of Li^+ from both the adsorption and desorption

step increases. This is ascribed to the higher extraction (retention yield) of Li^+ for higher increments in material surface. For a solid-liquid ratio of 20 g/L and 40 g/L, the Li^+ recovery was 80.99% and 90.39%, respectively for the lower initial Li^+ concentration of 131.4 mg/L. The highest recovery was achieved for a solid-liquid ratio of 60 g/L, yielding 94.61% recovery with Amberlite H-form. The same observations for a solid-liquid ratio of 60 g/L can be appreciated for higher initial concentration of Li^+, yielding a recovery of 40.83%. These observations are in agreement with the results presented in section 6.4.2, where it was established that the retention yield increased for increasing solid-liquid ratio. Moreover, the reduced Li^+ recovery from the higher initial concentration leachate was significantly lower, compared to lower initial concentration of Li^+. This is again attributed to the lower Li^+ retention yield for higher initial concentrations, established in section 6.4.2, meaning that higher solid-liquid ratios of Amberlite H-form have to be utilized to recover more Li^+ from the leachate.

6.4.4   Reutilization Studies

Reutilization of the previously desorbed Amberlite H-form resins (section 6.4.3) were further studied to compare the variation in uptake capacity and retention yield, with the fresh resins, where the desorption and regeneration process was described in section 5.5.3. Figure 6.22 presents the comparison for the fresh Amberlite H-form resins (red) and the regenerated resins (light red), reused for a second time, for an initial Li^+ concentration of 131.4 mg/L. As can be seen from the bar charts in Figure 6.22 (a) the uptake capacity increased significantly for the reutilized resins, for solid-liquid ratios of 40 g/L and 60 g/L, respectively. The main reasoning behind this is the reduced solid-liquid ratio utilized for the second round of experiments, depict in Table 5, being an outcome of resin loss from the previous adsorption and desorption steps, as well as from the two filtration steps.
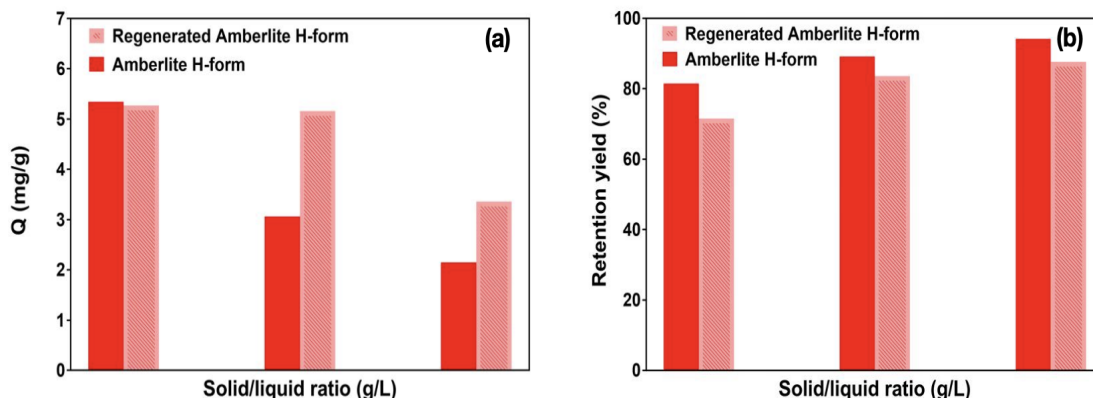
Figure 6.22: (a) Comparison in uptake capacity (Q) and (b) retention yield for fresh Amberlite H-form resins and regenerated resins, for an initial Li^+ concentration of 131.4 mg/L

However, from Figure 6.22 (b) and Table 5 the retention yield was slightly reduced for the reutilized resins, as a result of less depleation in initial Li^+ concentration from the water

leachate. The reutilized resins preformed in the order of 91.74%, 93.86% and 93.40%, for the solid-liquid ratios of 18.63 g/L, 22.30 g/L and 35.80 g/L, respectively, compared to the fresh resins. Moreover, the reutilized Amberlite H-form resins demonstrate similar Li^+ extraction capacities, as for the fresh resins, yielding high retention yields for lower initial concentrations of Li^+.

Table 5: Reutilization study with Amberlite H-form resins for an initial Li^+ concentration of 131.4 mg/L.

Resin	s/l ratio (g/L)	Q_{Li^+} (mg/g)	R_{Li^+} (%)
Fresh Amberlite H-form	20	5.34	81.43
Fresh Amberlite H-form	40	3.10	89.12
Fresh Amberlite H-form	60	2.15	93.83
Regenerated Amberlite H-form	18.63	5.27	74.71
Regenerated Amberlite H-form	22.30	5.16	83.65
Regenerated Amberlite H-form	35.80	3.36	87.64

Furthermore, reutilization of the Amberlite H-form resins for the higher initial Li^+ concentration of 602 mg/L was investigated. Figure 6.23 exhibits the comparison for the fresh resins (orange) and the reused regenerated resins (light orange). As seen from the bar charts describing the difference in uptake capacity (Figure 6.23 (a)), the same observation in terms of increased uptake capacity can be acknowledged for the regenerated resins. This increase in uptake capacity is again attributed to the reduction in solid-liquid ratio utilized for the second round of experiments (Table 6), as a result of resin loss during previous adsorption and desorption steps. The high uptake capacity of 11.64 mg/g was reached for a solid-liquid ratio of 9.02 g/L confirming the previous observation from section 6.4.2, that lower solid-liquid ratios yield higher uptake capacities.
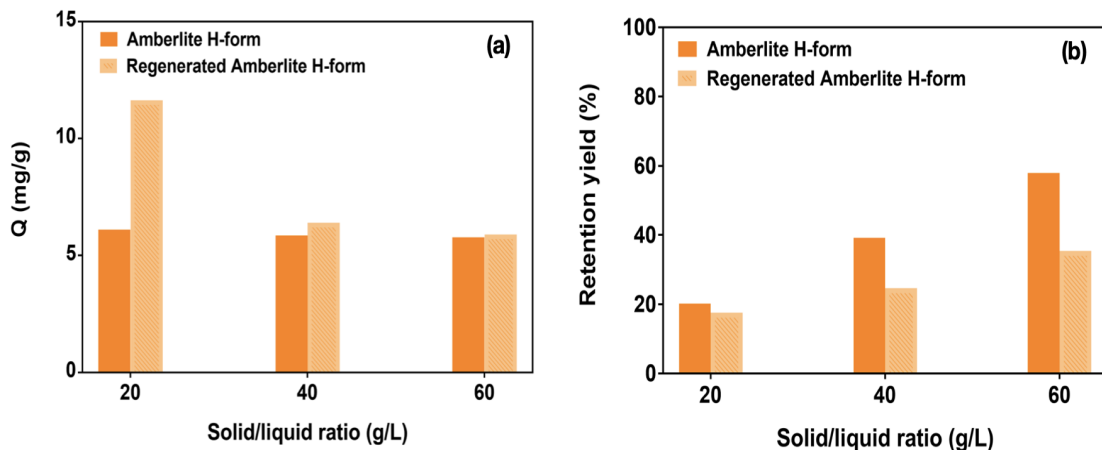
Figure 6.23: (a) Comparison in uptake capacity (Q) and (b) retention yield for fresh Amberlite H-form resins and regenerated resins, for an initial Li^+ concentration of 602 mg/L

However, as can be seen from the retention yield, in Figure 6.23 (b), a slight decrease in extraction for the reutilized resins can be identified, as a result of lower depletion in initial Li^+ concentration from the water leachate. The reutilized resins performed in the order of 85.70%, 62.77% and 59.43%, for the solid-liquid ratios of 9.02 g/L, 23.02 g/L and 36.07 g/L, respectively, compared to the fresh resins. This difference in obtained retention yields, for the reutilized resins employed for the lower initial concentration of Li^+ (light red) and the resins employed for higher initial concentration of Li^+ (light orange), can be attributed to the previously discussed lower desorption yield for the resins performed for higher initial concentration of Li^+ (section 6.4.3). The limited desorption yield gave poorer regeneration of the resins, again yielding lower retention yields compared to the fresh resins, suggesting that a larger contact time should be considered during desorption, or use a higher concentration of HCl, as to obtain a higher desorption yield and better regeneration of the Amberlite H-form resins [45, 48].

Table 6: Reutilization study with Amberlite H-form resins for an initial Li^+ concentration of 602 mg/L.

Resin	s/l ratio (g/L)	Q_{Li^+} (mg/g)	R_{Li^+} (%)
Fresh Amberlite H-form	20	6.11	20.42
Fresh Amberlite H-form	40	5.86	39.16
Fresh Amberlite H-form	60	5.78	57.92
Regenerated Amberlite H-form	9.02	11.64	17.50
Regenerated Amberlite H-form	23.02	6.40	24.58
Regenerated Amberlite H-form	36.07	5.90	34.42

6.4.5   Study on Synthetic LiCl Solution

It was decided to perform additional ion exchange experiments on synthetic solutions of LiCl, to further investigate the uptake capacity of Li^+ from Amberlite H-form. From the work presented by Julien et.al, the highest experimental Li^+ uptake capacity of 14.2 mg/g was achieved from a 0.2M LiCl solution, for a solid-liquid ratio of 20 g/L with Amberlite H-form [45]. For that reason, it was decided to perform experiments on 0.01M, 0.1M and 0.2M LiCl solutions for a fixed solid-liquid ratio of 20 g/L with Amberlite H-form, to further study the effect on Li^+ uptake capacity and retention yield for increasing initial concentration of Li^+. Figure 6.24 (a) exhibits the results representing the experimental uptake capacity for the varied initial concentrations of LiCl, whereas in Figure 6.24 (b) the obtained retention yields are presented.

As can be seen from the bar charts, presented in (a), the uptake capacity increased for larger initial concentration of Li^+. For the 0.01M LiCl solution (69.3 mg/L) the uptake capacity reached 2.76 mg/g, whereas when the initial concentration of LiCl was 0.1M (665 mg/L), the uptake capacity reached 13.21 mg/L and 17.67 mg/L for an initial LiCl concentration of 0.2M (1376 mg/L), respectively.
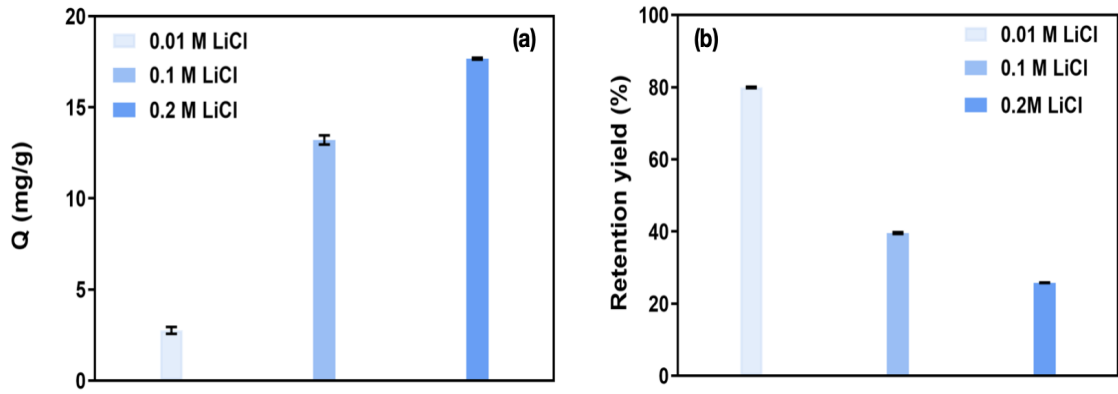
Figure 6.24: (a) Uptake capacity (Q) and (b) retention yield for increasing initial concentration of LiCl.

This observation gives rise to the taught that surface saturation was dependant on the initial Li^+ concentration, providing a significant driving force to overcome any mass transfer resistance between the Li^+ in solution and solid phase of the resin, for higher concentrations. For lower initial concentration of Li^+, the active sites of Amberlite H-form take up the Li^+ more quickly. However, for higher initial concentration of Li^+, the ions need to diffuse to the Amberlite H-form surface at a slower rate, relating to the reduction in retention yield for higher initial concentrations, seen from Figure 6.24 (b), implying that the decline in retention yield was caused by the saturation of the available active sites, becoming excessively saturated above a certain concentration [72–74].

This study demonstrates that for higher initial concentrations of Li^+, higher uptake capacities can be achieved for lower utilized resin amount, as a result of higher driving forces, caused by the concentration gradient. Furthermore, the results are in accordance with the results presented by Julien et.al. However, as was established, there is a trade-off between the uptake capacity and the retention yield for higher initial concentrations. With the desire to devise a process that can directly extract lithium in high yields, a higher retention yield would be more favourable in comparison to high Li^+ uptake by the resin, implying that a moderate resin amount has to be utilized to sustain higher uptake capacities and retention yields. The values discussed in this section are summarized in Table 7.

Table 7: Uptake capacity (Q_{Li^+}) and retention yield (R_{Li^+}) from Amberlite H-form on LiCl solutions with varied initial concentrations.

Study on LiCl solution			
Initial C_{LiCl} (mg/L)	s/l ratio (g/L)	Q_{Li^+} (mg/g)	R_{Li^+} (%)
69.3	20	2.76	79.94
665	20	13.21	39.55
1376	20	17.67	25.76

6.4.6   Investigation of Sodium Contaminants

From the previous studies it has been speculated that the uptake capacity and retention yield of Li^+ has been limited as a result of the competing Na^+ in the utilized water leachates. To further study the impact of Na^+, quantification with MP-AES was performed to determine the concentration (mg/L) of Na^+ in the utilized water leachates, as well as the depleted Li^+ solutions after resin contact and the final solutions from the desorption studies.

From the MP-AES analysis, it was acknowledged that the concentration of Na^+, in the lower concentration water leachate, was 360 mg/L, to 131.4 mg/L for Li^+, being a consequence of the pH-adjustments with NaOH from section 5.4. Moreover, for the higher initial concentration leachate, the concentration of Na^+ was 2850 mg/L to 602 mg/L for Li^+, explaining a large difference in initial concentration for the two ions. This is again a consequence of the pH-adjustments performed with NaOH, being more excessive for maintaining a desired pH of 10, for higher amounts of utilized solid black mass.

Figure 6.25 (a) presents the comparison in uptake capacity for Li^+ (light green) and Na^+ (grey) from Amberlite H-form, for the initial Li^+ concentration of 131.4 mg/L, previously discussed in section 6.4.2, and 360 mg/L for Na^+. In addition, the retention yield for both Li^+ and Na^+ is presented in Figure 6.25 (b). The presented uptake capacities for Li^+ are the previously discussed results from section 6.4.2, namely 5.34 mg/g, 3.060 mg/g and 2.15 mg/g, respectively, for the studied solid-liquid ratios of 20 g/L, 40 g/L and 60 g/L. As can be seen from (a), the uptake capacity of Na^+ was higher in all cases, compared to Li^+, yielding 5.99 mg/g, 4.93 mg/g and 4.21 mg/g, for increasing solid-liquid ratio. This confirms that the uptake capacity of Li^+ was inhibited by the uptake of Na^+.

Figure 6.25: (a) Uptake capacity (Q) and (b) retention yield of Li^+ and Na^+ as a function of solid-liquid ratio (g/L), from lower initial concentration leachate.

The major reason governing this observation is attributed to the difference in hydrodynamic radius of Li^+ and Na^+. The ionic radius of Li^+ (0.73 Å) is smaller than Na^+ (1.13 Å), however, the hydrodynamic radius of Li^+ is 3.4 Å, in comparison to 2.99 Å for Na^+, as a result of higher charge density for Li^+[67, 75].

For a higher charge density, the selective diffusion is lowered, favouring the uptake of Na^+, over Li^+ [75]. In other words, for larger hydrated ions, the more the resin bead must expand to accommodate it into the resin structure. The expansion is opposed by the restraining cross-links, explaining that larger ions require a greater force to penetrate into the resin [75]. Furthermore, the reported diffusivity of Li^+ is lower compared to Na^+, as a result of the higher hydrodynamic radius, confirming the effect from Stokes-Einstein equation (equation 18), where higher radius reduce the diffusion constant. From equation 18, K_B is the Boltzmann constant, T is the temperature, μ is the solvent viscosity and R_h is the hydrodynamic radius [67, 68, 76].

$$D = \frac{K_B T}{6\pi\mu R_h} \tag{18}$$

Furthermore, the retention yield for Na^+ was lower in comparison to Li^+, as a result of higher initial concentration of Na^+ (360 mg/L) in comparison to Li^+ (131.4 mg/L). The retention yield of Na^+ as a function of solid-liquid ratio gave 33.33%, 54.86% and 70.14% for the ratios of 20 g/L, 40 g/L and 60 g/L, respectively. Table 8 presents the obtained uptake capacities and retention yields for Na^+ for the lower concentration leachate, for the discussed solid-liquid ratios.

Table 8: Uptake capacity (Q_{Na^+}) and retention yield (R_{Na^+}) from lower initial concentration leachate with Amberlite H-form.

Uptake capacity and retention yield of Na^+			
Initial C_{Na^+} (mg/L)	s/l ratio (g/L)	Q_{Na^+} (mg/g)	R_{Na^+} (%)
360	20	5.99	33.33
360	40	4.93	54.86
360	60	4.21	70.14

Additionally, studies for the higher concentration leachate was investigated to further understand the difference in uptake capacity and retention yield for Li^+ and Na^+ from Amberlite H-form, presented in Figure 6.26 (a) and (b). From (a), a substantial difference in uptake capacity for Li^+ and Na^+ is evident, yielding 39.19 mg/g for Na^+, in contrast to 6.11 mg/g for Li^+ (section 6.4.2), for a solid-liquid ratio of 20 g/L. Major explanations governing this observation are attributed to the previously discussed difference in hydrodynamic radius, with the radius being smaller for Na^+ giving more favourable and higher uptake from Amberlite H-form. Another explanation can be attributed to the significant difference in initial concentration for the two ions, being 602 mg/L for Li^+ and 2850 mg/L for Na^+, meaning more than fourfold the amount of Li^+. This high initial concentration of Na^+ induce higher mass transfer, as a result of higher concentration gradients, resulting in a diffusion-controlled reaction. Moreover, the moderate stirring speed of 400 rpm promote higher rates of diffusion-controlled reactions by lowering the diffusion layer width, making the reaction interface move more rapidly [19]. These reasons combined, explain the selectivity and high uptake capacities of Na^+ over Li^+.
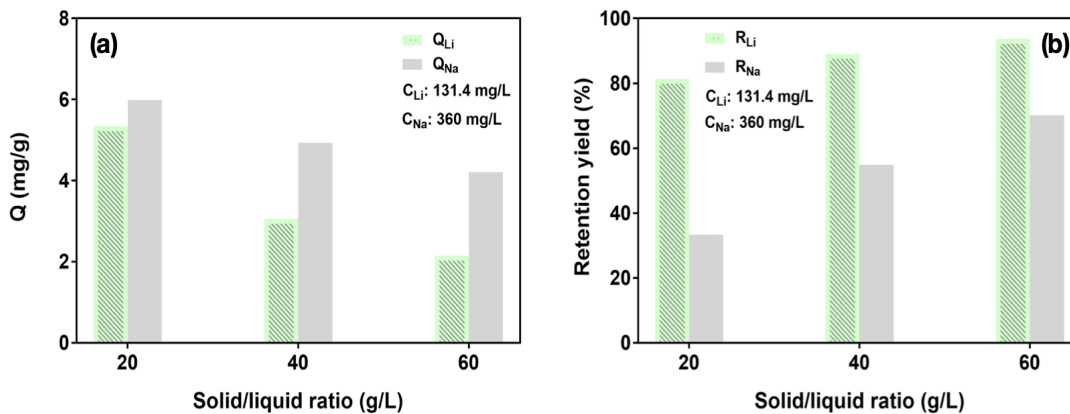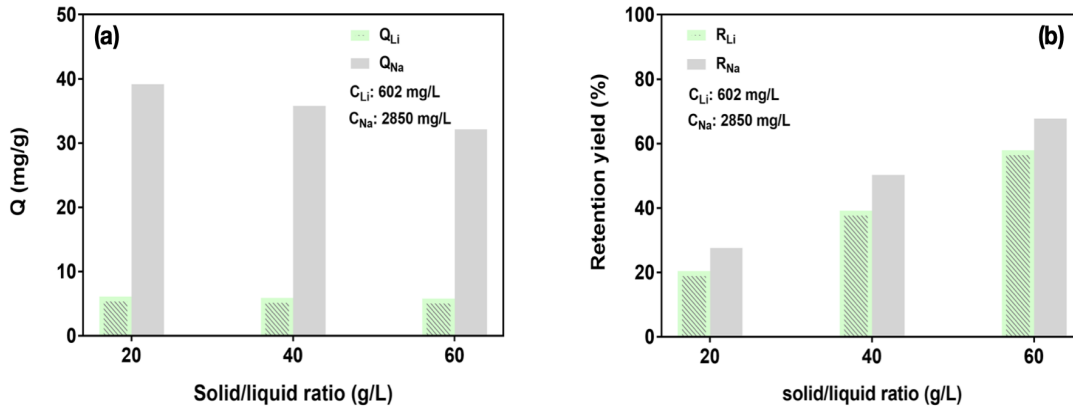
Figure 6.26: (a) Uptake capacity (Q) and (b) retention yield of Li^+ and Na^+ as a function of solid-liquid ratio (g/L), from higher initial concentration leachate.

The retention yield as a function of solid-liquid ratio (g/L) display an increasing yield for each increment in solid material, as a result of there being more available active for ion exchange, explained previously in section 6.4.2. Additionally, no significant difference in retention yield was observed for the lower initial concentration of Na^+ and the higher initial concentration, obtaining retention yields of 27.54%, 50.26% and 67.81% for increasing solid-liquid ratios, seen from Figure 6.26 (b) and Table 9. This observation is in accordance with the high obtained uptake capacity for the higher initial concentration of Na^+, as a result of high Na^+ concentration depletion.

Table 9: Uptake capacity (Q_{Na^+}) and retention yield (R_{Na^+}) from higher initial concentration leachate with Amberlite H-form.

Uptake capacity and retention yield of Na^+			
Initial C_{Na^+} (mg/L)	s/l ratio (g/L)	Q_{Na^+} (mg/g)	R_{Na^+} (%)
2850	20	39.19	27.54
2850	40	35.76	50.26
2850	60	32.17	67.81

Figure 6.27 presents the final concentrations of Na^+ and Li^+ after desorption with 1M HCl (section 6.4.3). The results in terms of Li^+ desorption yield and Li^+ recovery were discussed previously in section 6.4.3. As can be seen from the presented bar charts in Figure 6.27 (a) and (b), the presence of Na^+ in the final desorbed solution is evident, establishing that Na^+ was eluted with Li^+ in the final solution. A reason for this could be attributed to the desorption contact time as well as the retention order of Li^+ and Na^+. As previously stated, Li^+ is larger in hydrodynamic size, compared to Na^+, making Li^+ more stable in solution, preferring to stay in the mobile phase, resulting in reduced ability to penetrate into the pores of the resin. This makes the retention order of Li^+ faster than Na^+, where smaller hydrodynamic size will take longer time to eluate, because they penetrate into the resin pores [77–79].
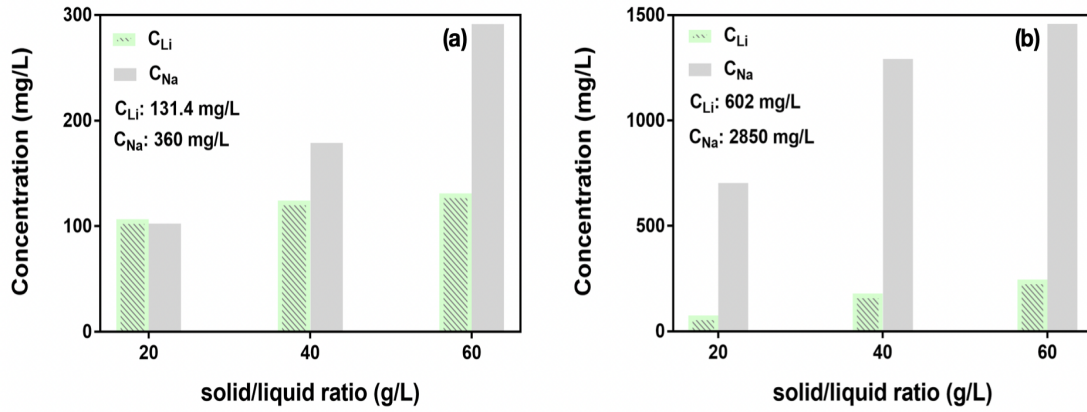
Figure 6.27: Concentration (mg/L) of Li^+ and Na^+ as a function of solid-liquid ratio (g/L).

From the previously discussed desorption studies, in section 6.4.3, the established equilibrium desorption contact time for Li^+ was 30 minutes, and set according to this time frame for all desorption experiments. This contact time may explains the large elution of Na^+ in solution, as the set contact time was sufficient to eluate both Li^+ and Na^+. This means, that by reducing the desorption contact time, a more selective elution of Li^+ can potentially be achieved for Li^+.

Moreover, the elution volume plays a significant role in the selective elution of Li^+. As described from the experimental desorption procedure, in section 5.5.3, a volume of 100 mL HCl (1M) was utilized. From literature it was recognized that higher volumes of eluent have to be utilized to eluate the ions that penetrate into the resin pores, giving rise to the taught that 100 mL was sufficient to eluate both Li^+ and Na^+ in one step when a contact time of 30 minutes was used [80, 81].

This establishment impose further questions regarding the experimental setup for the adsorption and desorption experiments. The used reactor setup (Figure 5.5) makes it challenging to perform a step-wise elution of Li^+, making it difficult to prevent the elution of Na^+ in the final solution, suggesting that an ion-exchange column should be used instead of a batch-reactor, as to obtain a more desirable separation if other ions are extracted. These findings explains the dramatic difference in obtained final concentration of Li^+ and Na^+. Furthermore, these findings suggest that an additional purification step, to selectively remove the Na^+ from the solution has to be employed, to isolate Li^+ in solution. This additional purification step increases the overall labour intensity and cost of the DLE process from black mass. In section 7.1, future recommendations will be suggested, based on the main findings from the study, for how to potentially mitigate the additional purification step of Na^+.

The obtained uptake capacities, retention yields, as well as final concentrations of Li^+ and Na^+, from the utilized water leachates are presented in Table 10 and 11, arranged according to increasing solid-liquid ratio.

Table 10: Results for lower initial concentration leachate.

Uptake capacity and retention yield for lower concentration leachate			
Initial C_{Li^+} (mg/L)	Q_{Li^+} (mg/g)	R_{Li^+} (%)	Final C_{Li^+}
131.4	5.34	81.43	106.4
131.4	3.06	89.12	124.2
131.4	2.15	93.68	131.1
Initial C_{Na^+} (mg/L)	Q_{Na^+} (mg/g)	R_{Na^+} (%)	Final C_{Na^+}
360	5.99	33.33	102.4
360	4.93	54.86	178.8
360	4.21	70.14	291.2

Table 11: Results for higher initial concentration leachate.

Uptake capacity and retention yield for higher concentration leachate			
Initial C_{Li^+} (mg/L)	Q_{Li^+} (mg/g)	R_{Li^+} (%)	Final C_{Li^+}
602	6.11	20.42	75
602	5.87	39.17	180
602	5.78	57.92	245
Initial C_{Na^+} (mg/L)	Q_{Na^+} (mg/g)	R_{Na^+} (%)	Final C_{Na^+}
2850	39.19	27.54	705
2850	35.77	50.26	1292.5
2850	32.17	67.81	1457.5

As a final study, it was decided to investigate the uptake capacity and retention yield of a mixture of 0.2M LiCl, used in previous studies (section 6.4.5), and 0.1M NaCl. This additional experiment was performed with the motive to investigate if the same observations, as for the presented results above, would be acknowledged for a mixture of LiCl and NaCl. The mixture was prepared as to obtain a ratio of 1:1 with 0.2M LiCl and 0.1M NaCl, and Amberlite H-form was used for a solid-liquid ratio of 20 g/L. Table 12 depicts the obtained results from the study, presenting the obtained uptake capacity of Li^+ (Q_{Li+}) and Na^+ (Q_{Na+}), as well as retention yield for both ions (R_{Li+} and R_{Na+}). From Table 12, it is evident to see that the uptake capacity, as well as the retention yield, was higher for Na^+, yielding an uptake capacity of 21.54 mg/g, in comparison to 10.93 mg/g for Li^+. The observations presented in Table 12 are agreeing with the results discussed from Table 10 and 11.

Table 12: Uptake capacity (mg/g) and retention yield (%) of Li^+ and Na^+ for a mixture of 0.2 M LiCl and 0.1 M NaCl.

Study on 1:1 mixture of 0.2 M LiCl and 0.1 M NaCl			
Q_{Li+} (mg/g)	Q_{Na+} (mg/g)	R_{Li+} (%)	R_{Na+} (%)
10.93	21.54	30.20	39.12

The major reasoning governing this observation is attributed to the difference in hydrodynamic radius for Li^+ and Na^+, where it has been recognized that the smaller Na^+ penetrate deeper into the resin pores, reducing the uptake of the larger Li^+. With this it can be once more concluded that the DLE process was limited by the uptake of Na^+, interfering with the selective extraction of Li^+.

6.5   Overall Mass Balance of Lithium

In Figure 4.1 the overall experimental pathway for the DLE was presented. As previously stated in the aim and scope of this work, the motivation was to directly extract Li from a water leached solution of black mass, originating from spent LIBs of electrical vehicles.

The block flow diagram presented in Figure 6.28 presents the overall distribution of Li throughout the process stages, allowing for an easier determination of the stagewise efficiency. The values representing the block flow diagram are the ones obtained from the water leaching experiment performed at 25°C, for a solid-liquid ratio of 20 g/L and pH 10 (lower initial concentration Li leachate, 131.4 mg/L). From the stages, it can be recognized that a substantial loss in the overall recovery of Li is attributed to the poor leaching efficiency from the water leaching step, yielding only 17% dissolution, making the remaining 83% of Li disappear in the filter residue (raffinate). Furthermore, from the ion exchange step with Amberlite H-form, for a solid-liquid ratio of 60 g/L, a 93.83% extraction was achieved, demonstrating that high Li extractions can be achieved for higher utilized solid-liquid ratios. Moreover, the desorption step, utilizing 1M HCl gave 94.61% recovery of Li in solution.

A high extraction of Li from the water leachate can be demonstrated yielding the highest recovery of 88.78% in this work, but the overall recovery of Li throughout the whole process illustrated below, is only 15.13%, as a result of the low Li dissolution during water leaching. Furthermore, the high contamination from the sodium ions discussed previously in section 6.4.6, demonstrate a lower purity in the final solution, needing further improvements and optimizations (section 7.1).
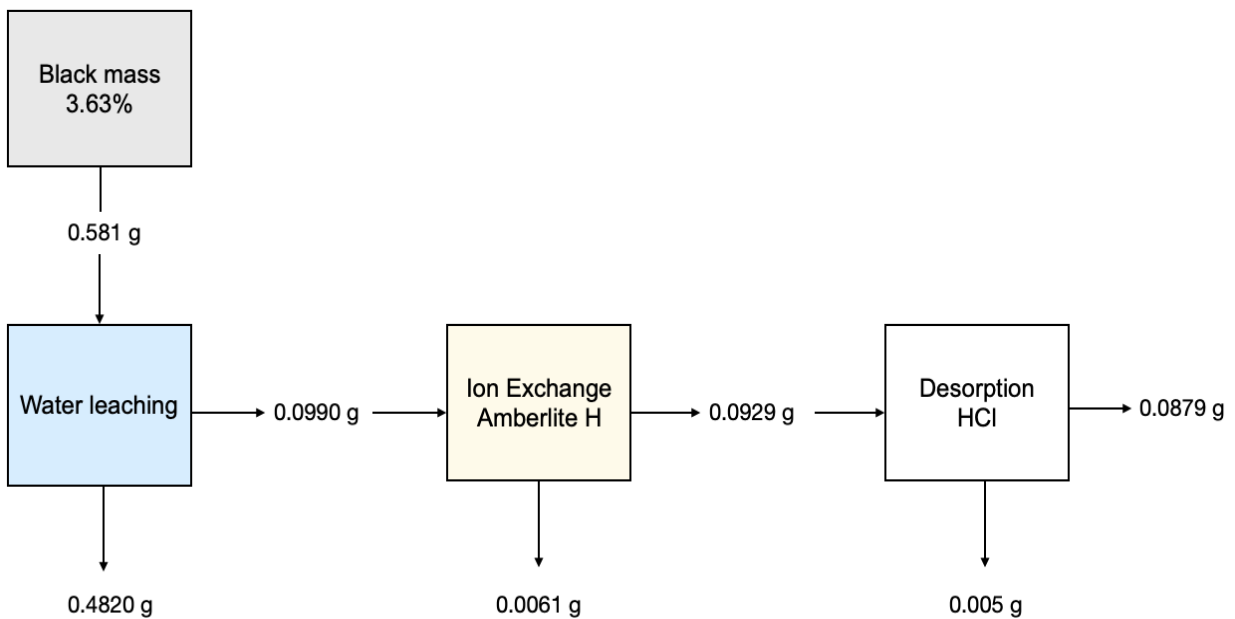
Figure 6.28: Overall mass balance of Li.

Furthermore, the overall mass balance of fluoride is presented in Figure 6.29. The values represent the conditions where the highest amount of fluoride was dissolved, namely for a solid-liquid ratio of 150 g/L (black mass to water ratio) and a pH of 10 for 80°C, previously discussed in section 6.3. From the first step, the weight percent of fluoride in the utilized black mass was calculated to be 1.39%. This calculation is presented in detail in Appendix D. Moreover, the leaching efficiency of fluoride during the water leaching step was 69.66%, for the conditions yielding the highest dissolution of fluoride in solution.

During the ion exchange step with Amberlite H-form, no fluoride is extracted as a result of the cation exchange properties of Amberlite H-form, leaving all fluoride to remain dissolved in the water leachate.
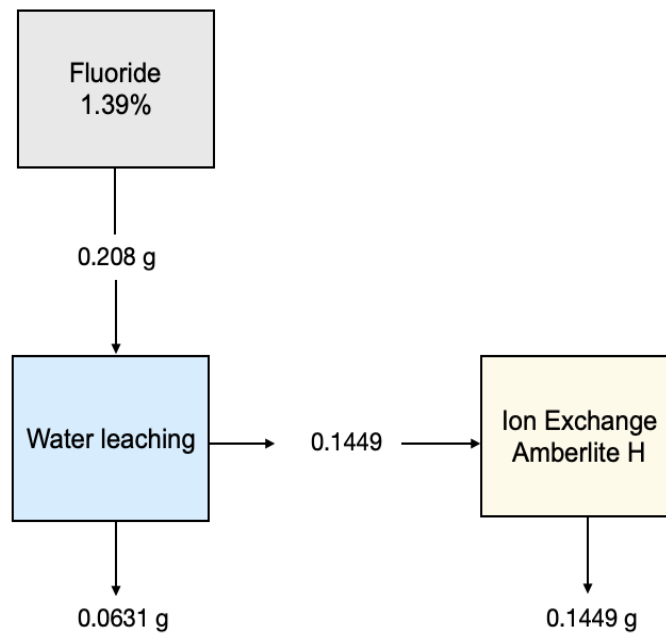
Figure 6.29: Overall mass balance of fluoride.

Chapter 7

Conclusion

In an attempt to device a process, with less process steps, cost efficiency and high recovery rate, hydrometallurgy was employed for the selective recovery of lithium. This recycling process has the ability to preserve the environment in terms of lithium raw material extraction, by creating opportunities for the reuse of critical raw materials in combination with energy savings.

In this work, an attempt has been made to develop a process for the early-stage direct lithium extraction, from a water leached solution of black mass, obtained from hydrometallurgical leaching. Water was employed as the leaching agent to diminish the usage of harsh chemicals and to selectively dissolve lithium as the majority compound in solution. Adsorption through ion exchange was further studied as a potential direct lithium extraction technique from leachate. From the water leaching study it was confirmed that the effect of temperature was negligible on the dissolution of lithium. The highest recovery was achieved for 25°C, for a solid-liquid ratio of 20 g/L, yielding 17% recovery as a result of minimal water evaporation, reducing the leaching process energy consumption. Moreover, the most selective pH condition for the recovery of lithium was confirmed to be 10. The highest dissolution (mg/L) of lithium was achieved for the highest solid-liquid ratio of 150 g/L, yielding a recovery of 7.27-9.32%, confirming a reduced leaching efficiency, in contrast to the lowest solid-liquid ratio of 20 g/L, where higher leaching efficiencies were achieved (14.69-17%).

From the direct lithium extraction study it was found that Amberlite Na-form and Molecular Sieve 13X had limited performance in terms of lithium extraction, yielding 26.70% and 21.83% extraction, respectively, as a result of competing sodium ions in the leachate. The highest lithium extraction for lower initial lithium concentration was achieved for a solid-liquid ratio of 60 g/L with Amberlite H-form, yielding 93.83% extraction. Desorption with HCl demonstrated high desorption yields of 96.61%, recovering in total 88.78% lithium from the water leachate. In contrast, for higher initial concentrations of lithium, lower extraction rates were observed as a result of higher amounts of competing sodium ions in the water leachate, yielding the highest extraction of 57.92% for a solid-liquid ratio of 60 g/L. Reutilized Amberlite H-form resins showed promising results yielding >90% extraction capacity, compared to fresh Amberlite H-form resins for one additional extraction experiment for lower initial concentration of lithium. Moreover, the highest dissolution of fluoride was achieved for high solid-liquid ratios of 150 g/L and promoted in the presence of sodium ions and alkaline pH conditions.

7.1 Future Recommendations

For the optimization of the DLE process, from a water leached solution of black mass, several recommendations should be explored, as key findings were established throughout the study. Firstly, the concentration of Li in the leachate should be increased, meaning that a higher solid-liquid ratio, of black mass power to water ratio, has to be utilized to achieve higher Li concentrations in the leachate. Furthermore, a lot of Li is lost in the filter residue, as a result of poor leaching efficiencies when employing water as a leaching agent. Therefore, the Li lost in the filter residue should be reintroduced for subsequent leaching steps, to recover more Li in solution prior to performing DLE.

Secondly, the utilized NaOH base showed complications further down the process line, in the DLE step, as a result of Na^+ blocking the active sites for the Li^+ extraction, as well as contaminating the final solution, requiring additional purification steps to remove the Na^+ contaminants. This problem can be mitigated by utilizing a different base, for example LiOH, when performing water leaching on a more acidic black mass that has not been pyrolyzed. LiOH is more expensive in comparison to NaOH, however the additional purification step required when utilizing NaOH makes the process more labour intensive.

Further optimization of the DLE step has to be performed to understand the most favourable solid-liquid ratio for extracting Li from higher initial concentration leachates. As previously established, high amounts of resin, favours higher extractions of Li^+, suggesting that the amount should be scaled with the initial Li^+ concentration in the leachate.

Lastly the elution volume of HCl has to be further optimized. If a lower volume of HCl is utilized, a more up-concentrated solution of Li can be achieved as well as reduce the elution of Na^+ in the final solution. This is beneficial, as it allows for the selective precipitation of Li^+ with for example Na_2CO_3, obtaining a Li_2CO_3 precipitate that can be further used to manufacture new LIBs and narrow the material loop. The suggested new process, based on the discussed recommendations, is presented below.
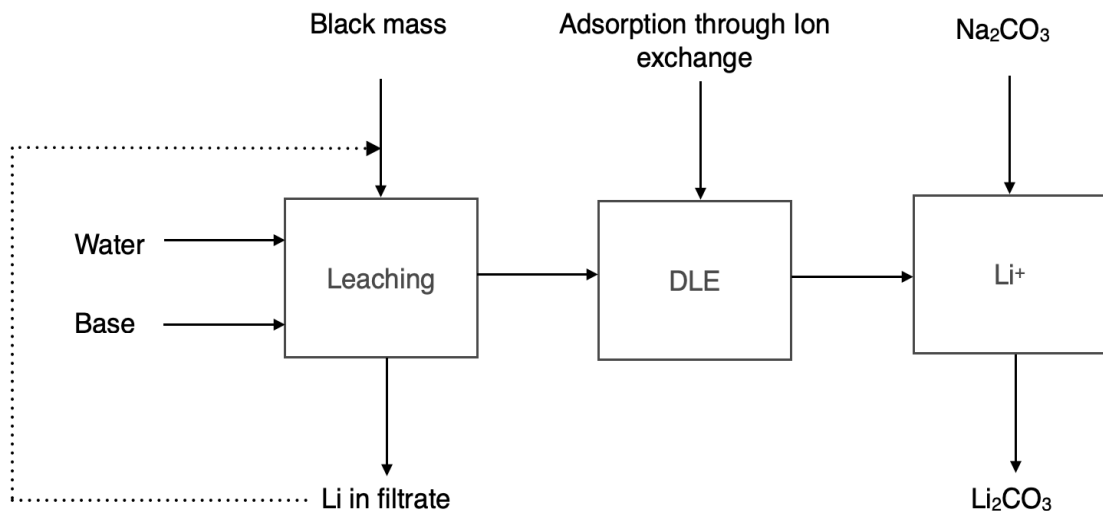
Bibliography

[1] Yuanli Ding et al. 'Automotive Li-Ion Batteries: Current Status and Future Perspectives'. In: Electrochemical Energy Reviews 2 (2019), pp. 1–28. issn: 1. doi: https://doi.org/10.1007/s41918-018-0022-z. url: https://link.springer.com/article/10.1007/s41918-018-0022-z.

[2] Tyler Or et al. 'Recycling of mixed cathode lithium-ion batteries for electric vehicles: Current status and future outlook'. In: Carbon Energy 2 (2020), pp. 6–43. issn: 1. doi: https://doi.org/10.1002/cey2.29. url: https://onlinelibrary.wiley.com/doi/10.1002/cey2.29.

[3] Victoria Flexer, Celso Fernando Baspineiro and Claudia Inés Galli. 'Lithium recovery from brines: A vital raw material for green energies with a potential environmental impact in its mining and processing'. In: Science of The Total Environment 638 (2018), pp. 1188–1204. doi: https://doi.org/10.1016/j.scitotenv.2018.05.223. url: https://www.sciencedirect.com/science/article/pii/S0048969718318746.

[4] William T. Stringfellow and Patrick F. Dobson. 'Technology for the Recovery of Lithium from Geothermal Brines'. In: Energies 14 (2021). doi: https://doi.org/10.3390/en14206805. url: https://www.mdpi.com/1996-1073/14/20/6805.

[5] Dario Latini et al. 'A comprehensive review and classification of unit operations with assessment of outputs quality in lithium-ion battery recycling'. In: Journal of Power Sources 546 (2022). doi: https://doi.org/10.1016/j.jpowsour.2022.231979. url: https://www.sciencedirect.com/science/article/pii/S0378775322009594.

[6] Yangtao Liu et al. 'Current and future lithium-ion battery manufacturing'. In: iScience 24 (2021), pp. 1–17. doi: https://doi.org/10.1016/j.isci.2021.102332. url: https://www.sciencedirect.com/science/article/pii/S258900422100300X.

[7] Jakob Fleischmann et al. 'Battery 2030: Resilient, sustainable, and circular'. In: McKinsey and Company (2023). url: https://www.mckinsey.com/industries/automotive-and-assembly/our-insights/battery-2030-resilient-sustainable-and-circular/.

[8] Sebastiaan Deuten, Jonatan J. Gómez Vilchez and Christian Thiel. 'Analysis and testing of electric car incentive scenarios in the Netherlands and Norway'. In: Technological Forecasting and Social Change 151 (2020), p. 119847. doi: https://doi.org/10.1016/j.techfore.2019.119847. url: https://www.sciencedirect.com/science/article/pii/S0040162519301210.

[9]   Yang Hua et al. 'Sustainable value chain of retired lithium-ion batteries for electric vehicles'. In: Journal of Power Sources 478 (2020), p. 228753. doi: https://doi.org/10.1016/j.jpowsour.2020.228753. url: https://www.sciencedirect.com/science/article/pii/S0378775320310570.

[10] Xue Wang et al. 'Economies of scale for future lithium-ion battery recycling infrastructure'. In: Resources, Conservation and Recycling 83 (2014), pp. 53–62. doi: https://doi.org/10.1016/j.resconrec.2013.11.009. url: https://www.sciencedirect.com/science/article/pii/S0921344913002541.

[11] Omar Velázquez-Martínez et al. 'A Critical Review of Lithium-Ion Battery Recycling Processes from a Circular Economy Perspective'. In: Batteries 5 (2019), p. 68. doi: https://doi.org/10.3390/batteries5040068. url: https://www.mdpi.com/2313-0105/5/4/68.

[12] IEA. The Role of Critical Minerals in Clean Energy Transitions. 2021. url: https://www.iea.org/reports/the-role-of-critical-minerals-in-clean-energy-transitions/executive-summary (visited on 24th Jan. 2023).

[13] Tobias Wesselborg, Sami Virolainen and Tuomo Sainio. 'Recovery of lithium from leach solutions of battery waste using direct solvent extraction with TBP and FeCl3'. In: Hydrometallurgy 202 (2021). doi: https://doi.org/10.1016/j.hydromet.2021.105593. url: https://www.sciencedirect.com/science/article/pii/S0304386X21000426.

[14] Youping Miao et al. 'An overview of global power lithium-ion batteries and associated critical metal recycling'. In: Journal of Hazardous Materials 425 (2022). doi: https://doi.org/10.1016/j.jhazmat.2021.127900. url: https://www.sciencedirect.com/science/article/pii/S0304389421028697.

[15] World Economic Forum. A Vision for a Sustainable Battery Value Chain in 2030 Unlocking the Full Potential to Power Sustainable Development and Climate Change Mitigation. url: https://www3.weforum.org/docs/WEF_A_Vision_for_a_Sustainable_Battery_Value_Chain_in_2030_Report.pdf (visited on 24th Jan. 2023).

[16] Qiang Wei et al. 'Spent lithium ion battery (LIB) recycle from electric vehicles: A mini-review'. In: Science of The Total Environment 866 (2023). doi: https://doi.org/10.1016/j.scitotenv.2022.161380. url: https://www.sciencedirect.com/science/article/pii/S0048969722084844.

[17] Linda Gaines et al. 'Direct recycling R&D at the ReCell Center'. In: Recycling 6 (2021). doi: https://doi.org/10.3390/recycling6020031. url: https://www.mdpi.com/2313-4321/6/2/31.

[18]   Xiaotu Ma, Luqman Azhari and Yan Wang. 'Li-ion battery recycling challenges'. In: Chem 7 (2021), pp. 2843–2847. doi: https://doi.org/10.1016/j.chempr.2021.09.013. url: https://www.sciencedirect.com/science/article/pii/S2451929421004757.

[19]   Michael L. Free. Hydrometallurgy Fundamentals and Applications. 2016.

[20]   Li-Feng Zhou et al. 'The Current Process for the Recycling of Spent Lithium Ion Batteries'. In: Frontiers in Chemistry 8 (2020). doi: https://doi.org/10.3389/fchem.2020.578044. url: https://www.frontiersin.org/articles/10.3389/fchem.2020.578044/full.

[21]   Ankit Verma et al. 'Metal recovery using Oxalate Chemistry: A technical review'. In: Industrial & Engineering Chemistry Research 58 (2019). doi: https://doi.org/10.1021/acs.iecr.9b02598. url: https://pubs.acs.org/doi/full/10.1021/acs.iecr.9b02598.

[22]   Muammer Kaya. 'State-of-the-art lithium-ion battery recycling technologies'. In: Circular Economy 1 (2022). doi: https://doi.org/10.1016/j.cec.2022.100015. url: https://www.sciencedirect.com/science/article/pii/S2773167722000152.

[23]   Léa M.J. Rouquette et al. 'Intensification of lithium carbonation in the thermal treatment of spent EV Li-ion batteries via waste utilization and selective recovery by water leaching'. In: Resources, Conservation & Recycling Advances 17 (2024). doi: https://doi.org/10.1016/j.rcradv.2022.200125. url: https://www.sciencedirect.com/science/article/pii/S2667378922000621.

[24]   Vassilis J. Inglezakis and Stavros G. Poulopoulos. 'Adsorption, Ion Exchange and Catalysis'. In: Elsevier (2006). doi: https://doi.org/10.1016/B978-044452783-7/50002-1. url: https://www.sciencedirect.com/science/article/pii/B9780044527837500021.

[25]   James R. Couper et al. '15 - Adsorption and Ion Exchange'. In: Chemical Process Equipment (Third Edition) (2012), pp. 529–559. doi: https://doi.org/10.1016/B978-0-12-396959-0.00015-X. url: https://www.sciencedirect.com/science/article/pii/B978012396959000015X.

[26]   François de Dardel. Ion exchange reactions. url: http://dardel.info/IX/reactions.html (visited on 4th June 2023).

[27]   DuPont. Ion Exchange Resins Selectivity. url: https://www.dupont.com/content/dam/dupont/amer/us/en/water-solutions/public/documents/en/IER-Selectivity-TechFact-45-D01458-en.pdf (visited on 4th June 2023).

[28]   Labster Theory. Ion exchange chromatography. 2021. url: https://theory.labster.com/iexchromatography/ (visited on 12th Feb. 2023).

[29] Andrei A. Bunaciu, Elena gabriela Udriştioiu and Hassan Y. Aboul-Enein. 'X-ray diffraction: Instrumentation and applications'. In: Critical Reviews in Analytical Chemistry 45 (2015). doi: https://doi.org/10.1080/10408347.2014.949616. url: https://www.tandfonline.com/doi/full/10.1080/10408347.2014.949616.

[30] veqter. X-RAY DIFFRACTION. url: https://www.veqter.co.uk/residual-stress-measurement/x-ray-diffraction (visited on 25th May 2023).

[31] Kalsoom Akhtar et al. 'Scanning electron microscopy: Principle and applications in nanomaterials characterization'. In: Handbook of Materials Characterization (2018). doi: https://doi.org/10.1007/978-3-319-92955-2_4. url: https://link.springer.com/chapter/10.1007/978-3-319-92955-2_4.

[32] Department of Materials Science and University of Cambridge Metallurgy. Looking at materials up close - The Scanning Electron Microscope (SEM). url: https://www.rrutc.msm.cam.ac.uk/outreach/articles/the-scanning-electron-microscope (visited on 25th May 2023).

[33] Agilent. Microwave Plasma Atomic Emission Spectroscopy (MP-AES) Application eHandbook. 2021. url: https://www.agilent.com/cs/library/applications/5991-7282EN_MP-AES-eBook.pdf.

[34] Engineers Community. Fourier Transform Infrared Spectroscopy (FTIR) Principle. url: https://engineerscommunity.com/t/fourier-transform-infrared-spectroscopy-ftir-principle/4980 (visited on 30th May 2023).

[35] Manoj Rajankunte Mahadeshwara. Fourier Transform Infrared Spectroscopy. url: https://www.tribonet.org/wiki/fourier-transform-infrared-spectroscopy/ (visited on 30th May 2023).

[36] Usman Saleem. 'Recycling Lithium from Spent Electric Vehicle (EV) Li-ion Batteries (LIBs) – A Unified Process'. In: Master's thesis, Chemical Engineering, NTNU, 2022. (2022).

[37] Yasin Orooji et al. 'Recent advances in nanomaterial development for lithium ion-sieving technologies'. In: Desalination 529 (2022). doi: https://doi.org/10.1016/j.desal.2022.115624. url: https://www.sciencedirect.com/science/article/pii/S0011916422000790.

[38] Hanwei Yu et al. 'Metal-based adsorbents for lithium recovery from aqueous resources'. In: Desalination 539 (2022). doi: https://doi.org/10.1016/j.desal.2022.115951. url: https://www.sciencedirect.com/science/article/pii/S0011916422004064.

[39] María L. Vera et al. 'Environmental impact of direct lithium extraction from Brines'. In: Nature Reviews Earth & Environment 4 (2023). doi: https://doi.org/10.1038/s43017-022-00387-5. url: https://www.nature.com/articles/s43017-022-00387-5.

[40] Jing Zhong, Sen Lin and Jianguo Yu. 'Li$^+$ adsorption performance and mechanism using lithium/aluminum layered double hydroxides in low grade brines'. In: Desalination (2021). doi: https://doi.org/10.1016/j.desal.2021.114983. url: https://www.sciencedirect.com/science/article/pii/S0011916421000540.

[41] Hui XU, Chang-Guo Chen and Ying-Hua Song. 'Synthesis and properties of lithium ion-sieve precursor Li4Mn5O12'. In: Journal of Inorganic Materials 28 (2013). doi: 10.3724/sp.j.1077.2013.12513. url: https://www.scopus.com/record/display.uri?eid=2-s2.0-84881002515&origin=inward.

[42] Shulei Wang et al. 'Hydrothermal synthesis of lithium-enriched b- Li2TiO3 with an ion-sieve application: excellent lithium adsorption'. In: RSC Advances 6 (2016). doi: https://doi.org/10.1039/C6RA18018C. url: https://pubs.rsc.org/en/content/articlelanding/2016/RA/C6RA18018C.

[43] Ali Shoghi et al. 'Spinel H4Ti5O12 nanotubes for Li recovery from aqueous solutions: Thermodynamics and kinetics study'. In: Journal of Environmental Chemical Engineering 9 (2021). doi: https://doi.org/10.1016/j.jece.2020.104679. url: https://www.sciencedirect.com/science/article/pii/S2213343720310289.

[44] Jia-Li Xiao et al. 'Synthesis and Adsorption Properties of Li1.6Mn1.6O4 Spinel'. In: Industrial & Engineering Chemistry Research 52 (2013). doi: https://doi.org/10.1021/ie400691d. url: https://pubs.acs.org/doi/10.1021/ie400691d.

[45] Julien Lemaire et al. 'Lithium recovery from aqueous solution by sorption/desorption'. In: Hydrometallurgy 143 (2014), pp. 1–11. doi: https://doi.org/10.1016/j.hydromet.2013.11.006. url: https://www.sciencedirect.com/science/article/pii/S0304386X13002247.

[46] Dupont Water Solutions. DuPont™ AmberLite™ IRC120 H. url: https://www.dupont.com/products/amberliteirc120h.html.

[47] Rebekka Reich et al. 'Lithium extraction techniques and the application potential of different sorbents for lithium recovery from brines'. In: Mineral Processing and Extractive Metallurgy Review (2022). doi: https://doi.org/10.1080/08827508.2022.2047041. url: https://www.tandfonline.com/doi/full/10.1080/08827508.2022.2047041.

[48] Fátima Arroyo et al. 'Lithium recovery from desalination brines using specific ion-exchange resins'. In: Desalination 468 (2019). doi: https://doi.org/10.1016/j.desal.2019.114073. url: https://www.sciencedirect.com/science/article/pii/S0011916419305168.

[49] Metrohm. Ion-selective electrodes (ISE) Manual. url: https://www.metrohm.com/nb_no/products/8/1098/81098042.html.

[50] Safoura Babanejad et al. 'High-Temperature Behavior of Spent Li-Ion Battery Black Mass in Inert Atmosphere'. In: Journal of Sustainable Metallurgy 8 (2022). doi: https://doi.org/10.1007/s40831-022-00514-y. url: https://link.springer.com/article/10.1007/s40831-022-00514-y.

[51] Alexander Quinn et al. 'Electron Backscatter Diffraction for Investigating Lithium-Ion Electrode Particle Architectures'. In: Electrode Particle Architectures 1 (2020). doi: https://doi.org/10.1016/j.xcrp.2020.100137. url: https://www.sciencedirect.com/science/article/pii/S2666386420301417.

[52] Zhiming Yan, Anwar Sattar and Zushu Li. 'Priority Lithium recovery from spent Li-ion batteries via carbothermal reduction with water leaching'. In: Resources, Conservation and Recycling 192 (2023). doi: https://doi.org/10.1016/j.resconrec.2023.106937. url: https://www.sciencedirect.com/science/article/pii/S0921344923000745.

[53] Shunsuke Kuzuhara et al. 'Recovering Lithium from the Cathode Active Material in Lithium-Ion Batteries via Thermal Decomposition'. In: Metals 10 (2020). doi: https://doi.org/10.3390/met10040433. url: https://www.mdpi.com/2075-4701/10/4/433.

[54] Tiaan Punt et al. 'The Efficiency of Black Mass Preparation by Discharge and Alkaline Leaching for LIB Recycling'. In: Minerals 12 (2022). doi: https://doi.org/10.3390/min12060753. url: https://www.mdpi.com/2075-163X/12/6/753.

[55] Daniel Alvarenga Ferreira et al. 'Hydrometallurgical separation of aluminium, cobalt, copper and lithium from spent Li-ion batteries'. In: Journal of Power Sources 187 (2009). doi: https://doi.org/10.1016/j.jpowsour.2008.10.077. url: https://www.sciencedirect.com/science/article/pii/S0378775308019964.

[56] Fredrik Larsson et al. 'Toxic fluoride gas emissions from lithium-ion battery fires'. In: Scientific Reports volume 7 (2017). doi: https://doi.org/10.1038/s41598-017-09784-z. url: https://www.nature.com/articles/s41598-017-09784-z.

[57] Tiaan Punt et al. 'The Efficiency of Black Mass Preparation by Discharge and Alkaline Leaching for LIB Recycling'. In: Minerals 12 (2022). doi: https://doi.org/10.3390/min12060753. url: https://www.mdpi.com/2075-163X/12/6/753.

[58] Laurance Donnelly et al. 'The sampling and phase characterisation of Black Mass'. In: TOS Forum (2022). doi: 10.1255/tosf.166. url: https://www.impopen.com/subs/tosf/v22/S11_0397.pdf.

[59]   Safoura Babanejad et al. 'High-Temperature Behavior of Spent Li-Ion Battery Black Mass in Inert Atmosphere'. In: Journal of Sustainable Metallurgy 8 (2022). doi: 10.1007/s40831-022-00514-y. url: https://link.springer.com/article/10.1007/s40831-022-00514-y.

[60]   Hanlin Huang, Chunwei Liu and Zhi Sun. 'Transformation and migration mechanism of fluorine-containing pollutants in the pyrolysis process of spent lithium-ion battery'. In: Journal of Hazardous Materials 435 (2022). doi: https://doi.org/10.1016/j.jhazmat.2022.128974. url: https://www.sciencedirect.com/science/article/pii/S0304389422007634.

[61]   Mohamadi Somayeh. Preparation and Characterization of PVDF/PMMA/Graphene Polymer Blend Nanocomposites by Using ATR-FTIR Technique. 2012. doi: 10.5772/36497. url: https://www.researchgate.net/publication/224830990.

[62]   K. Medeiros et al. 'Evaluation of the electromechanical behavior of polyvinylidene fluoride used as a component of risers in the offshore oil industry'. In: Oil & Gas Science and Technology 73 (2018), p. 48. doi: https://doi.org/10.2516/ogst/2018058. url: https://www.researchgate.net/publication/328584586.

[63]   Ryan T. Pekarek et al. 'Intrinsic chemical reactivity of solid-electrolyte interphase components in silicon–lithium alloy anode batteries probed by FTIR spectroscopy'. In: Journal of Materials Chemistry A 8 (2021). doi: https://doi.org/10.1039/C9TA13535A. url: https://pubs.rsc.org/en/content/articlelanding/2020/TA/C9TA13535A.

[64]   Tobiloba Onipe, Joshua N. N. and John O. Odiyo. 'Geochemical characterization and assessment of fluoride sources in groundwater of Siloam area, Limpopo Province, South Africa'. In: Scientific Reports 11 (2021). doi: https://doi.org/10.1038/s41598-021-93385-4. url: https://www.nature.com/articles/s41598-021-93385-4.

[65]   Narsimha Adimalla, Sudarshan Venkatayogi and S. V. G. Das. 'Assessment of fluoride contamination and distribution: a case study from a rural part of Andhra Pradesh, India'. In: Applied Water Science 9 (2019). doi: https://doi.org/10.1007/s13201-019-0968-y. url: https://link.springer.com/article/10.1007/s13201-019-0968-y.

[66]   Chander Kumar Singh et al. 'Geochemical modeling of high fluoride concentration in groundwater of Pokhran area of Rajasthan, India'. In: Bulletin of Environmental Contamination and Toxicology 86 (2011). doi: https://doi.org/10.1007/s00128-011-0192-4. url: https://link.springer.com/article/10.1007/s00128-011-0192-4.

[67] Rebekka Reicha et al. 'Structural and compositional variation of zeolite 13X in lithium sorption experiments using synthetic solutions and geothermal brine'. In: Microporous and Mesoporous Materials 359 (2023). doi: https://doi.org/10.1016/j.micromeso.2023.112623. url: https://www.sciencedirect.com/science/article/pii/S1387181123001944.

[68] Wendong Shi et al. 'Size and shape effects on diffusion and absorption of colloidal particles near a partially absorbing sphere: Implications for uptake of nanoparticles in animal cells'. In: Physical Review E 78 (2008). doi: https://doi.org/10.1103/PhysRevE.78.061914. url: https://journals.aps.org/pre/abstract/10.1103/PhysRevE.78.061914.

[69] Norbert Onen Rubangakene et al. 'Novel nano-biosorbent materials from thermal catalytic degradation of green pea waste for cationic and anionic dye decolorization'. In: Biomass Conversion and Biorefinery (2022). doi: https://doi.org/10.1007/s13399-022-03299-y. url: https://link.springer.com/article/10.1007/s13399-022-03299-y.

[70] Bahdja Hayoun et al. 'Production of modified sunflowers seed shells for the removal of bisphenol A'. In: RSC Advances 11 (2021). doi: 10.1039/d0ra09137e. url: https://pubs.rsc.org/en/content/articlelanding/2021/RA/D0RA09137E.

[71] M.K. Rai et al. 'Removal of hexavalent chromium Cr (VI) using activated carbon prepared from mango kernel activated with H3PO4'. In: Resource-Efficient Technologies 2 (2016). doi: https://doi.org/10.1016/j.reffit.2016.11.011. url: https://www.sciencedirect.com/science/article/pii/S2405653716300707.

[72] Jegan Josephraj et al. 'Sorption kinetics and isotherm studies of cationic dyes using groundnut (Arachis hypogaea) shell derived biochar a low-cost adsorbent'. In: Applied Ecology and Environmental Research 18 (2020). doi: http://dx.doi.org/10.15666/aeer/1801_19251939. url: https://www.researchgate.net/publication/341981386_Sorption_kinetics_and_isotherm_studies_of_cationic_dyes_using_groundnut_Arachis_hypogaea_shell_derived_biochar_a_low-cost_adsorbent.

[73] Ashraf M., Maah Mohd and Yusoff Ismail. 'Study of mango biomass (Mangifera indica L) as a cationic biosorbent'. In: International Journal of Environmental Science and Technology 7 (2010). doi: 10.1007/BF03326167. url: https://link.springer.com/article/10.1007/BF03326167.

[74] Sana Alahmadi, Sharifah Mohamad and Mohd Maah. 'Comparative Study of Tributyltin Adsorption onto Mesoporous Silica Functionalized with Calix[4]arene, p-tert-Butylcalix[4]arene and p-Sulfonatocalix[4]arene'. In: Molecules 19 (2014). doi: https://doi.org/10.3390/molecules19044524. url: https://www.mdpi.com/1420-3049/19/4/4524.

[75] Samuel Warnock et al. 'Engineering Li/Na selectivity in 12-crown-4–functionalized polymer membranes'. In: Proceedings of the National Academy of Sciences 118 (2021). doi: https://doi.org/10.1073/pnas.2022197118. url: https://www.pnas.org/doi/full/10.1073/pnas.2022197118.

[76] Kikuko Hayamizu, Yusuke Chiba and Tomoyuki Haishi. 'Dynamic ionic radius of alkali metal ions in aqueous solution: A pulsed-field gradient NMR study'. In: RSC Advances 11 (2021). doi: https://doi.org/10.1039/D1RA02301B. url: https://pubs.rsc.org/en/content/articlelanding/2021/ra/d1ra02301b.

[77] Thomas Wenzel. Ion-Exchange Chromatography. url: https://chem.libretexts.org/Bookshelves/Analytical_Chemistry/Supplemental_Modules_(Analytical_Chemistry)/Analytical_Sciences_Digital_Library / Courseware / Separation_Science / 02_Text / 05_Liquid_Chromatographic_Separation_Methods/02_Ion-Exchange_Chromatography (visited on 4th June 2023).

[78] J. H. Aubert and M. Tirrell. 'Flow rate dependence of elution volumes in size Exclusion Chromatography: A Review'. In: Journal of Liquid Chromatography 6 (1983). doi: https://doi.org/10.1080/01483918308062875. url: https://www.tandfonline.com/doi/abs/10.1080/01483918308062875.

[79] Pran Kishore Deb et al. 'Pharmaceutical and biomedical applications of polymers'. In: Basic Fundamentals of Drug Delivery (2019). doi: https://doi.org/10.1016/B978-0-12-817909-3.00006-6. url: https://www.sciencedirect.com/science/article/pii/B9780128179093000066.

[80] K. Van Hoecke et al. 'Single-step chromatographic isolation of lithium from whole-rock carbonate and clay for isotopic analysis with multi-collector ICP-mass spectrometry'. In: Journal of Analytical Atomic Spectrometry 30 (2015). doi: https://doi.org/10.1039/C5JA00165J. url: https://pubs.rsc.org/en/content/articlelanding/2015/JA/C5JA00165J.

[81] Krisna C. Duong-Ly and Sandra B. Gabelli. 'Chapter Nine - Gel Filtration Chromatography (Size Exclusion Chromatography) of Proteins'. In: Methods in Enzymology 541 (2014). doi: https://doi.org/10.1016/B978-0-12-420119-4.00009-4. url: https://www.sciencedirect.com/science/article/pii/B9780124201194000094.

Appendix

A   Black mass digestion results

Table 13 and 14 describe the obtained wt% for the microwave digestion and manual digestion of black mass. The results are averages obtained from three samples with ~ 0.5 g black mass power, for both digestion methods.

Table 13: Concentration, mass and wt% of metals from speedwave digestion of black mass.

Obtained results from Speedwave digestion of black mass				
Metal	AVG Conc. (mg/L)	Mass (mg)	wt.%	STD
Fe	350	0.35	0.115	0.037
Cu	3350	3.35	1.457	0.268
Ni	30400	30.4	10.515	0.768
Co	26750	26.75	9.965	1.004
Li	9350	9.35	3.70	0.494
Mn	22050	22.05	7.821	0.424
Al	1000	1	0.354	0.220

Table 14: Concentration, mass and wt% of metals from manual digestion of black mass.

Obtained results from Manual digestion of black mass				
Metal	AVG Conc. (mg/L)	Mass (g)	wt.%	STD
Fe	1310	1.31	0.254	0.009
Cu	7200	7.2	1.522	0.123
Ni	47750	47.75	9.391	0.183
Co	46500	46.50	9.102	0.239
Li	17255	17.26	3.631	0.269
Mn	34900	34.90	6.904	0.077
Al	695	0.70	0.142	0.0

B Water Leaching

B.1 Water Leaching Experiments and Conditions

Table 15 presents a summary over the performed water leaching experiments with the main conditions including temperature (°C), pH and solid-liquid ratio (g/L), discussed in section 5.4.

Table 15: Summary of Leaching Experiments from section 5.4.

Exp.	Temp. (°C)	pH	s/l ratio (g/L)
Leaching Experiments Summary			
1	80	6.5	20
2	80	6.5	40
3	80	6.5	150
4	80	8	20
5	80	8	40
6	80	8	150
7	80	10	20
8	80	10	40
9	80	10	150
10	60	6.5	20
11	60	6.5	40
12	60	6.5	150
13	60	8	20
14	60	8	40
15	60	8	150
16	60	10	20
17	60	10	40
18	60	10	150
19	25	10	20
20	25	10	150

B.2 Concentrations of metals in solution from MP-AES

The concentration of metals in the water leached solutions, analysed with MP-AES are presented in Table 16, for all the performed leaching experiments discussed in section 5.4.

Table 16: Concentration of metals from all water leaching experiments.

Concentration of metals (mg/L)							
Exp.	Li	Al	Ni	Co	Mn	Cu	Fe
1	134.1	0.9	15.3	17.2	92.2	20.5	0.1
2	235.2	0.3	23.9	22.5	27.9	16.4	0.1
3	582	0	44	63.5	70.5	15	0
4	144.1	0.9	0.1	0.3	0.3	0	0.1
5	279.7	0.1	0.1	0.2	0.1	0	0.1
6	601	0	2	1	1	0	0
7	134.4	5.5	0	0	0	0.2	0.1
8	250.1	17.7	0	0	0	0	0
9	528	0	0	0	0	0	0.1
10	150	0	16.6	19.4	23.4	8.6	0.1
11	234.7	0.3	24.9	28.5	34.9	13.42	0.2
12	592	0	62.5	73.5	90.0	22.1	0.1
13	148.2	1.8	0.6	0.8	1.8	0.9	0.2
14	219.8	0.1	0.9	1.21	3.4	0.77	0.1
15	579.5	0	5.5	7.5	9	4.5	0
16	126	10.4	0.4	3	0	0	0.1
17	239.4	0.1	0.4	0.1	0	0	0
18	606	0	0.1	0.1	0.1	0.1	1
19	131.4	2.6	0	0.3	0	0	0
20	602	4.2	0	0	0	8	0

B.3 Calculating Leaching Efficiency Example

The concentration of metal (C_i) (mg/L) in the leachate was obtained from the MP-AES analysis presented in Table 16. The weight of each sample, m_0, is the initial amount of black mass utilized in the water leaching experiments. The weight percentage, w_i, of the metals presented in the black mass are listed in the table below.

Electrode Composition (wt.%) from MP-AES used in calculations						
Fe	Cu	Ni	Co	Li	Mn	Al
0.25 ± 0.0	1.52 ± 0.12	9.39 ± 0.18	9.0 ± 0.24	3.63 ± 0.27	6.9 ± 0.07	0.14 ± 0.01

$$Leaching\ efficiency\ (\%) = \frac{C_i \cdot V}{m_0 \cdot w_i} \cdot 100$$

Mass of solid sample (g)	Li in black mass (wt.%)	MP-AES Experimental conc. of Li (mg/L)	Volume of leachate (L)
2.006	3.63	134.4	0.080

Initial amount of Li in 2.006 g black mass ($m_{Li,0}$):

$$m_{Li,0} = m_0\ (g) \cdot w_{Li}$$

$$m_{Li,0} = 2.006\ (g) \cdot 3.63 = 0.0728\ (g)$$

Mass of Li in solution after water leaching experiment ($m_{Li,1}$):

$$m_{Li,1} = \frac{C_{Li}\ (mg/L)}{1000\ (mg/g)} \cdot V_{leachate}\ (L)$$

$$m_{Li,1} = \frac{134.4\ (mg/L)}{1000\ (mg/g)} \cdot 0.08\ (L) = 0.0107\ (g)$$

Leaching efficiency with respect to Li:

$$L\ \% = \frac{m_{Li,1}}{m_{Li,0}} \cdot 100\ \%$$

$$L\ \% = \frac{0.0107\ (g)}{0.0728\ (g)} \cdot 100\% = 14.69\ \%$$

Meaning, 14.69 % of Li was dissolved in solution through water leaching.

B.4 Leaching Efficiency for all Metals

Table 17 depicts the calculated leaching efficiencies (%) for all metals from the described procedure above (Appendix B.3).

Table 17: Metal leaching efficiency (%) from water leaching experiments.

Exp.	Li	Al	Ni	Co	Mn	Cu
1	15.49	0.26	0.68	0.80	5.6	5.64
2	12.96	0.33	0.51	0.50	0.80	2.15
3	8.12	0	0.24	0	0.52	0.35
4	15.81	0	0	0.3	0.3	0
5	14.42	0.13	0	0	0	0
6	8.17	0	0	0	0	0
7	14.69	15.44	0	0	0	0
8	13.66	24.92	0.1	0.1	0	0
9	7.27	0	0	0	0	0
10	15.49	0	0.82	1.0	1.57	2.62
11	14.54	0.47	0.59	0.70	1.13	0.73
12	7.48	0	0.34	0.41	0.66	4.2
13	15.14	5.63	0	0	0.1	0
14	13.91	0.18	0.2	0.03	0.1	0.1
15	8.19	0	0.03	0.04	0.07	0.15
16	15.10	31.82	0	0	0.14	0
17	14.01	0.15	0	0	0	0
18	8.30	0	0	0	0	0.3
19	17.04	1.06	0	0	0	0
20	9.32	13.88	0	0	0	0.31

C Direct Lithium Extraction from Leachate

C.1 Direct Lithium Extraction Experiments and Conditions

This section serves as a summary for the performed DLE experiments throughout this work, where the experimental conditions will be summarized once more.

Table 18: Conditions employed for kinetic studies.

Kinetic study Experiments				
Initial Li$^+$ (mg/L)	Resin	s/l ratio (g/L)	Temp. (°C)	Contact time (h)
131.4	Amberlite H-form	20	25	4
131.4	Amberlite Na-form	20	25	4
131.4	Molecular sieve 13X	20	25	4
602	Amberlite H-form	20	25	4

Table 19 presents the conditions employed for the solid-liquid ratio experiments with Amberlite H-form and Amberlite Na-form washed with 1M HCl. The contact time was set to 30 minutes for all independent experiments.

Table 19: Solid-liquid ratio study from Amberlite H-form and Amberlite Na-form.

Solid-liquid ratio Experiments			
Initial Li$^+$ (mg/L)	Resin	s/l ratio (g/L)	Temp. (°C)
131.4	Amberlite H-form	20	25
131.4	Amberlite H-form	40	25
131.4	Amberlite H-form	60	25
602	Amberlite H-form	20	25
602	Amberlite H-form	40	25
602	Amberlite H-form	60	25
131.4	Amberlite Na-form	20	25
131.4	Amberlite Na-form	40	25
131.4	Amberlite Na-form	60	25

Table 20: Desorption experiments from Amberlite H-form

Desorption Experiments			
Initial Li$^+$ (mg/L)	Resin	1M HCl (L)	Temp. (°C)
131.4	Amberlite H-form	0.1	25
131.4	Amberlite H-form	0.1	25
131.4	Amberlite H-form	0.1	25
602	Amberlite H-form	0.1	25
602	Amberlite H-form	0.1	25
602	Amberlite H-form	0.1	25

Table 21 presents the conditions for the reutilization experiments with Amberlite H-form resins, displaying the variation in solid-liquid ratio for the second round of experiments as a result of resin loss during the initial experiments, explained previously in section 6.4.4.

Table 21: Reutilization experiments with Amberlite H-form resins.

Reutilization Experiments			
Initial Li$^+$ (mg/L)	Resin	s/l ratio (g/L)	Temp. (°C)
131.4	Amberlite H-form	18.63	25
131.4	Amberlite H-form	22.30	25
131.4	Amberlite H-form	35.80	25
602	Amberlite H-form	9.02	25
602	Amberlite H-form	23.02	25
602	Amberlite H-form	36.07	25

The conditions employed for the experiments with synthetic LiCl and 1:1 mix of 0.2M LiCl and 0.1M NaCl solutions are presented in Table 22. All experiments were performed for a fixed solid-liquid ratio of 20 g/L with Amberlite H-form resins at 25°C.

Table 22: Conditions employed for adsorption of synthetic solutions of LiCl and NaCl.

Synthetic Solution Experiments			
Solution	Initial Li$^+$ (mg/L)	Initial Na$^+$ (mg/L)	Resin
0.01M LiCl	69.3	0	Amberlite H-form
0.1M LiCl	665	0	Amberlite H-form
0.2M LiCl	1376	0	Amberlite H-form
0.2M LiCl+0.1M NaCl	725	1103	Amberlite H-form

C.2 Direct Lithium Extraction Calculation Example

The concentration of Li^+ in the leachate (C_i) was obtained from MP-AES (Table 16), as well as the Li^+ concentration in the depleted solution and the final concentration after desorption with HCl.

Li^+ concentration in leachate (mg/L)	Li^+ concentration in depleted solution (mg/L)	Li^+ concentration after desorption (mg/L)
131.4	24.4	106.43

Li^+ uptake capacity from the resin (Q_{Li+}) was calculated as follows:

$$Q_{Li+} = (131.4 - 24.4) \ (mg/L) \cdot \frac{0.1 \ (L)}{2.0 \ (g)} = 5.34 \ (mg/g)$$

The Li^+ retention yield (R_{Li+}) was calculated as follows:

$$R_{Li+} = \frac{(131.4 - 24.4) \ (mg/L)}{131.4 \ (mg/L)} \cdot 100\% = 81.43\%$$

The volume of HCl utilized for all desorption experiments was 100 mL and the Li^+ desorption yield ($Li^+_{desorption}$) was calculated as follows:

$$Li^+_{desorption} = \frac{106.43 \ (mg/L) \cdot 0.1 \ (L)}{5.34 \ (mg/g) \cdot 2.0 \ (g)} \cdot 100\% = 99.46\%$$

The global Li^+ recovery throughout the adsorption and desorption process was calculated as follows:

$$Li^+_{Recovery} = \frac{106.43 \ (mg/L) \cdot 0.1 \ (L)}{131.4 \ (mg/L) \cdot 0.1 \ (L)} \cdot 100\% = 80.99\%$$

C.3   Results obtained from Kinetic Study

Table 23 presents the result from the kinetic study previously discussed in section 6.4.1, where it was recognized that the uptake capacity (Q) and retention yield (R) of Li^+ was highest for Amberlite H-form.

Table 23: Results from the performed kinetic study for Amberlite H-form, Amberlite Na-form and Molecular sieve 13X.

Results from Kinetic Study			
Initial Li^+ (mg/L)	Resin	Q_{Li^+}	R_{Li^+} (%)
131.4	Amberlite H-form	5.34 ± 0.26	81.43 ± 3.94
131.4	Amberlite Na-form	1.76 ± 0.31	26.70 ± 1.25
131.4	Molecular sieve 13X	1.39 ± 0.02	21.83 ± 0.32
602	Amberlite H-form	6.11	20.42

C.4   Results obtained from Solid-Liquid ratio study

Table 24 presents the results, in terms of uptake capacity (Q) and retention yield (R) for Li^+ for increasing solid-liquid ratio. These results were previously discussed in section 6.4.2.

Table 24: Results for increasing solid-liquid ratio

Solid-liquid ratio Experiments				
Initial Li^+ (mg/L)	Resin	s/l ratio (g/L)	Q_{Li^+}	R_{Li^+} (%)
131.4	Amberlite H-form	20	5.34	81.43
131.4	Amberlite H-forn	40	3.061	89.12
131.4	Amberlite H-form	60	2.15	93.83
602	Amberlite H-form	20	6.11	20.42
602	Amberlite H-form	40	5.86	39.16
602	Amberlite H-form	60	5.78	57.92
131.4	Amberlite Na-form	20	5.072	78.32
131.4	Amberlite Na-form	40	3.12	90.76
131.4	Amberlite Na-form	60	2.15	94.14

C.5 Results from Desoprtion Study

Table 25: Results from desorption/elution experiments with 1M HCl.

Desorption Experiments				
Initial Li$^+$ (mg/L)	Resin	s/l ratio (g/L)	Li$^+_{desorption}$ (%)	Li$^+_{Recovered}$
131.4	Amberlite H-form	20	99.46	80.99
131.4	Amberlite H-form	40	98.45	90.39
131.4	Amberlite H-form	60	97.11	94.61
602	Amberlite H-form	20	61.22	12.50
602	Amberlite H-form	40	79.59	30.00
602	Amberlite H-form	60	70.50	40.83

C.6 Results from Reutilization Study

Table 26: Reutilization study of Amberlite H-form for initial Li$^+$ concentration of 131.4 mg/L.

Resin	s/l ratio (g/L)	Q$_{Li^+}$ (mg/g)	R$_{Li^+}$ (%)
Fresh Amberlite H-form	20	5.34	81.43
Fresh Amberlite H-form	40	3.10	89.12
Fresh Amberlite H-form	60	2.15	93.83
Regenerated Amberlite H-form	18.63	5.27	74.71
Regenerated Amberlite H-form	22.30	5.16	83.65
Regenerated Amberlite H-form	35.80	3.36	87.64

Table 27: Reutilization study of Amberlite H-form for initial Li$^+$ concentration of 602 mg/L.

Resin	s/l ratio (g/L)	Q$_{Li^+}$ (mg/g)	R$_{Li^+}$ (%)
Fresh Amberlite H-form	20	6.11	20.16
Fresh Amberlite H-form	40	5.86	39.16
Fresh Amberlite H-form	60	5.78	57.92
Regenerated Amberlite H-form	9.02	11.64	17.50
Regenerated Amberlite H-form	23.02	6.40	24.58
Regenerated Amberlite H-form	36.07	5.90	34.42

D   Fluoride Selective Electrode

D.1   Voltage Data for Fluoride Selective Electrode Measurements

The voltage data for constructing the calibration curve, presented in section 6.3.2, is depicted in Table 28.

Table 28: Data for constructing the FSE calibration curve.

Fluoride Electrode Calibration Curve			
Actual C	C	log C	mV
500	250	2.397	-36
250	125	2.097	-13
100	50	1.6989	12
50	25	1.3979	33.2
25	12.5	1.0969	51.2
10	5	0.6989	71.9
1	0.5	-0.3010	137.8
0.1	0.05	-1.3010	181

D.2   Fluoride amount in Black Mass

The initial weight of black mass utilized for the digestion of fluoride was 0.9998 g. The digested black mass was filtered and diluted 250 times, meaning the dilution factor is 250. The obtained fluoride concentration in black mass from FSE was 55.43 mg/L.

Amount of fluoride in black mass prior to dilution:

$$m_{F^-} = 55.43 \ mg/L \ \cdot 0.25 \ L = 13.857 \ mg = 0.0138 \ g$$

Weight % of fluoride in black mass:

$$F^- = \frac{0.0138 \ g}{0.9998 \ g} \cdot 100 = 1.39 \ wt\%$$

Meaning, that the wt% of fluoride in the black mass was 1.39 wt%.

The previously discussed fluoride concentrations dissolved in the water leached solutions (section 6.3.2) are presented in Table 29, arranged according to the studied leaching conditions, temperature (°C), pH and solid-liquid ratio (g/L).

Table 29: Fluoride concentration in water leached solutions.

Fluoride Concentration in water leached solutions				
Temperature °C	pH	s/l ratio (g/L)	mV	F$^-$ (mg/L)
25	10.0	20	-25.2	423.23
25	10.0	150	-59.1	1584.52
60	6.5	20	-18.8	330.0
60	6.5	40	-35.7	637.03
60	6.5	150	-58.1	1524.0
80	6.5	20	-22.8	385.47
80	6.5	40	-39	724.38
80	6.5	150	-59.3	1596.90
60	8.0	20	-21.6	367.87
60	8.0	40	-39.6	741.51
60	8.0	150	-61	1706.20
80	8.0	20	-25.2	423.24
80	8.0	40	-43.1	849.78
80	8.0	150	-62	1773.95
60	10.0	20	-23.5	396.20
60	10.0	40	-41.9	810.98
60	10.0	150	-63	1844.39
80	10.0	20	-28.7	483.50
80	10.0	40	-45.1	918.0
80	10.0	150	-64.2	1932.62

E   EDS data from Scanning Electron Microscopy

Figure .1 presents the EDS mapping for the 5 µm spherical black mass particle presented in section 6.1.3. From the map, the presence of 5.2 wt% Co, 5.1 wt% Ni and 3.9 wt% Mn are identified, from Figure .2 on the next page, confirming the NMC cathode material.
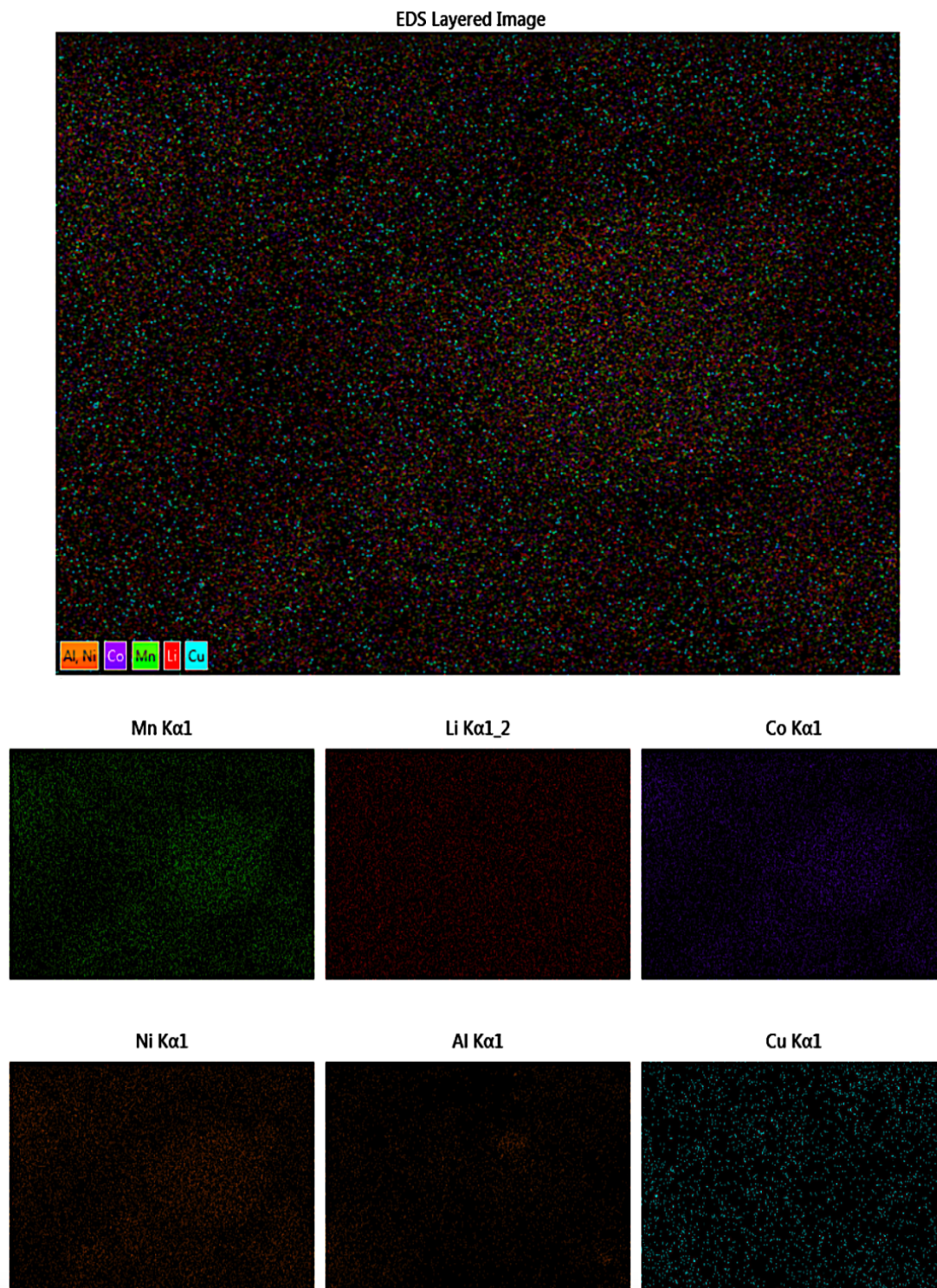
Figure .1: EDS mapping on 5 µm spherical black mass particle.
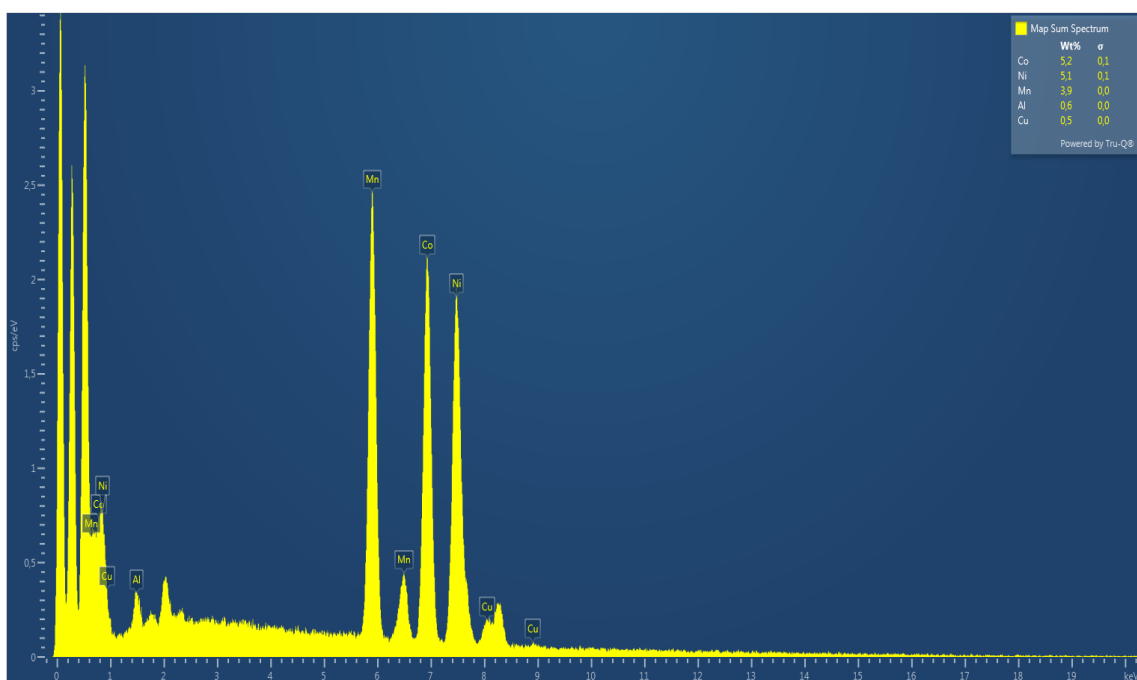
E.1 Graphs from EDS
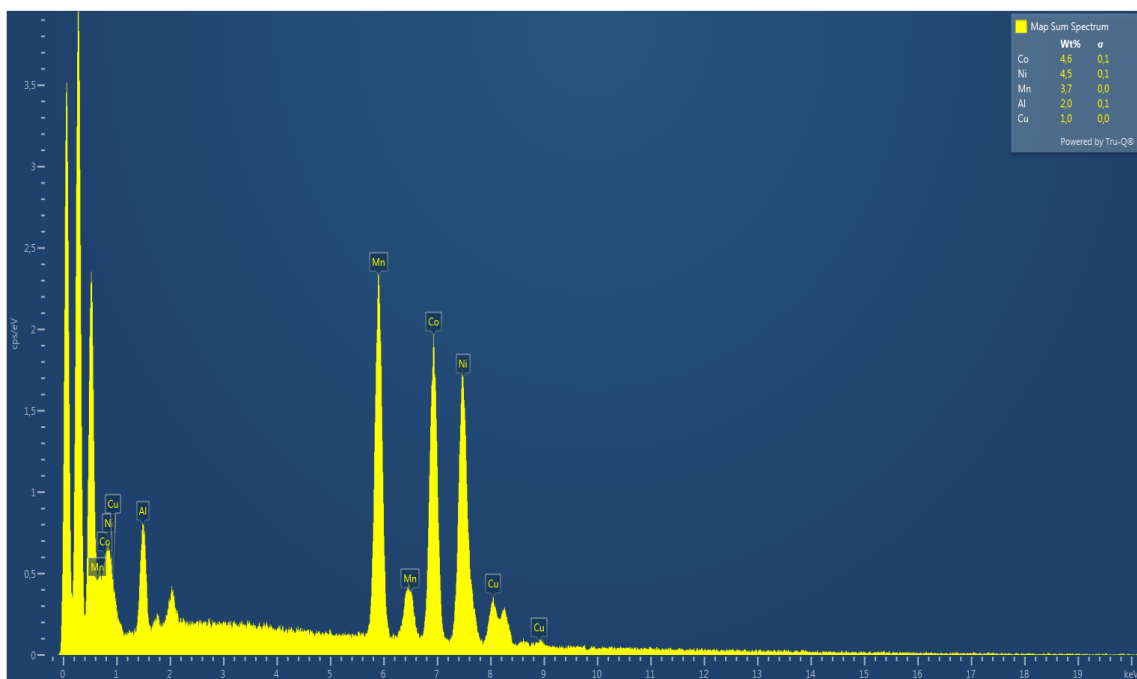

Figure .2: Black mass map sum spectrum.

Figure .3: Filter residue map sum spectrum.

F   Detailed Calibration Curves from MP-AES Software
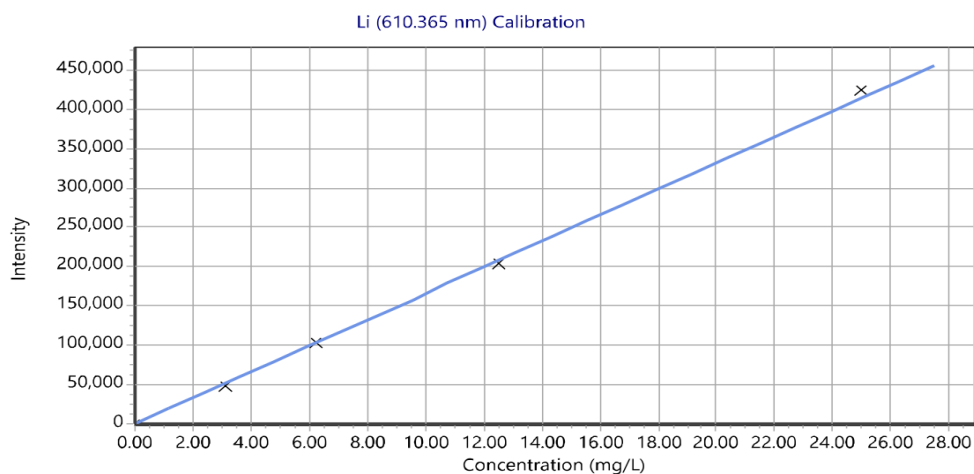
Figure .4: MP-AES calibration curve for lithium.
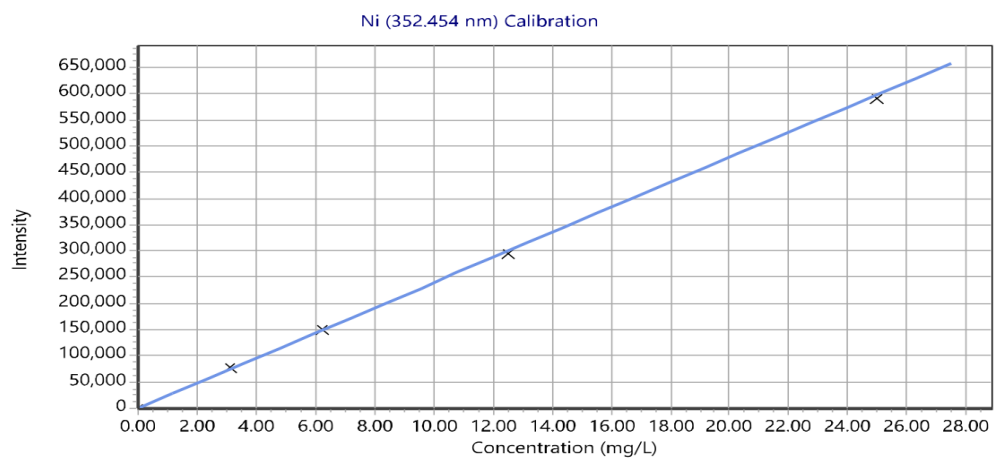
Figure .5: MP-AES calibration curve for nickel.
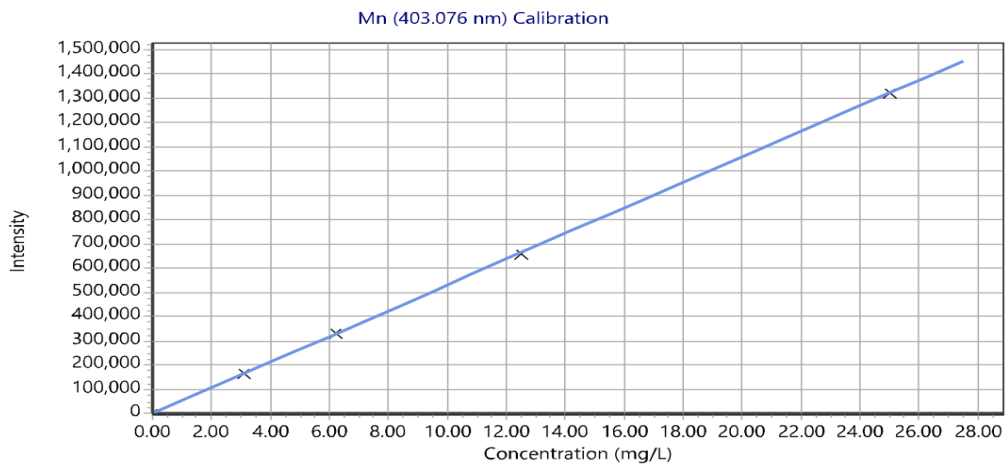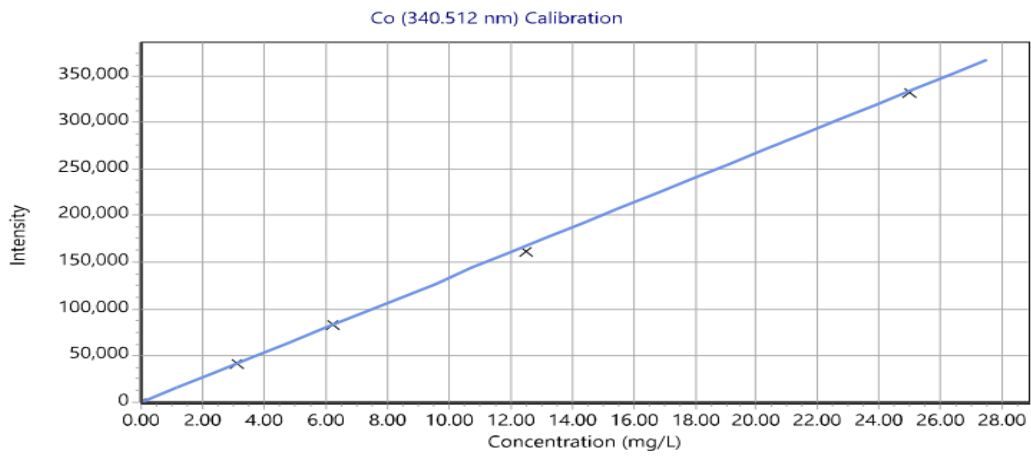
Figure .6: MP-AES calibration curve for manganese.
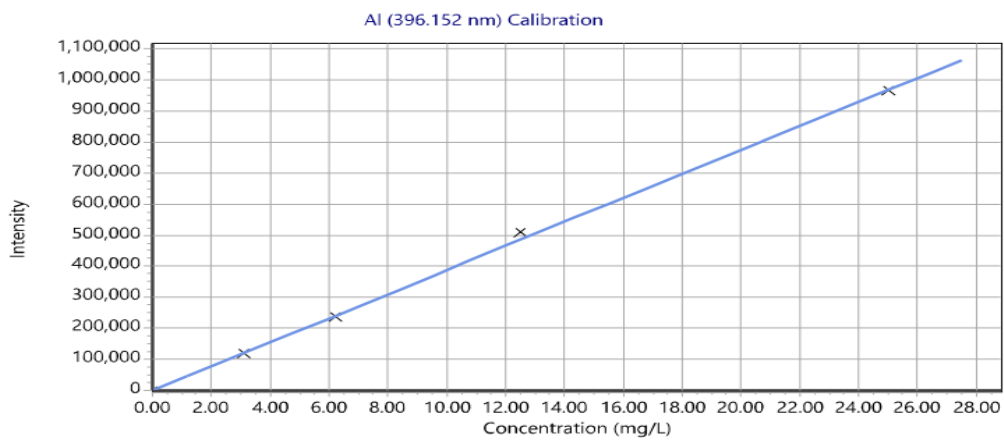

Figure .7: MP-AES calibration curve for cobalt.
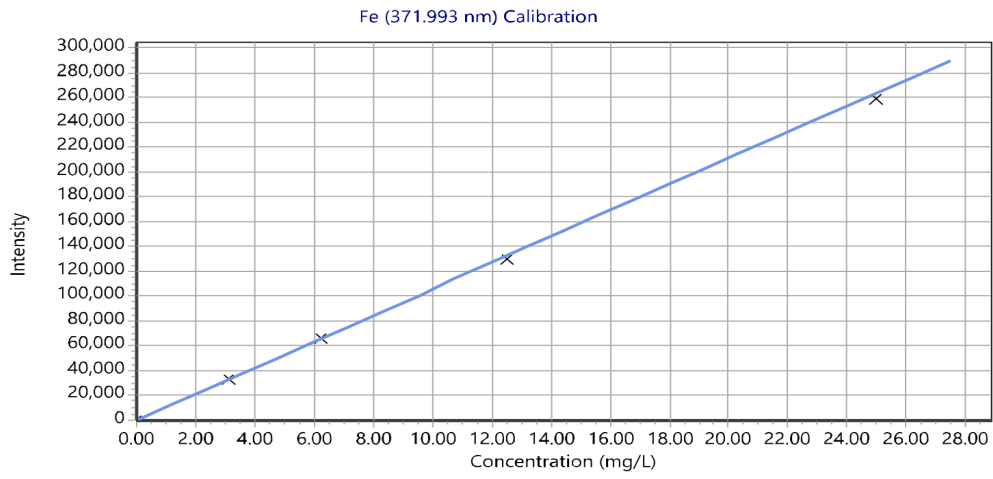

Figure .8: MP-AES calibration curve for aluminium.

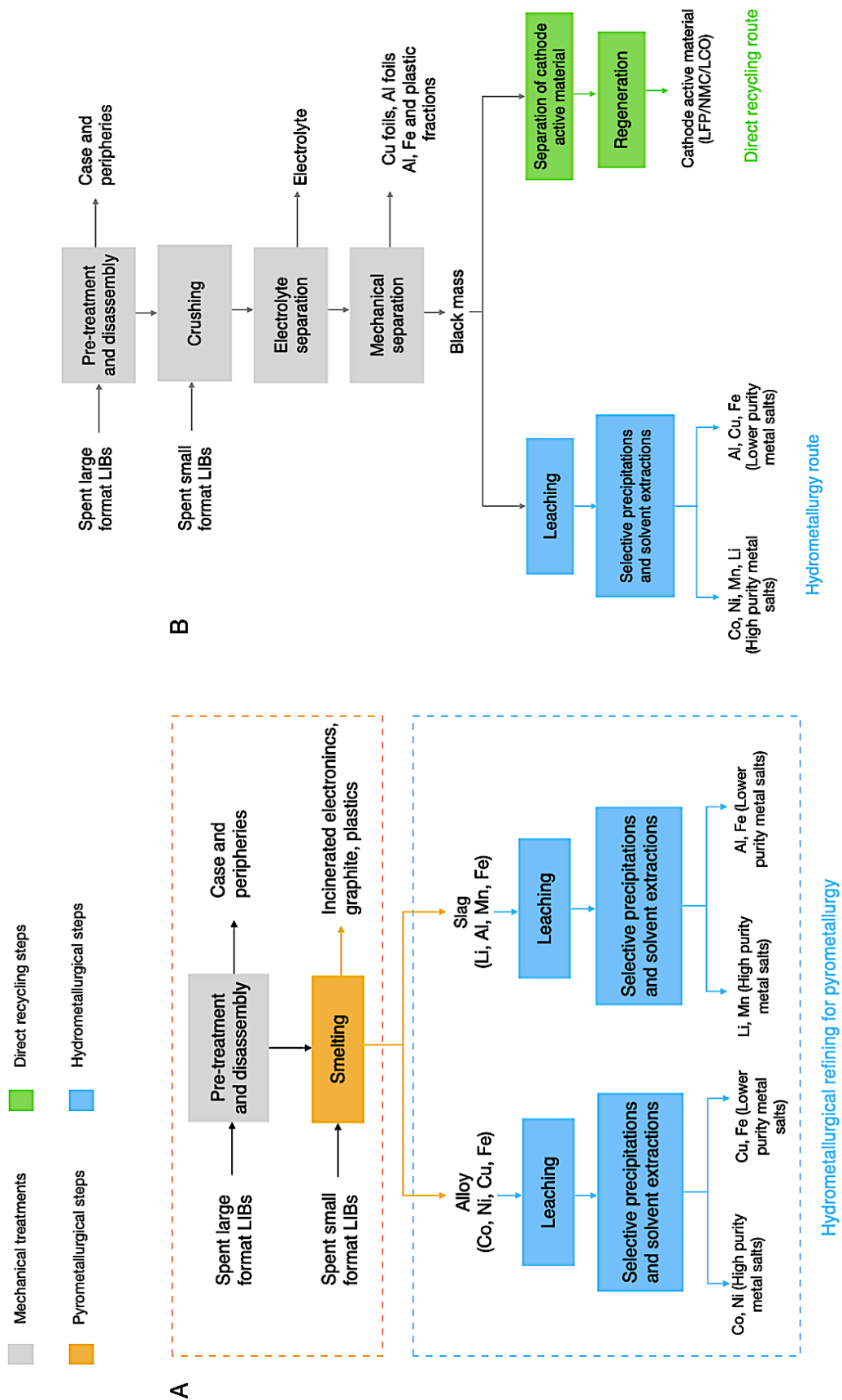Figure .9: MP-AES calibration curve for iron.

Figure .10: Block flow diagrams of general LIB recycling routes: (A) pyrometallurgical route, with hydrometallurgical refining of the alloy and the slag, (B) hydrometallurgical/co-precipitation/direct recycling routes, preceded by a mechanical separation step [5].